

## INFORMATION TO USERS

This manuscript has been reproduced from the microfilm master. UMI films the text directly from the original or copy submitted. Thus, some thesis and dissertation copies are in typewriter face, while others may be from any type of computer printer.

**The quality of this reproduction is dependent upon the quality of the copy submitted.** Broken or indistinct print, colored or poor quality illustrations and photographs, print bleedthrough, substandard margins, and improper alignment can adversely affect reproduction.

In the unlikely event that the author did not send UMI a complete manuscript and there are missing pages, these will be noted. Also, if unauthorized copyright material had to be removed, a note will indicate the deletion.

Oversize materials (e.g., maps, drawings, charts) are reproduced by sectioning the original, beginning at the upper left-hand corner and continuing from left to right in equal sections with small overlaps. Each original is also photographed in one exposure and is included in reduced form at the back of the book.

Photographs included in the original manuscript have been reproduced xerographically in this copy. Higher quality 6" x 9" black and white photographic prints are available for any photographs or illustrations appearing in this copy for an additional charge. Contact UMI directly to order.

U·M·I

University Microfilms International  
A Bell & Howell Information Company  
300 North Zeeb Road, Ann Arbor, MI 48106-1346 USA  
313/761-4700 800/521-0600



**Order Number 9325038**

**On the annual cycle of the tropical Pacific atmosphere and  
ocean**

**Li, Tianming, Ph.D.**

**University of Hawaii, 1993**

**U·M·I**  
300 N. Zeeb Rd.  
Ann Arbor, MI 48106



ON THE ANNUAL CYCLE OF THE TROPICAL PACIFIC ATMOSPHERE AND OCEAN

A DISSERTATION SUBMITTED TO THE GRADUATE DIVISION OF THE  
UNIVERSITY OF HAWAII IN PARTIAL FULFILLMENT OF THE  
REQUIREMENTS FOR THE DEGREE OF

DOCTOR OF PHILOSOPHY

IN

METEOROLOGY

MAY 1993

BY

Tianming Li

Dissertation Committee

Bin Wang, Chairperson  
Roger Lukas  
Dennis Moore  
Thomas Schroeder  
Duane Stevens

## ACKNOWLEDGEMENTS

I would like to take this opportunity to recognize my deep appreciation for the support and encouragement provided to me by my advisor Professor Bin Wang. His guidance in scientific research and interesting discussions as well as the initiation of the two-and-half-layer atmospheric model are crucial for my dissertation studies. I would like to thank my dissertation committee for their valuable comments and suggestions, and particularly thank Professor R. Lukas for his stimulation in the study of the western Pacific remote wind forcing. Thanks goes to Professor Ping Chang of Texas A & M University for his providing an oceanic mixed-layer model. A special thanks goes to my wife, Lili, for her continuous support and encouragement.

## ABSTRACT

A simple climate model is proposed for studying the key parameters of the coupled ocean-atmosphere system, monthly mean surface winds and precipitation. In this model, sea-level pressure is thermodynamically determined from sea surface temperature (SST) through a vertically integrated hydrostatic equation in which the vertical mean lapse rate is a function of SST plus a time-independent correction. The surface wind are then computed from the sea-level pressure gradients through a linear surface momentum balance with the anisotropic and latitude-dependent Rayleigh friction coefficients. The precipitation is calculated from a moisture budget by taking into account the effect of SST on convective instability. This model is capable of simulating a realistic annual cycle of the surface winds, sea-level pressure, and precipitation over the tropical Pacific. The response of the tropical atmosphere to symmetric and antisymmetric SST forcing is examined using the simple model. It is found that the annual variation of the symmetric SST mode results in the westward propagation of the surface zonal wind, sea-level pressure, and precipitation along the equator and the antisymmetric SST variation causes the seasonal oscillation of monsoonal circulations and rainfall.

The mechanisms of annual variations of the tropical Pacific sea surface temperature are investigated using a reduced-gravity ocean model. It is found that the westward propagation of the equatorial SST anomaly is due to wind-related dynamic processes. Therefore, the westward propagation of atmospheric and oceanic quantities is a manifestation of coupled air-sea interaction. The initiation of anomalous warming or cooling in the eastern Pacific, however, is primarily due to the northward propagation of the SST anomaly in response to solar radiation forcing. As a result, the annual variation of the Pacific SST can be regarded as an interplay between coupled air-sea interaction and solar radiation forcing. The remote forcing of anomalous winds in the western Pacific also shows contribution on the SST variation in the eastern Pacific. The annual variation of cloudiness has effects on the change of SST in the western Pacific and the northeastern Pacific monsoon region.

## TABLE OF CONTENTS

|  |      |
|--|------|
| ACKNOWLEDGEMENTS.....  | iii  |
| ABSTRACT.....  | iv   |
| LIST OF FIGURES.....   | viii |
| LIST OF ABBREVIATIONS.....   | xiv  |
| LIST OF SYMBOLS.....   | xiv  |
| <br>   |      |
| CHAPTER 1 INTRODUCTION.....  | 1    |
| CHAPTER 2 A SIMPLE TROPICAL ATMOSPHERE MODEL<br>OF CLIMATOLOGY AND VARIABILITY OF<br>SURFACE WINDS AND PRECIPITATION.....          | 5    |
| 2.1 Introduction.....  | 5    |
| 2.2 Diagnosis of problems in simple<br>atmospheric models.....   | 9    |
| 2.3 The model.....   | 21   |
| 2.4 Simulation of the annual cycle of the<br>tropical Pacific atmosphere.....  | 25   |
| 2.5 The response of tropical atmosphere<br>to symmetric and antisymmetric SST<br>forcing.....                                      | 28   |
| CHAPTER 3 ON THE ANNUAL CYCLES OF THE TROPICAL<br>PACIFIC SEA SURFACE TEMPERATURE.....   | 32   |
| 3.1 Introduction.....  | 32   |
| 3.2 The model description.....   | 36   |
| 3.3 The response of the tropical Pacific SST<br>to surface wind and thermal forcing:<br>surface wind stress verse heat fluxes..... | 42   |
| 3.4 The remote and local wind forcing on the<br>equatorial eastern Pacific SST.....  | 50   |
| 3.5 The effects of annual variations of<br>cloudiness on the SST change.....   | 55   |

|                        |     |
|------------------------|-----|
| CHAPTER 4 SUMMARY..... | 61  |
| APPENDIX.....          | 68  |
| REFERENCES.....        | 113 |

## LIST OF FIGURES

| <u>Figure</u> | <u>Page</u>  |
|---------------|--|
| 1a.           | Observed climatological monthly mean sea-level pressure (mb) fields (after Sadler et al. 1987) in January, April, July, and October, respectively. Contour interval is 1 mb..... 68  |
| 1b.           | Observed climatological monthly mean sea surface temperature fields (after Sadler et al. 1987) in January, April, July, and October, respectively. Contour interval is 1°C..... 69   |
| 2.            | The pressure gradient force (a), Coriolis force (b), inertial force (c), and residual force (d) computed from climatological annual mean sea-level pressure and surface winds derived from COADS by Sadler et al. (1987). The unit vector is $5 \times 10^{-4} \text{ ms}^{-2}$ ..... 70 |
| 3.            | Geographic distribution of the regions (represented by shaded areas) where opposite signs exist between the zonal residual force ( $R_1$ ) and zonal wind component (a) and between the meridional residual force ( $R_2$ ) and meridional wind component (b)..... 71                    |
| 4.            | Diagnosed annual mean zonal (a) and meridional (b) friction coefficients (in units $10^{-5} \text{ s}^{-1}$ ) based on observation. Contour interval is $0.5 \times 10^{-5} \text{ s}^{-1}$ ..... 72   |
| 5.            | The meridional distribution of zonal-averaged zonal (a) and meridional (b) friction coefficients from January (line A) through December (line L), and 12-month-mean zonal (c) and meridional (d) coefficients (in units $10^{-5} \text{ s}^{-1}$ )..... 73                               |
| 6.            | The difference between simulated and observed annual mean surface zonal (a) and meridional (b) winds (in units m/s). The simulation uses a linear three-force balance model (2.2.2) with the direction-  |

|     |  |    |
|-----|--|----|
|     | and latitude-dependent Rayleigh friction coefficients. Contour interval is 1 m/s.....  | 74 |
| 7.  | As in Fig. 6 except with a constant Rayleigh friction coefficient of $10^{-5} \text{ s}^{-1}$ . Contour interval is 1 m/s.....   | 75 |
| 8.  | (a) The diagnosed annual mean lower-troposphere geopotential height perturbation (in units m) based on the thermodynamic equation (2.2.3) in the WL model, using climatological annual mean SST and surface and 850mb winds. (b) The annual mean 850mb geopotential height perturbation (in units m) computed from climatological annual mean sea-level pressure with an approximate temperature profile proposed by Lindzen and Nigam (1987). Contour interval is 10 m..... | 76 |
| 9.  | The annual mean perturbation lapse rate (in units $10^{-5} \text{ }^{\circ}\text{C}/\text{Pa}$ ) diagnosed from the thermodynamic equation (2.2.3) using climatological annual mean SST, 850mb and surface winds, and 850mb geopotential height. Contour interval is $2 \times 10^{-5} \text{ }^{\circ}\text{C}/\text{Pa}$ .....   | 77 |
| 10. | The diagnosed January, April, July and October perturbation lapse rates (in units $10^{-5} \text{ }^{\circ}\text{C}/\text{Pa}$ ) calculated from the corresponding climatological monthly mean SST, surface and 850mb winds, and 850mb geopotential height. Contour interval is $2 \times 10^{-5} \text{ }^{\circ}\text{C}/\text{Pa}$ .....  | 78 |
| 11. | The diagnosed January, April, July and October lapse rate (in units $^{\circ}\text{C}/\text{km}$ ) distribution calculated from equation (2.3.2) by using observed climatological monthly mean SST and SLP (COADS) data. Contour interval is $0.1 \text{ }^{\circ}\text{C}/\text{km}$ .....  | 79 |
| 12. | The 12-month-mean difference between the empirical lapse rate calculated from Equation (2.3.3) and the diagnosed lapse rate calculated from Equation (2.3.2). The contour interval is $0.01 \text{ }^{\circ}\text{C}/\text{km}$ .....  | 80 |

|      |  |    |
|------|--|----|
| 13.  | The simulated (a) January, (b) April, (c) July, and (c) October sea-level pressure (in units mb) fields using the present model. Contour interval is 1 mb.....   | 81 |
| 14a. | The simulated (a) January, (b) April, (c) July, and (c) October surface wind (in units m/s) fields using the present model.....  | 82 |
| 14b. | The observed (a) January, (b) April, (c) July, and (c) October surface wind (in units m/s) fields (after Sadler et al. 1987).....  | 83 |
| 15a. | The simulated precipitation rate (in units mm/day) fields for (a) January, (b) April, (c) July, and (d) October using the present model. Contour interval is 2 mm/day.....   | 84 |
| 15b. | The observed Highly Reflective Cloud (day/month) fields for (a) January, (b) April, (c) July, and (d) October (after Garcia 1985). Contour interval is 1 day/month.....  | 85 |
| 16.  | The observed symmetric (to the equator) SST (in units of °C) modes in January, March, May, July, September, and November, respectively. Annual mean SST field has been removed. Contour interval is 0.4°C.....                                       | 86 |
| 17.  | The time-longitude section of precipitation rate (mm/day), sea-level pressure (mb) and zonal and meridional winds (m/s) along the equator in response to the symmetric SST forcing. Contour intervals are 3 mm/day, 0.4 mb, 1 m/s, and 0.4 m/s.....  | 88 |
| 18.  | The annual cycle of the zonal-averaged antisymmetric (to the equator) monsoonal mode of the monthly mean anomaly fields. The contour intervals for SST, SLP, and OLR are 0.2°C, 0.2 mb, and 3 Wm <sup>2</sup> , respectively (after Wang 1992b)..... | 89 |
| 19.  | The time-latitude section of zonal-mean precipitation rate (mm/day), sea-level   |    |

|     |   |    |
|-----|---|----|
|     | pressure (mb) and zonal and meridional winds (m/s) in response to the antisymmetric SST forcing. Contour intervals are 1 mm/day, 0.4 mb, 0.5 m/s, and 0.5 m/s, respectively.....  | 90 |
| 20. | (a) The time-longitude section of SST anomaly along the equator and (b) the time-latitude section of SST anomaly along 100-110°W. The SST is derived from COADS by Sadler et al. (1987). Contour intervals are 0.2°C and 0.4°C respectively.....  | 91 |
| 21. | Observed climatological annual mean cloudiness derived from Esbensen and Kushnir (1981) and annual mean HRC derived from Garcia (1985). Contour intervals are 0.05 and 1 day/month.....   | 92 |
| 22. | Observed climatological January and July cloudiness anomaly fields derived from Esbensen and Kushnir (1981). Contour interval is 0.05.....  | 93 |
| 23. | The simulated annual mean SST, its error and thermocline depth (m) over the tropical Pacific in response to observed annual mean wind and thermal forcing. The surface winds are derived from COADS by Sadler et al. (1987) and the heat flux data are from Esbensen and Kushnir (1981). Contour intervals are 1°C, 1°C, and 5 m, respectively..... | 94 |
| 24. | The zonal temperature advection (a), meridional temperature advection (b), vertical temperature advection (c), and thermal forcing term (d) (in units of $10^{-8}$ °C/s) in the thermodynamic equation (3.2.5) for the first ocean experiment. Contour interval is $5 \times 10^{-8}$ °C/s.....   | 95 |
| 25. | The time-longitude section of the simulated SST anomaly and the observed thermal forcing anomaly along the equator for the second ocean experiment. Contour intervals are 0.1°C and $2 \times 10^{-8}$ °C/s respectively.....   | 97 |

|     |  |     |
|-----|--|-----|
| 26. | The time-latitude section of the simulated SST anomaly and the observed thermal forcing anomaly along 100-110°W for the second ocean experiment. Contour intervals are 0.1°C and $2 \times 10^{-8}$ °C/s respectively.....   | 98  |
| 27  | The time-latitude section of downward solar flux at ocean surface derived from Esbensen and Kushnir (1981) along 90°W, 100°W, and 110°W, respectively. The effect of cloudiness has been considered. Contour interval is $10 \text{ Wm}^2$ .....   | 99  |
| 28. | The time-longitude section of the simulated SST anomaly and the observed surface zonal and meridional wind anomalies along the equator for the third ocean experiment. Contour intervals are 0.1°C, 0.5m/s, and 0.5m/s.....  | 100 |
| 29. | The time-longitude section of the simulated zonal and vertical temperature advection anomalies along the equator in the third ocean experiment. Contour interval is $2 \times 10^{-8}$ °C/s.....   | 101 |
| 30. | The time-latitude section of the simulated SST anomaly and the observed surface zonal and meridional wind anomalies along 100-110°W in the third ocean experiment. Contour intervals are 0.1°C, 0.5m/s, and 0.5m/s.....  | 102 |
| 31. | The time-longitude profile of the simulated SST anomaly along the equator (a) and the time-latitude profile of the simulated SST anomaly along 100-110°W (b) in the fourth ocean experiment in which both annual cycle winds and heat fluxes are specified. Contour interval is 0.1°C..... | 103 |
| 32. | Climatological monthly mean surface zonal wind (a) and the corresponding monthly mean anomaly (b) along the equator. Contour interval is 0.5 m/s.....  | 104 |
| 33. | Time-longitude section of simulated SST (°C) anomaly along the equator in response to anomalous surface wind forcing west of the date line. Contour interval is 0.05°C.....  | 105 |
| 34. | As in Figure 33 except for the simulated   |     |

|     |  |     |
|-----|--|-----|
|     | thermocline depth anomaly field (in units of meter). Contour interval is 0.5 m.....  | 106 |
| 35. | Horizontal structure of the thermocline depth (m) anomaly in January, April, July, and October, respectively in response to anomalous surface wind forcing west of the date line. Contour interval is 1 m..... | 107 |
| 36. | Time-longitude section of the simulated SST anomaly along the equator in response to anomalous surface wind forcing east of the date line. Contour interval is 0.1°C.....                                      | 108 |
| 37. | Time-longitude section of simulated SST (°C) and thermocline depth (m) anomalies along the equator in response to anomalous surface wind forcing east of 120°W. Contour intervals are 0.1°C and 1 m.....       | 109 |
| 38. | Simulated annual mean SST (a) and its error (b) calculating with the heat flux formulas of Equations (3.5.2-3.5.5). Contour interval is 1°C.....   | 110 |
| 39. | Simulated March and September SST fields for given climatological monthly mean wind and cloudiness fields with the heat flux formulas of Equations (3.5.2-3.5.5). Contour interval is 1°C.....                 | 111 |
| 40. | The simulated SST difference in March and September between the experiments with fixed annual mean cloudiness and with varying monthly mean cloudiness. Contour interval is 0.1°C.....                         | 112 |

## LIST OF ABBREVIATIONS

|       |  |
|-------|--|
| CISK  | Conditional Instability of the Second Kind   |
| COADS | Comprehensive Ocean-Atmosphere Data Set      |
| COARE | Coupled Ocean-Atmosphere Response Experiment |
| HRC   | Highly Reflective Cloud                      |
| OLR   | Outgoing Longwave Radiation                  |
| SLP   | Sea Level Pressure                           |
| SST   | Sea Surface Temperature                      |
| TOGA  | Tropical Ocean and Global Atmosphere         |

## LIST OF SYMBOLS

|              |   |
|--------------|---|
| $\mathbf{V}$ | Horizontal wind vector                              |
| $u, v, w$    | Zonal, meridional, and vertical velocities          |
| $x, y, z$    | Zonal, meridional, and vertical spatial coordinates |
| $t$          | Time  |
| $E_1, E_2$   | Zonal, meridional Rayleigh friction coefficients    |
| $\beta$      | Gradient of earth planetary vorticity               |
| $N$          | Newtonian cooling coefficient                       |
| $\phi$       | Geopotential height                                 |
| $\phi_{eq}$  | Equilibrium geopotential height                     |
| $I$          | Convective heating coefficient in free atmosphere   |
| $B$          | Convective heating coefficient in boundary layer    |
| $d$          | Nondimensional boundary-layer depth                 |

|            |   |
|------------|---|
| $u_B, v_B$ | Zonal and meridional wind components in boundary layer  |
| F          | Evaporational heating coefficient                       |
| $q_s$      | Sea specific humidity                                   |
| $q_a$      | Air specific humidity                                   |
| $\delta$   | Switch-on nonlinear heating coefficient                 |
| $T_{eq}'$  | Equilibrium temperature perturbation in mid troposphere |
| $T_s'$     | Sea surface temperature perturbation                    |
| $\gamma'$  | Perturbation lapse rate                                 |
| p          | Pressure  |
| g          | gravitation constant                                    |
| R          | Gas constant for dry air                                |
| $P_s$      | Sea-level pressure                                      |
| $P_u$      | Pressure at tropopause                                  |
| $Z_u$      | Height at tropopause                                    |
| $T_s$      | Sea surface temperature                                 |
| $\gamma$   | Lapse rate  |
| $P_r$      | Precipitation rate                                      |
| $\lambda$  | Precipitation efficiency coefficient                    |
| $\rho_s$   | Air density at surface                                  |
| $C_D$      | Drag coefficient  |
| $\Delta z$ | Depth of boundary layer                                 |
| f          | Coriolis parameter                                      |
| b          | Buoyancy  |
| h          | Depth of thermocline                                    |
| $\tau$     | Surface wind stress vector                              |

|                          |   |
|--------------------------|---|
| $r$                      | Rayleigh friction coefficient                               |
| $H$                      | Mean constant thermocline depth                             |
| $u$                      | Mean ocean current vector                                   |
| $r_s$                    | Rayleigh friction coefficient at shear equation             |
| $u_s, v_s$               | Zonal and meridional shear current velocities               |
| $\tau^{(x)}, \tau^{(y)}$ | Zonal and meridional wind stress components                 |
| $\rho_o$                 | Density of upper ocean                                      |
| $H_1$                    | Constant depth of ocean mixed layer                         |
| $w_e$                    | Vertical velocity at the base of the mixed layer            |
| $u_1, v_1$               | Zonal and meridional surface current velocities             |
| $T$                      | Mean surface temperature at the mixed layer                 |
| $T_e$                    | Entrained temperature                                       |
| $Q$                      | Diabatic heating  |
| $C_w$                    | Specific heat of water                                      |
| $\kappa$                 | Diffusion coefficient                                       |
| $J$                      | Penetration rate of solar radiation                         |
| $R$                      | Penetration coefficient                                     |
| $r_1, r_2$               | Penetration e-folding depths                                |
| $\alpha$                 | Coefficient of entrained temperature                        |
| $T_{sub}$                | Temperature at the base of mixed layer                      |
| $T_{am}$                 | Observed annual mean temperature at the base of mixed layer |
| $h_m$                    | Simulated annual mean thermocline depth                     |
| $T_m$                    | Simulated annual mean surface temperature                   |
| $T_r$                    | Temperature below the thermocline                           |
| $Q_0$                    | Monthly averaged direct and diffuse maximum solar flux      |

|                 |   |
|-----------------|---|
| A               | Surface albedo                                      |
| n               | Monthly mean cloudiness                             |
| $\varepsilon$   | Emissivity of water                                 |
| $\sigma$        | Stefan-Boltzmann constant                           |
| e               | Water vapor pressure                                |
| $T_a$           | Air surface temperature                             |
| L               | Latent heat for evaporation                         |
| $C_p$           | Specific heat at constant pressure                  |
| $V_a$           | Surface wind speed                                  |
| $a_1, a_2, a_3$ | Coefficients of solar and longwave radiation fluxes |

## CHAPTER ONE

### INTRODUCTION

In the last decade, coupled ocean-atmosphere models of varying complexity have been developed to study the interannual variability of El Nino/ Southern Oscillation (ENSO) with either specified or oversimplified annual cycles in both ocean and atmosphere (e.g., Anderson and McCreary 1985, Zebiak and Cane 1987, Schopf and Suarez 1988). These numerical studies revealed the importance of annual cycles on the phase locking of the ENSO-like oscillations. Since the annual cycle is one of most dominant variations in the tropical atmosphere and ocean, a natural question is what physical processes are responsible for the annual variability of the tropical Pacific atmosphere and ocean.

Webster and Lukas (1992) in their summary paper about TOGA COARE state that:

"Although theories of low-frequency variability of the coupled ocean-atmosphere system depend crucially on the form of the basic state of the warm-pool region of the tropical Pacific Ocean, the processes that determine and maintain the basic state are not understood.

... The two basic theories of the El Nino-Southern Oscillation phenomenon (i.e., either coupled ocean-atmosphere instability or cyclic equilibrium of a closed tropical ocean basin involving successive boundary reflections and

interactions of equatorially trapped modes) depend on the existence of a basic state with very specific properties. The mechanisms that maintain the basic state are not well understood."

Observations have indicated that there is a prominent annual oscillation of monsoonal circulations and rainfall in the tropical Pacific atmosphere. The oscillation is consistent with an antisymmetric SST variation (Wang 1992b). Climatological convergence zones also shows clear annual variations. For instance, the intertropical convergence zone (ITCZ) has maximum strength along 5°N in January and shifts to 10°N in July. The South Pacific convergence zone (SPCZ) extends to 15°S in the northern winter and retreats northwestward during the northern spring and summer. The meridional shift of the atmospheric convergence zones coincides with the annual cycle of SST (see Sadler et al. 1987).

A remarkable feature in the Pacific ocean is the annual march and retreat of the equatorial Pacific SST cold tongue. The first harmonic analysis of annual variation of SST along the equator shows a systematic longitude change in both phase and amplitude with a prominent westward propagation in the eastern-central Pacific (Horel, 1982). Such propagation is thought to be a manifestation of the interaction between the Walker circulation and SST (Bjerknes 1966, Horel 1982) and can be regarded as a result of the interplay between a forced

monsoonal mode, a direct response of the Pacific ocean to external solar radiation forcing, and a coupled equatorial mode which reflects an interaction between atmosphere and ocean (Wang 1992b). In the subthermocline region between 300 and 800 m, observed annual variations in thermal structure of the central equatorial Pacific is found to be a forced lowest-mode Rossby wave in response to westward propagating annual surface wind forcing (Lukas and Firing, 1985).

The objective of the present study is to investigate the physical mechanisms of annual cycles of the tropical Pacific atmosphere and ocean using simple atmosphere and ocean models. I try to understand what physical processes cause the annual oscillations of the monsoonal circulations and rainfall and what processes are responsible for annual variations of the equatorial cold tongue.

So far a number of simple atmosphere and ocean models have been developed to study the atmospheric response to SST and the oceanic response to surface wind forcing. Worth particularly mentioning among them are a two and one-half layer atmospheric model that consists of both Gill's (1980) and Lindzen-Nigam's (1987) mechanisms (Wang and Li 1993) and a reduced-gravity ocean model which simulates the tropical Pacific SST climatology (Seager et al. 1988). Both the atmospheric and oceanic models are capable of simulating some important features of annual cycles in the tropical Pacific. However, some problems still remain.

This dissertation study contains two major parts. In Chapter 2, the dynamic and thermodynamic problems of a simple atmosphere model are diagnosed using climatological monthly mean COADS data. Based on the observations, a simple tropical atmosphere model is proposed to simulate the annual cycles of surface wind, sea-level pressure, and precipitation over the tropical Pacific. This model is also used to investigate the physical mechanisms of atmospheric response to symmetric and antisymmetric SST forcing. In Chapter 3, a modified reduced-gravity upper ocean model is described. This model is used to investigate the physical mechanisms of the annual variations of SST in the tropical Pacific. Two processes in terms of the wind-induced dynamic process and heat flux forcing are investigated. The effects of remote and local anomalous winds on the equatorial eastern Pacific SST and the influence of annual variations of cloudiness on the SST change are also examined.

CHAPTER TWO  
A SIMPLE TROPICAL ATMOSPHERE MODEL  
OF CLIMATOLOGY AND VARIABILITY OF  
SURFACE WINDS AND PRECIPITATION

2.1 Introduction

A large number of simple or intermediate models in the past decade have been developed to study climatology and variability in the tropical atmosphere and ocean. The fundamental physics involved in these models are large-scale air-sea interactions. For the meteorological component, a key element is to predict as accurately as possible surface winds and precipitation/cloudiness for a given SST forcing.

Gill's single-vertical mode model has been a basic dynamic framework for most of simple or intermediate atmosphere models. Following linear wave solutions of the tropical atmospheric motion (Matsuno 1966), Gill (1980) presented a simple first-baroclinic-mode model in which the wind and pressure fields in the upper troposphere have opposite signs with those in the lower troposphere and maximum vertical motion and atmospheric heating appear in the middle troposphere. This model was originally built for studying the response of tropical Walker and Hadley circulations to imposed atmospheric heating (Gill 1982). Later it was used to study interannual variability (e.g., Zebiak 1982, Zebiak and Cane, 1987) and the annual cycle (Seager 1991, Wang and Li 1993) as

well as intraseasonal oscillation (Wang 1988). This model is referred to as the Gill-type model (or simply the Gill model, hereafter).

The improvement of the thermodynamics of the Gill model has been attempted through different physical considerations. Zebiak (1982) assumed evaporational heating proportional to SST and its anomaly, and later (1986) included circulation-dependent moisture convergence feedback. Davey and Gill (1987) introduced a Newtonian cooling process as thermal forcing through which the atmosphere tends toward an equilibrium state controlled by SST. Seager (1991) considered the importance of buoyancy in representation of convective heating through convective instability, following the argument that the tropical atmosphere is not always conditionally unstable (Betts 1982, Emanuel 1986). Wang and Li (1993) (WL hereafter) proposed a nonlinear SST-dependent atmospheric heating scheme in which the atmospheric heating essentially incorporates all three thermodynamic processes described in the aforementioned models.

The essential premise of the Gill model is that tropical low-level flow is driven by diabatic heating. On the other hand, Lindzen and Nigam (1987) proposed a different mechanism in which boundary-layer flows are driven directly by SST gradients through momentum forcing. Both the Gill-type and Lindzen-Nigam models have a similar mathematical formulation and one can be derived from the another (Neelin 1989). In all

simple models, unrealistically large values of Rayleigh friction and Newtonian cooling are required to produce reasonable magnitudes of the tropical wind and convergence.

When other physical processes are added to the WL model, the simulated surface or low-level winds do not show significant improvement. The motivation of the present study comes from a natural question, namely "What is the key quantity for a simple model to simulate realistic surface (or low-level) winds?". According to the surface momentum balance equation, surface winds are only driven by the surface pressure gradient. Therefore, the key element for simulating a realistic wind field is to predict an accurate enough sea-level pressure field.

Observations show a high correlation between climatological monthly mean SST and sea-level pressure (SLP). Inspection of the tropical marine climatic atlas by Sadler et al. (1987) discloses an obvious linkage between SLP and SST (Figure 1a and 1b). In the western Pacific the highest SST is located at 10°S in January and moves to 15°N in July. The surface pressure shows a similar shift with minimum pressure at 10°S (northwest of Australia) in January and 10-20°N (northwestern Pacific) in July. The SST cold tongues in the eastern North and South Pacific are located east of the subtropical high systems in the Northern and Southern Hemispheres, respectively. The trade wind trough is strongest in July along 10°N and weakest in January along 5°N, closely

following the annual shift of the warm water zone as indicated by the 27.5°C SST contour along 8–10°N in July and a contour line of 26.5°C along 5–8°N in January. The similarity between climatological monthly mean SLP and SST reminds us: Can we establish a direct relationship between the two quantities?

Another issue is to what extent linear dynamics in the Gill model is reasonable for the surface momentum balance. In other words, can we use the linear three-force balance model to simulate a realistic surface wind field by giving an observed sea-level pressure field? Linear dynamics of the Gill model provides the three-force balance among pressure gradient force, Coriolis force and Rayleigh friction. What is the function of nonlinear advection terms? Is nonlinearity of transient-eddy effects important for the time-mean surface momentum balance? How do we adequately parameterize these transient effects if they are important? All these questions are related to the linear dynamics of the Gill model and must be addressed.

The purpose of the present study is to analyze detailed dynamic and thermodynamic balances using observed climatological monthly mean data and to develop a simple atmosphere model to simulate key parameters for the coupled ocean-atmosphere system. The model can be used to study tropical atmosphere variabilities ranging from time scale of months to years. In Section 2.2, the dynamic and thermodynamic problems of a simple atmospheric model are diagnosed by using

observed climatological monthly mean data. Based on the aforementioned observation, a simple tropical atmosphere model is proposed and described in Section 2.3. The ability of the model to simulate the annual cycle in the tropical Pacific atmosphere is shown in Section 2.4 for given sea surface temperature forcing. In Section 2.5, the response of the tropical Pacific atmosphere to symmetric and antisymmetric SST forcing is investigated.

## 2.2 Diagnosis of problems in simple atmospheric models

In this section, the dynamic and thermodynamic problems of simple atmospheric models are analyzed using climatological monthly mean SST, SLP, and surface wind fields derived from Comprehensive Ocean-Atmosphere Data Set (COADS) (1900-1979) by Sadler et al. (1987). The data were on  $2^\circ \times 2^\circ$  grid. Climatological monthly mean 850 mb winds are derived from 7-year-mean ECMWF analyzed data (1979-1985) with the resolution of  $5^\circ \times 5^\circ$ .

### 2.2.1 Dynamics problems

The horizontal low-level (or surface layer) momentum budget in the Gill-type model requires a balance among pressure gradient force, Coriolis force and Rayleigh friction. The three-force balance forms the basis of the linear dynamics in the Gill model. The nonlinearity is shown to be unimportant based on a diagnosis of a time-mean surface momentum or

vorticity equation using observed wind data (Lander 1987, Murphree and van den Douk 1988, Zebiak 1990). It has been suggested by many authors (e.g., Seager 1991) that the difficulty in modeling tropical flows with simple models lies in the treatment of diabatic heating and not in the linear dynamics.

The simplest way to judge the relative importance of different terms in the surface momentum budget is to diagnose these terms based on observation. Consider a general form of nonlinear time-mean momentum equations in a well-mixed surface layer:

$$R_1 = P_1 + C_1 + A_1 \quad (2.2.1a)$$

$$R_2 = P_2 + C_2 + A_2 \quad (2.2.1b)$$

where P stands for the pressure gradient force, C the Coriolis force, A the inertial force or nonlinear mean advection effect, and R the residual term which consists of frictional and time-mean transient effects. The subscripts 1 and 2 represent zonal and meridional direction, respectively.

Figure 2 shows the horizontal distribution of the four terms computed using observed climatological annual mean sea-level pressure and wind fields. There are several important features:

(1) The pressure gradient force and Coriolis force have opposite signs and comparable magnitudes except near the

equator within 3-5° latitude. Both fields have a dominant meridional component.

(2) The inertial force (or nonlinear mean momentum advection) can be neglected compared to the pressure gradient force and Coriolis force.

(3) The residual force which consists of frictional and nonlinear transient effects has a comparable magnitude with the pressure gradient and Coriolis forces. The direction of the residual force is generally in agreement with the observed surface wind field, particularly in trade wind regions. This agreement suggests that the combined frictional and transient effects may be parameterized by, to the first approximation, a form of Rayleigh friction.

Further investigation indicates that there are some particular areas where zonal/meridional wind has opposite signs from residual force  $R_1/R_2$ , as shown in Figures 3a/3b. These particular areas define an important dynamical region in the tropical boundary layer where the traditional three-force balance in the atmospheric boundary layer breaks down. In these regions, the nonlinearity of transient effect plays an important role in maintaining the momentum balance. For zonal momentum balance, the particular dynamical region is mainly in the north eastern Pacific summer monsoon region and the equatorial western Pacific. The prominent feature of onset of the north eastern Pacific summer monsoon is the establishment of westerly flow south of monsoon trough (Murakami et al.

1992). The development of warm SST and strong convection enhances transient activity which further affects mean flow. Therefore, the absence of transient effects, as assumed in the linear dynamics of the Gill model, could result in failure to simulate monsoon westerlies. The transient effects in these particular regions, shown in Figure 3a, can be thought as a momentum source. For meridional momentum balance, the particular dynamical region is in the south Pacific convergence zone (SPCZ) and extra-tropical region. It follows that in these particular regions, the linear dynamics in the Gill-type model fails to produce tropical low-level (surface) flows.

The linear dynamics in a simple Gill model can read

$$E_1 u - \beta y v = -\partial \phi / \partial x \quad (2.2.2a)$$

$$E_2 v + \beta y u = -\partial \phi / \partial y \quad (2.2.2b)$$

where  $u, v$  and  $\phi$  represent low-level (or 1000 mb) zonal and meridional wind components and geopotential height. The Rayleigh friction coefficients  $E_1$  and  $E_2$  are usually assumed to be the same and constant. In reality, the two friction coefficients could be different and change with space and time. For example, the friction coefficient might be larger over land than that over the ocean. Since the model dynamics does not include other physical processes such as transient effects, the friction coefficients could have large

variations. Figure 4 shows the horizontal distribution of friction coefficients  $E_1$  and  $E_2$  calculated by using observed annual mean SLP and surface winds through Equations (2.2.2ab). The sea-level pressure field has been transferred to the geopotential height at 1000 mb according to hydrostatic relationship. To avoid negative and extremely large positive values, the regions where the calculated friction coefficients,  $E_1$  and  $E_2$ , are greater than  $3 \times 10^{-5} \text{ s}^{-1}$  or smaller than  $3 \times 10^{-6} \text{ s}^{-1}$  were blanked out and interpolation was used to obtain modified values. The corresponding damping time scales for the maximum and minimum values of the friction coefficients (i.e.,  $3 \times 10^{-5} \text{ s}^{-1}$  and  $3 \times 10^{-6} \text{ s}^{-1}$ ) are approximately 3 days and 8 hours, respectively. The friction coefficients in the regions where  $u$  and  $v$  are less than 0.5 m/s are also interpolated.

One important feature found in Figure 4 is that the zonal friction coefficient  $E_1$  (Figure 4a) is much smaller than the meridional friction coefficient  $E_2$  (Figure 4b), particularly in the equatorial region where  $E_1$  is up to 3-5 times smaller than  $E_2$ . It is physically reasonable since larger (smaller) zonal (meridional) wind is forced by smaller (larger) zonal (meridional) pressure gradient in the equator. The friction coefficients generally tend to increase with latitude and have larger values over land than over the ocean.

It is noted from Figure 4 that the meridional variations of both  $E_1$  and  $E_2$  are much larger than the corresponding zonal

variations. Figures 5a and 5b illustrate the zonally-averaged friction coefficients  $E_1$  and  $E_2$ . Climatological monthly mean SLP and surface wind are used in these calculations. The 12-month-mean  $E_1$  and  $E_2$  is shown in Figures 5c and 5d. It is noted that both zonal and meridional friction coefficients show systematic change with latitude for all 12 months. Therefore, the zonally-averaged annual mean friction coefficients can be used as a time-independent quantity in the simulation of annual cycle of surface winds. Generally, the zonal friction coefficient is smallest at the equator and increases with latitude. The meridional friction coefficient is also smallest in the equator but shows a maximum value around  $20^\circ\text{N}$  or  $20^\circ\text{S}$ . Both zonal and meridional friction coefficients are approximately symmetric with respect to the equator. Near the equator between  $10^\circ\text{S}$  and  $10^\circ\text{N}$  the annual mean zonally-averaged  $E_2$  is 2-2.5 times as large as  $E_1$ . This result agrees with Deser's (1993) recent study.

The use of the direction- and latitude- dependent Rayleigh friction coefficients is critical in improving the model behavior in simulating low-level (or surface) circulations in the Gill model. Figure 6 shows the difference between simulated and observed winds using the direction- and latitude- dependent annual-mean friction coefficients as illustrated in Figures 5c and 5d. Climatological annual mean sea-level pressure is used in this calculation. The friction over land is set 5 times as large as over the ocean. A nine-

point smoothing method (Liao and Wang 1986) is applied in the calculation of the surface wind field, namely,  $F_{ij}^{NEW} = (1-s^2) f_{ij} + 0.5 s(1-s) (f_{i+1j} + f_{i-1j} + f_{ij+1} + f_{ij-1}) + 0.25 s^2 (f_{i+1j+1} + f_{i-1j-1} + f_{i-1j+1} + f_{i+1j-1})$ , where the smoothing coefficient,  $s$ , is set to be 0.5. It is found that the difference between simulation and observation is, in most region, less than 1 m/s in both zonal and meridional components. Thus, the magnitude and location of both zonal and meridional winds are well simulated. For instance, the simulated trade winds and equatorial easterly flows are both close to the observed. The convergence along ITCZ is well reproduced.

As a comparison with the direction- and latitude-dependent friction coefficients, the simulation with a constant zonal and meridional friction coefficient ( $E_1=E_2=10^{-5} s^{-1}$ ) is performed. This constant friction coefficient corresponds to a damping time scale of 1 day and is used by many authors (e.g., Zebiak 1982, Davey and Gill 1987). The same smoothing as in the previous calculation is used. The difference between simulated and observed winds is shown in Figure 7. It is found that the simulated trade wind between  $10^\circ N$  to  $20^\circ N$  is too strong and too zonal. The equatorial easterly within  $10^\circ S$  and  $10^\circ N$  is relatively weak with a maximum error of 1-2 m/s in the eastern equatorial Pacific. The largest errors in the zonal component (greater than 3 m/s) occur along the coast of Mexico and Central America. The most serious problem is the simulation of meridional wind component

in the equatorial eastern Pacific where the error is up to 7 m/s. The large error in meridional wind directly affects convergence field near the ITCZ. Further sensitivity tests indicate that decreasing friction coefficient can increase equatorial easterly, but the trade wind becomes more zonal and the cross-equatorial meridional wind becomes unrealistically large. As a result, the corresponding convergence field in the equatorial region becomes worse. With an increased friction coefficient, the simulated trade winds are close to the observed, but the equatorial easterly becomes too weak. It is concluded that the direction- and latitude-dependent Rayleigh friction coefficients are important in simulating surface (or low-level) winds in a simple Gill-type model.

### 2.2.2 Thermodynamics problems

Wang and Li (1993) proposed a two and one-half layer tropical atmosphere model (the WL model) to study the response of atmospheric circulations to SST forcing. The nondimensional thermodynamic equation in the WL model can be written as:

$$\begin{array}{ccccccc}
 N(\phi - \phi_{eq}) & + & (1 - \delta I) \nabla \nabla & = & d(\delta B - 1) \nabla \nabla_B & - & \delta F |\nabla_B| (q_s - q_l) & (2.2.3) \\
 \text{A1} & & \text{A2} & & \text{A3} & & \text{A4} & 
 \end{array}$$

where  $\phi$  represents lower-troposphere geopotential height (or thickness between upper and lower troposphere),  $\phi_{eq}$  represents an equilibrium state of the geopotential height which is

assumed to be a function of SST,  $V$  and  $V_B$  represent, respectively, the lower-troposphere and boundary-layer winds. The nondimensional parameters  $I$  and  $B$  represent the heating intensities in the free atmosphere and boundary layer, which are related to SST. The evaporation coefficient  $F$  is a constant which depends on the drag coefficient and boundary-layer depth. The Newtonian cooling coefficient,  $N$ , represents an inverse of the time scale during which the geopotential height relaxes to its equilibrium state. The parameter  $d$  is a nondimensional boundary-layer depth. The nonlinear-heating switch-on coefficient,  $\delta$ , is important for taking into account the SST effect on convective instability. It linearly increase from 0 to 1 when SST changes from 25.5°C to 28.5°C. It is equal to zero when SST is below 25.5°C and remains one when SST is larger than 28.5°C. The detailed derivation can be found in Wang and Li (1993).

Term A1 in Equation (2.2.3) stands for the Newtonian cooling process, term A2 the effect of adiabatic and diabatic processes associated with lower-troposphere convergence, term A3 the effect of adiabatic and diabatic processes associated with boundary-layer convergence, and term A4 the evaporational effect. The thermodynamic Equation (2.2.3) can be transferred to that of Davey and Gill (1987) if the boundary-layer process and evaporation (i.e., term A3 and A4) are dropped. It becomes that of Zebiak (1982, 1986) when the boundary-layer term (A3)

and the equilibrium geopotential height ( $\phi_{eq}$ ) in term A1 are not included.

Thermodynamic equation (2.2.3) is diagnosed using observed annual mean SST and surface and 850 mb winds. Figure 8a shows the diagnosed annual mean lower-troposphere geopotential height field based on the model thermodynamic equation. For comparison with the diagnosed field, Figure 8b illustrates annual mean 850 mb geopotential height field calculated from observed annual mean sea-level pressure with an approximated boundary-layer temperature profile proposed by Lindzen and Nigam (1987). The result in Figure 8b is regarded as observation. The diagnosed subtropical highs in both hemispheres are severely underestimated. The low-pressure system in the western Pacific is, on the other hand, overestimated. Generally, the model-diagnosed geopotential height is too close to the SST field. There is an obvious east-west phase difference between the diagnosed and observed subtropical highs. For instance, the center of the observed subtropical high in the southern hemisphere is located at 100°W whereas the diagnosed center is east of 90°W. In the northern hemisphere, the observed subtropical high center is located at 140°W but the simulated is at 110°W. It is difficult to use such a diagnosed geopotential height field to simulate realistic trade winds.

The discrepancies arise partially from the model assumptions in parameterization of Newtonian cooling. In term

$A_1$  of Equation (2.2.3), the equilibrium geopotential height is, according to hydrostatic relationship, related to mid-troposphere equilibrium temperature perturbation which is further assumed to have the same horizontal distribution as the SST perturbation with a reduced amplitude (Davey and Gill 1987, Wang and Li 1993). In reality, the relationship between the mid-troposphere and surface temperature perturbations must be complicated and change with time and space. Consider a general formula between the mid-troposphere temperature perturbation,  $T_{eq}'$ , and the SST anomaly,  $T_s'$ , namely

$$T_{eq}' = T_s' + \gamma'(p_1 - p_2) \quad (2.2.4)$$

where  $\gamma'$  is the perturbation lapse rate,  $p_1=1000$  mb, and  $p_2=475$  mb when the top of the boundary layer is at 850 mb. The perturbation lapse rate is generally not constant in space and time. For instance, the lapse rate in the deep convection regions where the temperature profile reaches a saturated adiabatic lapse rate should be much different from that in the subtropical high or strong inversion regions. The phase shift between observed SST and SLP fields in the north and south eastern Pacific (Fig. 1) also suggests a geographically-dependent vertical temperature profile.

The perturbation lapse rates (as shown in Figure 9) are diagnosed from Equation (2.2.3) by applying the hydrostatic relationship between  $\phi_{eq}$  and  $T_{eq}'$  and Equation (2.2.4). The

maximum positive perturbation lapse rates occur in the north western Pacific, the south Pacific convergence zone (SPCZ), and the north eastern Pacific. The negative perturbation lapse rates appear in Australia and North America, subtropical regions, and the coast of the South America. The amplitude of the perturbation lapse rate is around  $10 \cdot 10^{-5}$  °C/Pa (approximately 1°C/km). The positive perturbation lapse rate implies a larger temperature decrease with height and a colder temperature in mid troposphere or a higher pressure at sea surface. The east-west contrast between the positive and negative perturbation lapse rates in the north and south eastern Pacific cold tongue regions is critical for the phase shift between the lowest SST and the highest SLP.

The annual cycle of the computed perturbation lapse rate is illustrated in Figure 10. In the north eastern Pacific around 5°N, the lapse rates are negative in January with an amplitude of  $-4 \cdot 10^{-5}$  °C/Pa. They become positive in July with an amplitude of  $8-10 \cdot 10^{-5}$  °C/Pa. In the north western Pacific, the maximum positive perturbation lapse rate is at 10°N in January and moves to 20°N in July. In the southern hemisphere, the maximum positive perturbation lapse rate approaches 110°W in January and retreats to 160°W in April and 160°E in July. The maximum negative perturbation lapse rate occurs in Australia in October and in the North America in April.

Overall, the diagnosed perturbation lapse rate shows a complicated annual variation. Without proper description of

annual variation of the perturbation lapse rate, it is difficult to simulate the realistic strength, location, and time variations of the subtropical highs in the WL model.

### 2.3 The model

Consider a hydrostatic equilibrium troposphere with a vertically averaged lapse rate  $\gamma$ , i.e.,  $T(z)=T_s -\gamma z$ , where  $T_s$  is surface air temperature which, for simplicity, is assumed to be equal to sea surface temperature,  $T_s$  (an experiment with  $T_s=T_s-1$  shows that the simplification does not affect model results). The top of the troposphere is assumed undisturbed with constant pressure ( $p_u$ ) and height  $H$ . This assumption is approximately valid for the tropical troposphere between 20°N and 20°S. For a hydrostatic equilibrium atmosphere,

$$\partial p/\partial z=-gp/RT \quad (2.3.1)$$

where  $p$ ,  $g$ , and  $R$  represent the pressure, gravity, and gas constant for dry air. Integrating (2.3.1) vertically from surface  $z=0$  to the tropopause  $z=Z_u$  yields

$$\ln(P_s/P_u)=(g/R\gamma) \ln[T_s/(T_s-\gamma Z_u)] \quad (2.3.2)$$

where  $P_s$  stands for SLP. For a constant mean lapse rate (6°C/km) and a tropopause at 100 mb, the height of the tropopause is 16.8 km as determined by (2.3.2) if domain-

averaged (120°E-80°W, 30°S-30°N) climatological annual mean SST and SLP are used as reference temperature and pressure. The calculated tropopause height is close to the observed value in the tropics.

Generally speaking, the lapse rate  $\gamma$  changes with time and space. By applying climatological monthly mean SST and SLP data in Equation (2.3.2), we can compute mean geographic distribution of the vertically averaged lapse rate for January through December. Figure 11 shows the model diagnosed  $\gamma$  field. Note that the lapse rates shown in Figure 11 display a reasonable range of variation from 6.4°C/km to 5.4°C/km.

To compare the diagnosed lapse rate with observation, a so called observed lapse rate was calculated using ECMWF's analyzed 200mb and 850mb geopotential height climatology (Li and Wang 1992). Both lapse rates show similar amplitudes and spatial and temporal variations. The largest difference lies in subtropical regions (north or south of 20°N or 20°S).

Figure 11 shows that large lapse rates occur in high SST regions. The annual variation of the lapse rate exhibits a systematic meridional migration in the western Pacific and westward propagation in the equatorial eastern Pacific. The annual variation of the lapse rate appears to be in harmony with that of SST field. In fact, there is high correlation between SST and the diagnosed lapse rate. The linear correlation coefficient which is calculated for the entire tropical Pacific domain (120°E-80°W and 30°S-30°N) and for all

12 months (sample size: 30132), is 0.99. The linear regression equation for the lapse rate can be expressed as

$$\gamma_{\text{regression}} (\text{°C/km}) = 10^{-3} [0.106719T_s (\text{°C}) + 3.26009] \quad (2.3.3)$$

Using this empirical formula, an estimate of lapse rate can be made from SST. The results indicate that the estimated lapse rate captures the most important features of spatial and temporal variabilities of the vertically averaged lapse rate field. The difference between the estimated (from empirical relationship (2.3.3)) and diagnosed (based on observation) lapse rates is quite small. The maximum error is smaller than 0.05°C/km. More importantly, inspection of the difference for all 12 months (not shown) reveals that there is a systematic bias between the estimated and diagnosed fields. The 12-month-averaged bias (estimated minus diagnosed lapse rate) is shown in Figure 12. There are two negative centers in the subtropical high regions of the respective hemisphere, indicating that a larger-than-estimated lapse rate in these regions is needed. This implies that in the subtropical high regions the estimated mean tropospheric temperature is systematically higher than the observed and the estimated SLP is systematically lower than the observed. Two areas of major positive bias are found in the SST cold tongue regions along the coast of South America and Mexico. Over those regions the model tends to underestimate the mean tropospheric

temperature. It is worth noting that the annual variation of the bias is negligible. Therefore, the bias is nearly season-independent and is primarily a function of geographic location. This bias must be due to processes, such as transient effects, which are not described by the model. It follows that the time-independent bias can be included for a steady state climate model by

$$\gamma = \gamma_{\text{regression}} + \gamma_{\text{bias}} \quad (2.3.4)$$

The premise involved here is that the lapse rate is determined by SST and other unresolved free atmospheric processes, especially the transient and radiational effects. The latter is related to the nature of mean climate systems.

Substitution of (2.3.3) and (2.3.4) into (2.3.2) results in a single equation to predict SLP, given a SST field and the time-independent bias which is empirically determined from climatological data (Figure 12). Once sea-level pressure is known, surface winds can be computed using the surface momentum balance equations (2.2.1ab) and the direction- and latitude-dependent Rayleigh friction coefficients. The precipitation rate,  $P_r$ , is determined from a moisture budget by taking into account the effects of SST on convective instability, following the WL model:

$$P_r = \delta \lambda \{ -\rho_a \Delta z \nabla \cdot (q_a \nabla_B) + \rho_a C_D |\nabla_B| (q_s - q_a) \} \quad (2.3.5)$$

where  $q_s$  is sea surface specific humidity which is function of SST and SLP according to the Clausius-Clapeyron equation,  $C_D$  is drag coefficient (0.0015),  $V_B$  represents surface wind,  $\rho_a$  is surface air density (1.2 kg/m<sup>3</sup>),  $\lambda$  is a fraction (0.75) which represents the precipitation efficiency, following Kuo (1974),  $\delta$  is a SST-dependent nonlinear heating switch-on coefficient, as proposed by Wang and Li (1993), and  $\Delta z$  is the depth of boundary layer (1500 m). Here we have assumed that moisture convergence takes place only in the well-mixed boundary layer. Surface air specific humidity ( $q_s$ ) can be empirically decided since there is a high correlation between climatological monthly mean SST and  $q_s$ . The correlation between the SST and  $q_s$  for all 12 months within model domain exceeds 0.99. The data of surface air specific humidity are derived by Esbensen and Kushnir (1981) with a resolution of 5 degrees longitude by 4 degrees latitude. The linear regression equation between SST and  $q_s$  can be written as

$$q_s = 10^3[0.972T_s(^{\circ}\text{C})-8.92]. \quad (2.3.6)$$

#### 2.4 Simulation of the annual cycle of the tropical Pacific atmosphere

Annual variation of tropical Pacific SLP, surface winds, and precipitation are simulated using the present model forced by climatological monthly mean SST. The domain of the forcing spans 120°E to 80°W and 30°S to 30°N with a resolution of 2

degrees longitude by 2 degrees latitude. The same smoothing method as in section 2.2.1 is applied in the calculation of surface wind fields. Figure 13 presents simulated monthly mean SLP fields. The simulations can be compared with the observed fields, as shown in Figure 1a. It is obvious that the simple model is able to reproduce most fundamental features of the annual cycle of SLP. For instance, the position and intensity of the subtropical highs in both hemispheres are well simulated. The low-pressure system in the western Pacific shows clear meridional migration with maximum intensity occurring in the summer hemisphere. The trade wind trough shows a seasonal shift with maximum intensity along 5°N in January and up to 10°N in July. The pressure difference between the simulated and observed fields is within 1-2 mb in most regions.

Figures 14a and 14b show simulated and observed surface wind fields. The trade winds in both hemispheres are well simulated. In the western Pacific, there is an obvious annual variation of monsoon circulation with reversed cross-equatorial flow from winter to summer hemispheres. In the eastern Pacific, the cross-equatorial southerly component reaches a maximum in July and October when the ITCZ or eastern North Pacific monsoon trough reaches its northernmost position. The southwesterly flow is also found north of the equator during the eastern North Pacific summer monsoon. The trade wind convergence zone (the ITCZ in the central Pacific)

is found close to the equator in April and at its northernmost location in October. The South Pacific convergence zone (SPCZ) is strongest in January but nearly disappears in July because the northerly component occurs in 5-10°S around 180-160°W in January but not in July.

The annual cycle of precipitation pattern shows consistent features with surface wind and pressure variation. Figure 15a illustrates the mean precipitation rate in January, April, July, and October. As an indirect comparison, observed climatological monthly Highly Reflective Cloud (HRC) data derived by Garcia (1985) are displayed for corresponding months (Figure 15b). According to Wang (1992a), a monthly mean value of HRC of 3 days/month corresponds approximately to a rainfall rate of 7 mm/day. The precipitation along SPCZ shows the strongest phase in January with the contour of 3 mm/day extending eastward to 140°W and the weakest phase in July with the same contour retreating back to 160°W. In the western Pacific, the precipitation center moves toward the northern hemisphere during northern spring. The maximum precipitation in the western Pacific reaches 15 mm/day, which is a reasonable magnitude compared with the climatological precipitation rate there (e.g., Taylor 1973). In the eastern Pacific, maximum precipitation is consistent with the development of the eastern North Pacific monsoon circulation. The simulated precipitation rate along the ITCZ in the central Pacific shows a maximum in October and a minimum in January,

which is also in agreement with observations (Wang 1992a). The major discrepancy of the simulated precipitation field lies in its strength in the SPCZ region during the northern winter where the observed Highly Reflective Cloud shows the maximum value. Because SPCZ is a deep convergence zone in the lower troposphere, whereas the model precipitation only takes boundary layer moisture convergence into account, this discrepancy is expected. It may be improved by assuming a space-varying depth of boundary layer.

## 2.5 The response of tropical atmosphere to symmetric and antisymmetric SST forcing

The annual variation of Pacific SST is alternatively dominated by a quasi-symmetric equatorial mode with the maximum amplitude in late spring/fall and an antisymmetric monsoonal mode with the maximum amplitude in late summer/winter (Wang 1992b). The former is a consequence of coupled air-sea interaction and the latter reflects a response to global solar radiation forcing. In this section, I investigate how the atmosphere responds to the symmetric and antisymmetric SST modes.

Following Wang (1992b), climatological monthly anomalous SST is divided into a symmetric and an antisymmetric mode in reference to the equator. The atmospheric response to annual mean SST is first obtained by forcing the model towards an equilibrium state. This solution is referred to as an annual

mean solution. Then the atmospheric response to the sum of the annual mean SST and a symmetric (or antisymmetric) mode is obtained. The solution is referred to as the total solution. Finally, the response of atmosphere to the symmetric (or antisymmetric) SST forcing is obtained by subtracting the total solution from the annual mean solution.

Figure 16 shows that the symmetric SST mode exhibits a systematic westward phase propagation along the equator. In January, there is a weak positive SST anomaly occurring in the equatorial eastern Pacific near the coast of South America. It then intensifies and propagates westward. By March, the maximum anomaly moves to 100°W with an amplitude of 2.6°C, and the front of the positive anomaly approaches 150°W. In addition to the westward propagation, the SST anomaly also expands poleward. In May, the maximum anomaly occurs at 5-10° latitude. When the positive SST anomaly continues to move westward, a cold SST center occurs in the equatorial eastern Pacific in July (an approximately opposite image to January). The anomalous cold SST evolves in a similar way as that of the anomalous warm SST.

The atmospheric response to the symmetric SST forcing is illustrated in Figure 17. The atmospheric zonal wind component, precipitation and sea-level pressure all show, along the equator, a westward propagation similar to that in SST. For example, the maximum anomalous precipitation occurs in March around 100°W with a magnitude of 10 mm/day and

propagates to 140°W in April (7.0 mm/day) and 170°W in June (9.4 mm/day). The meridional wind component, however, does not show any significant westward phase propagation, which is consistent with observations. The maximum anomalous SLP is at 100°W with a magnitude of 2.5 mb. The magnitude of the westerly wind anomaly is about 3.7 m/s and the amplitude for the meridional anomaly is about 1 m/s. There is a phase difference between the zonal wind and SST along the equator. The westerly lies west of the maximum anomalous warm SST. The maximum precipitation occurs in March at 100°W and moves to 170°W in June and 140°E in August. The sea-level pressure shows a semi-annual variation in the western Pacific and an annual oscillation in the eastern-central Pacific.

Inspection of the antisymmetric SST mode (not shown) indicates that there are dominant meridional variations throughout the year. The amplitude of the zonal-average antisymmetric SST mode (Figure 18) is about 3°C far away from the equator (at 30°N and 30°S). The maximum warming of the antisymmetric mode occurs in February in the southern hemisphere and shifts to the northern hemisphere in August in response to the solar radiation forcing.

Figure 19 shows the atmospheric response to the antisymmetric SST forcing. The maximum precipitation occurs at 5-10°S or N, along the climatological convergence zones: the intertropical convergence zone and south Pacific convergence zone. The maximum precipitation rate is about 4.2 mm/day in

September along the ITCZ and 1.5 mm/day in April along the SPCZ. Compared with the structure and evolution of the antisymmetric SST mode, the sea-level pressure field shows similar characteristics, with the maximum low pressure center at 30°S in the northern winter (February) and at 30°N in the northern summer (August). The surface winds exhibit a monsoonal pattern, with the westerly anomaly occurring in the summer hemisphere and the cross-equatorial flow from the winter hemisphere. The maximum zonal wind component occurs in February and August-September with a magnitude of 1.7 m/s. The maximum meridional wind component occurs in March and September in the equator with an amplitude of 2.8 m/s. These results generally agree with the observed antisymmetric mode in OLR, SLP and surface wind fields (Figure 18).

CHAPTER THREE  
ON THE ANNUAL CYCLE OF THE TROPICAL PACIFIC  
SEA SURFACE TEMPERATURE

3.1 Introduction

Studies in the tropical atmosphere-ocean interaction have indicated that the primary direct influence of the ocean on the atmosphere is through sea surface temperature (Zebiak and Cane, Schopf and Suarez 1988, Philander 1990). Atmospheric influence on the sea surface temperature, on the other hand, is rather complicated. This is because both dynamic (e.g., surface wind stress) and thermodynamic (e.g., surface heat fluxes) processes contribute to the SST change. Although the surface wind stress is a major cause of the positive feedback through coupled instability during the El Nino/Southern Oscillation (Philander et al. 1984), quantities such as air surface temperature and humidity as well as cloudiness, which all affect net surface heat flux, are also important in the annual cycle of the sea surface temperature in the tropical Pacific.

Annual variation of sea surface temperature shows the clear signals of westward propagation along the equator and northward propagation along the eastern Pacific (Figures 20a and 20b). It is found from Figure 20a that the maximum positive SST anomaly (with a magnitude of  $2.8^{\circ}\text{C}$ ) occurs in March around  $100^{\circ}\text{W}$ . The positive SST anomaly then propagates

westward from the eastern Pacific to the date line in June. While the positive anomaly continues to propagate westward, a negative SST anomaly occurs in the equatorial eastern Pacific. It also propagates westward. It is noted that a semi-annual SST variation appears in the equatorial western Pacific while an annual variation of the SST occurs in the eastern-central Pacific. In the time-latitude profile of the SST anomaly along 100-110°W (Figure 20b), there is prominent northward propagation. A positive SST anomaly occurs at 30°S in February and moves northward to the equator in April. Similar to the time evolution of the positive SST anomaly, a negative SST anomaly appears at 30°S in August and at the equator in October.

A key question related to the observed phenomena is what physical processes are responsible for the westward propagation of the SST anomaly along the equator and for the northward propagation of the SST anomaly in the eastern Pacific. This forms the first motivation of the present study.

Physically, there are two essential types of processes which can change the sea surface temperature. One is the thermal forcing through which ocean surface gets heat from the solar radiation, emits longwave radiation, and loses the latent and sensible heat to atmosphere. Another is the wind-induced dynamical process which includes turbulent mixing and horizontal temperature advection by oceanic currents. So far,

it is not clear which process plays a key role in determining the annual variation of the Pacific SST.

The annual variation of equatorial western Pacific surface wind may have remote influences on the equatorial eastern Pacific SST through oceanic wave dynamics (Lukas 1981, Wang 1992b). Equatorial oceanic waves such as Kelvin and Rossby waves may carry information away from the local wind forcing region and cause remote response. It was observed from the eastward transport and sea level signal that there is eastward propagation with a phase speed of 2-3 m/s due to a strong April 1980 westerly burst in the western Pacific (Knox and Halpern 1982). Lukas et al. (1984) analyzed the phase speed of sea level records from a number of island stations during the onset of the 1982-83 ENSO and found that the propagation modes are the first and second vertical-mode Kelvin waves. It is observed from climatological surface wind data that both total and anomalous zonal winds in the equatorial western Pacific are westerlies during the northern winter (Sadler et al. 1987), and two month later, a warm SST anomaly occurs in the equatorial eastern Pacific around 85°W (Wang 1992b). Are the two phenomena related? This forms the second motivation for the present study.

Climatological annual mean cloudiness derived from Esbensen and Kushnir (1981) shows distinct spatial distribution in comparison with climatological annual mean highly reflective cloud data (Garcia 1985). Figure 21 shows

the two fields. Note that the maximum HRC along the ITCZ and SPCZ is one order of magnitude larger than that in the eastern Pacific subtropical high region. The pattern of HRC coincides well with observed annual precipitation field derived by Taylor (1973) (Figure omitted). The ratio between the eastern and western Pacific in the annual mean cloudiness field, on the other hand, is quite large (about 2/3). For instance, the annual mean cloud cover is about 0.4-0.5 in the eastern Pacific and about 0.7-0.8 in the equatorial western Pacific. The difference is because there are a number of low stratus (non-convection) clouds in the eastern Pacific and subtropical high regions due to strong inversion and due to cold SST.

The indication is that there is difficulty in parameterizing annual mean cloudiness using either observed or model-output precipitation. However, inspection of monthly mean cloudiness and precipitation anomalies indicates that there is some similarity in the two fields. Figure 22 illustrates January and July cloudiness anomaly fields. The positive anomaly is found along the SPCZ and the north Australia monsoon region in January while negative anomaly is found in July. In the north eastern Pacific, the positive anomaly of monthly mean cloud cover occurs in July and the negative anomaly is in January. The features are consistent with the seasonal variations of simulated anomalous precipitation fields (see Figure 15a).

The amplitude of annual variation of the cloudiness is quite small compared with its annual mean value. For example, the maximum mean cloud cover in the equatorial western Pacific (around 150°E) is about 0.78 whereas the anomaly is only about 0.1. In the subtropical high region, the annual mean value of cloudiness is 0.4-0.5 while the anomaly is about 0.05. Does such a small variation of cloudiness affect the change in SST? This question forms the third motivation.

The purpose of this study is to numerically investigate the physical mechanisms which affect the SST in the tropical Pacific Ocean. In Section 3.2, a reduced-gravity ocean model is described. To identify the relative importance of the dynamic and thermodynamic processes in the SST change, four experiments are designed in Section 3.3 in terms of annual mean and annual cycle of surface wind and heat flux forcing. In Section 3.4, I investigate the influences of remote and local wind forcing and effects of oceanic waves on the SST variations. Results from two experiments are analyzed in Section 3.5 to examine the effects of annual variations of cloudiness on the SST change.

### 3.2 The model description

The ocean model used in this study is an extension of the conventional 1.5 layer reduced gravity system, following that of Cane (1979), Zebiak and Cane (1987), and Seager et al. (1988). It describes the linear dynamics of an homogeneous

upper layer with a varying thermocline that overlies a motionless abyssal layer with a constant temperature. A constant buoyancy is assumed in the upper ocean ( $b=5.6 \text{ cm/s}^2$ ) which corresponds to a Kelvin wave speed of 290 cm/s for a mean thermocline depth of 150 m. The equations for mean upper-ocean currents ( $\mathbf{u}$ ) and thermocline depth ( $h$ ) can be written as:

$$\partial \mathbf{u} / \partial t + f \mathbf{k} \times \mathbf{u} + \nabla b h = \tau / H + \mu \nabla^2 \mathbf{u} - r \mathbf{u} \quad (3.2.1)$$

$$\partial h / \partial t + H \nabla \cdot (\mathbf{u}) = -r h \quad (3.2.2)$$

where  $\tau$ ,  $\mu$ ,  $r$ , and  $H$  represent the surface wind stress, the diffusion coefficient, the Rayleigh friction coefficient, and the mean depth of thermocline, respectively. Following Zebiak and Cane (1987) and Seager et al. (1988), a constant surface frictional (Ekman) layer is included in the upper ocean to capture the intensity of wind driven surface currents. Therefore, the vertically averaged currents in the upper ocean can be expressed as  $\mathbf{u} = (H_1 \mathbf{u}_1 + H_2 \mathbf{u}_2) / H$ , where subscripts 1 and 2 refer to the surface layer and underlying layer, respectively.

The equations governing the shear between layers 1 and 2 can be written as

$$r_s u_s - f v_s = \tau^{(x)} / \rho_o H_1 \quad (3.2.3a)$$

$$r_s v_s + f u_s = \tau^{(y)} / \rho_o H_1 \quad (3.2.3b)$$

where  $u_i = u_1 - u_2$  and  $\tau^{(x)}$  and  $\tau^{(y)}$  are wind stress in zonal and meridional directions, respectively.

The entrainment velocity (which equals the upwelling velocity for a constant depth mixed layer) at the base of surface layer is determined from the Ekman divergence of the surface-layer currents, namely,

$$w_e = H_1 (\partial u_1 / \partial x + \partial v_1 / \partial y) \quad (3.2.4)$$

The model allows prediction of sea surface temperature. The mean temperature in the surface layer can be written as

$$\partial T / \partial t + u_1 \nabla T = Q / \rho_0 C_w H_1 + \kappa \nabla^2 T - w_e H(w_e) (T - T_e) / H_1 \quad (3.2.5)$$

where  $T_e$  is temperature of entrained water below the constant mixed layer,  $\rho_0$  and  $C_w$  are the density and specific heat of water,  $Q$  is diabatic heating in the mixed layer, and  $H(x)$  is a heavyside step function which equals to 1 when  $x > 0$  and equals to 0 when  $x < 0$ . The equation (3.2.5) shows that the change in SST depends on horizontal advection, vertical advection, and surface heat fluxes.

So far there are a number of maps showing the annual mean net surface heat flux at the tropical Pacific Ocean basin (e.g., Wyrтки 1965, Esbensen and Kushnir 1981, Weare et al. 1981). These maps are estimated from marine climate data using various empirical formulas. There is considerable uncertainty

regarding the pattern and magnitude of the surface heat flux. For example, Weare et al. show a large downward annual mean net heat flux ( $60 \text{ Wm}^{-2}$ ) over the equatorial western Pacific around  $140\text{-}160^\circ\text{E}$  whereas Esbensen and Kushnir's data show a value of  $20 \text{ Wm}^{-2}$ . If the mean net heat flux has an error of  $40 \text{ Wm}^{-2}$ , the surface temperature with a typical mixed layer depth of  $50 \text{ m}$  will change at a rate of  $6^\circ\text{C yr}^{-1}$ , which is greater than that observed in ENSO transitions (Webster and Lukas 1992). Gordon and Corry (1991) simulated the seasonal cycle in the tropical Pacific ocean using an ocean GCM model in which a flux correction term, in addition to observed surface heat flux, is added to the diabatic heating term, namely,  $Q = Q(T_c) - \eta(T - T^*)$ , where  $Q(T_c)$  is the observed net heat flux,  $T^*$  is taken to be the climatological monthly mean SST, and  $\eta$  is assigned a value of  $35 \text{ Wm}^{-2}\text{K}^{-1}$  which corresponds to a Newtonian cooling time scale of two months for a mean mixed layer depth of  $50 \text{ m}$  ( $\rho_r C_w H_1 / \eta$ ). In the present study,  $T^*$  is set as climatological annual mean SST rather than monthly mean SST so that the simulated SST is relaxed only toward the annual mean SST and the flux correction has little effect on the annual variation of SST. A value of  $14 \text{ Wm}^{-2}\text{K}^{-1}$  for  $\eta$  is taken in the present study so that the relaxation time extends to 5 months. This value is supported by Gent's (1991) recent study for the heat budget in the TOGA-COARE domain. The climatological surface heat fluxes of Esbensen and Kushnir (1981) are used in the present study.

The solar radiation in the model is allowed to penetrate below the base of the mixed layer according to a "two band" approximation. Therefore, the climatological net heat flux in the surface temperature equation can be written as:

$$Q(T_c) = Q_1(1-J) - Q_2 \quad (3.2.6)$$

where  $Q_1$  is available insolation flux and  $Q_2$  is the sum of sensible, latent and longwave radiation heat fluxes. The parameter,  $J$ , represents the penetration rate of solar radiation flux down to the base of surface layer which is parameterized as

$$J = R \exp(-H_1/r_1) + (1-R) \exp(-H_1/r_2) \quad (3.2.7)$$

The temperature of entrained water below the base of the mixed layer,  $T_c$ , is given by

$$T_c = \alpha T_{sub} + (1-\alpha) T \quad (3.2.8)$$

where  $\alpha$  is an adjustable parameter taken to be 0.75 and  $T_{sub}$  is temperature below the surface layer which is set to be the climatological annual mean temperature at 50 meters ( $T_{50m}$ ) plus an annual variation. Since the model does not predict the change of  $T_{sub}$ , the change in  $T_{sub}$  is assumed to be related to the variation of thermocline depth. There are several

different formulae relating  $T_{sub}$  and  $h$  (e.g., Zebiak and Cane 1987, Seager et al. 1988, Chang 1993). In the present study, I use a simple relation given by

$$T_{sub} = T_m + (h-h_m)(T_m-T_r)/(h_m-H_1) \quad (3.2.9)$$

where  $T_m$  and  $h_m$  are model-output annual mean surface temperature and thermocline depth and  $T_r$  is the constant reference temperature in the abyss.

The model ocean covers from 120°E to 80°W between 30°S and 30°N with a realistic description of the Pacific ocean boundaries in the east and west sides. The model spatial resolution is 2° longitude by 1° latitude and the time interval is approximately 3 hours. To make sure that the current resolution is proper, a sensitivity test with a twice resolution (1° longitude by 0.5° latitude) was carried out and the results are very close. An absolute potential enstrophy conserving scheme is used and the finite-difference equations are formulated on the staggered C grid in a spherical coordinate. No-flux boundary conditions for temperature and free slip conditions for velocities are applied at the ocean boundaries. At northern and southern boundaries, the large Rayleigh friction and Newtonian damping with a time scale of a half day, which rapidly decay toward the ocean interior, are introduced to eliminate coastal Kelvin waves. The climatological monthly mean surface winds and heat fluxes are

decomposed to 6 harmonics so that their values at each time step can be precisely determined.

The model contains a number of parameters. The values of these parameters are set as following. The density of ocean water,  $\rho_0$ , equals to  $1 \text{ g/cm}^3$ , the air density at surface,  $\rho_a$ , is  $1.2 \times 10^{-3} \text{ g/cm}^3$ , the drag coefficient,  $C_D$ , is set to be  $1.5 \times 10^{-3}$ , the heat capacity of water,  $C_w$ , is  $4.2 \times 10^3 \text{ Jkg}^{-1}\text{K}^{-1}$ , the solar radiation penetration coefficient,  $R$ , is 0.58 and e-folding depths  $r_1$  and  $r_2$  are 35 cm and 2300 cm, respectively, the reference temperature,  $T_r$ , is set  $10^\circ\text{C}$ , the Rayleigh friction coefficient,  $r$ , is set to be  $1/150 \text{ day}^{-1}$ , the diffusion coefficients in momentum and thermodynamic equations,  $\mu$  and  $\kappa$ , are set to be  $5 \times 10^7 \text{ cm}^2/\text{s}$ , the mean depth of thermocline,  $H$ , is 150 m, the depth of the constant surface layer,  $H_1$ , is 50 m, and the Rayleigh friction coefficient in the shear equation (3.2.3),  $r_s$ , is set to be  $2 \text{ day}^{-1}$ .

### 3.3 The response of the tropical Pacific SST to dynamic and thermodynamic forcing: surface wind stresses verse heat fluxes

According to the thermodynamic equation (3.2.5), time change rate of SST depends on two physical processes: the wind-induced dynamic process that includes horizontal and vertical temperature advection and the thermodynamic process associated with surface heat fluxes. To identify the relative importance of the two processes, four experiments are designed. In the first experiment, the model ocean is forced

by both annual mean wind stress and annual mean net surface heat flux. In the second experiment, the annual cycles of wind stress and annual mean of surface heat flux are specified. In the third experiment, the ocean is forced by annual mean of wind stress and annual cycle of heat flux. In the fourth experiment, it is forced by the annual cycles of both wind stress and heat flux. By isolating dynamic and thermodynamic processes, I attempt to understand what physical processes are responsible for the westward propagation of the SST anomaly along the equator and what processes are responsible for the northward propagation of the SST anomaly in the eastern Pacific.

Climatological monthly mean surface winds derived from the COADS data (Sadler et al. 1987) and surface heat fluxes derived from Esbensen and Kushnir (1981) are used in the section.

### 3.3.1 Experiment one: annual mean wind and heat flux forcing

In the first experiment, annual mean SST is simulated using observed annual mean wind stresses and surface heat fluxes as external forcing. The model is integrated for two years and the initial conditions for ocean surface temperature, currents, and thermocline depth are set to be constants and equal  $30^{\circ}\text{C}$ ,  $0 \text{ cm s}^{-1}$ , and 150 m, respectively.

Figure 23 shows the simulated SST and thermocline depth fields. The western Pacific warm pool, the south and north

eastern Pacific cold tongues, and warm water belt ( $27^{\circ}\text{C}$  contour line) along the intertropical convergence zone (ITCZ) are simulated. The error is less than  $1^{\circ}\text{C}$  in most region and the maximum errors occur in the equatorial eastern Pacific ( $1.3^{\circ}\text{C}$ ) and along the North and South America coasts ( $2.8^{\circ}\text{C}$ ). The thermocline depth is shallow in the equatorial eastern Pacific and the coasts of South and North America and is deep in the equatorial western Pacific and subtropical regions.

The major terms influencing SST in the thermodynamic equation (3.2.5) are zonal and meridional temperature advection, vertical temperature advection, and thermal forcing (net heat flux) terms. To examine the relative importance of these terms, I calculated these aforementioned four terms (Figure 24). It is seen from the thermal forcing field that net downward heat flux occurs in the equatorial eastern and western Pacific ocean. The maximum diabatic heating lies at  $110^{\circ}\text{W}$  along the equator. In the subtropics, the surface heat fluxes generally tend to cool the ocean and cause the decrease of sea surface temperature. The wind-induced zonal and vertical temperature advection has a comparable magnitude with the thermal forcing term. The meridional temperature advection is relatively small. The strongest cooling associated with the zonal temperature advection appears in the eastern and central Pacific with a maximum value at  $120^{\circ}\text{W}$ ,  $10^{\circ}\text{S}$ . The maximum cooling related to the vertical upwelling process lies in the

equatorial eastern Pacific and along the coasts of North and South America.

### 3.3.2 Experiment two: annual mean wind stress and annual cycle heat flux forcing

In the second experiment, I investigate the temporal evolution of sea surface temperature in response to the annual cycle of thermal forcing and annual mean of surface wind forcing.

Figure 25 shows the annual variation of simulated SST and external thermal forcing term (the  $Q$  term in the thermodynamic equation (3.2.5)) along the equator. The annual mean fields have been removed from the both fields. It is found that the anomalous warming (cooling) occurs in April (October) at  $100^{\circ}\text{W}$ . Such anomalous warming or cooling is associated with the annual variation of the thermal forcing in the eastern Pacific. The maximum positive (negative) anomaly in the thermal forcing field appears at  $90\text{-}100^{\circ}\text{W}$  in March (July and October). In the western-central Pacific, there is a semi-annual variation (a period of 6 months) in both the thermal forcing and SST fields. The annual variation is dominant in the eastern Pacific. Generally, the SST lags the ocean surface net heat flux by an approximate time scale of 1-2 months along the equator. Both the simulated SST and thermal forcing anomalies show little systematic westward propagation along the equator.

The above results suggest that the initial warming (or cooling) of the equatorial SST in the eastern Pacific is a response to thermal forcing of net surface heat flux. The response time scale is approximately 1-2 months. However, after it initiates the anomalous warming (or cooling) in the eastern Pacific, the surface heat flux does not cause the westward propagation of the SST anomaly.

Figure 26 shows the annual variation of the simulated SST and thermal forcing along 100-110°W. As in Figure 25, the annual mean fields have been removed. Both the SST and thermal forcing anomalies exhibit systematic northward propagation. For example, the maximum warm SST occurs at 25°S in March and propagates to the equator in April whereas the maximum thermal forcing anomaly appears at 30°S in January and propagates to the equator in March. The phase difference between the SST and thermal forcing anomalies is approximately 2 months at 30°S and 1 month at the equator.

The numerical results suggest that the annual variation of the surface heat fluxes plays an important role in determining the meridional propagation of the SST anomaly along the eastern Pacific. Further investigation reveals that solar radiation flux is a dominant term to cause the meridional propagation of the SST anomaly (figure not shown). Therefore, the initial anomalous warming (cooling) in the equatorial eastern Pacific may be due to the annual cycle of the solar radiation flux which propagates northward along the

eastern Pacific from the southern hemisphere to the northern hemisphere.

A interesting question related to the above phenomenon is why there is no southward propagation of the SST anomaly in the eastern Pacific while the sun goes back to the southern hemisphere. Due to unstable interaction between southerly wind and SST gradient, a number of low stratus clouds develop which greatly affect the solar heat flux at ocean surface (Mitchell and Wallace 1992). It is shown from the latitude-time profile of the downward surface solar flux (cloudiness effects included) (Esbensen and Kushnir 1981) that there is no southward propagation (Figure 27). Therefore, the low-stratus cloudiness feedback plays an important role in causing only northward propagation of the SST anomaly in the eastern Pacific.

### 3.3.3 Experiment three: annual cycle wind stress and annual mean heat flux forcing

In the third experiment, the response of the tropical Pacific SST to the annual cycle of wind forcing and annual mean of thermal forcing is examined.

Figure 28 shows the simulated SST and observed surface zonal and meridional wind fields along the equator (annual mean has been removed). Unlike in the previous experiment, the SST anomaly does show systematic westward propagation along the equator. Since there is no anomalous thermal forcing, the

westward propagation of the SST anomaly is purely due to the wind-related dynamical process. The observed zonal wind anomaly along the equator shows similar westward propagation. There is a phase difference between the SST and zonal wind anomalies. The westerly (easterly) anomaly lies west (east) of the anomalous warm SST. The observed meridional wind anomaly along the equator does not show significant phase propagation.

Zonal temperature advection and vertical upwelling are two major processes associated with the wind-induced dynamic process. The anomalous westerly wind west of the anomalous warm SST suppresses the upwelling by reducing the Ekman divergence and induces a positive zonal advection anomaly through mean negative SST gradients. In order to examine the relative importance of the two processes, the time-longitude profiles of the zonal and vertical temperature advection anomalies are illustrated in Figure 29. The systematic westward propagation of the SST anomaly is mainly due to the anomalous zonal temperature advection. The vertical temperature advection mainly contributes to the warming (or cooling) in the eastern Pacific (east of 120°W).

The amplitude of the SST anomaly due to the wind-induced dynamical process in the eastern Pacific (1.1°C) is almost same as that due to the anomalous thermal forcing (1.2°C). The maximum SST anomaly due to the anomalous wind forcing occurs in May while the anomaly due to the anomalous thermal forcing appears in April. This suggests the importance of surface heat

flux thermal forcing in the timing of initial warming or cooling in the equatorial eastern Pacific.

The simulated SST and observed surface wind anomalies do not show systematic meridional propagation in the eastern Pacific (Figure 30). The result suggests that the observed meridional propagation of the SST anomaly along the eastern Pacific, as shown in Figure 20b, is not due to the surface wind stress forcing.

#### 3.3.4 Experiment four: annual cycle wind stress and heat flux forcing

In the fourth experiment, the response of the tropical Pacific ocean to the annual cycles of surface wind and heat flux forcing is examined.

Figure 31 illustrates the simulated SST field along the equator and along 100-110°W. Both westward propagation of the SST anomaly along the equator and northward propagation along the eastern Pacific are simulated although the amplitude of the SST anomaly is smaller than the observed (see Figure 20). The SST anomaly in experiment 4 is approximately the sum of the previous two isolated experiments (Experiments 2 and 3). Along the equator, the simulated maximum anomalous warm (cold) SST occurs in April (August) at 90-100°W while the observed appears in March (September). The phase speed of westward propagation of the simulated SST anomaly is close to observation. Such westward propagation is due to the wind-

induced dynamic process and not due to the heat flux forcing. In the eastern Pacific around 100-110°W, the maximum SST anomaly (1.1°C) occurs in March along 20°S. It propagates northward and reaches to the equator in May. The meridional propagation of the SST anomaly results from the annual variation of surface heat fluxes.

#### 3.4 The remote and local wind forcing on the equatorial eastern Pacific SST

Climatological monthly mean surface wind over the equatorial western Pacific shows a clear annual variation. Both total and anomalous (to annual mean) zonal winds between 120°E and 170°E are westerlies during November and December (Figure 32). Maximum westerly anomaly occurs in November at 160°E with a magnitude of 2.2 m/s whereas the maximum westerly (2.5 m/s) of the total field appears in December at 140°E. Lukas (1981) suggested that the change of sign of pressure gradient associated with equatorial undercurrent at 86°W-96°W during early spring is caused by the remote wind forcing in the west side of the ocean through the propagation of an oceanic Kelvin pulse since the phases of local wind stress lag the pressure gradient change by 1-2 months. Wang (1992b) implied that the change in SST off the coast of Ecuador (80-86°W, 2°N-2°S) is a remote response to the annual variation of the zonal wind in the western Pacific since it leads by about two months (his Fig. 12c).

In this section, using the ocean model described in 3.2, I attempt to investigate the response of the equatorial eastern Pacific SST to remote and local surface wind forcing. Two experiments are designed. In the first experiment, I specify the annual cycle of surface wind forcing in the western Pacific (west of the date line) but keep the annual mean wind forcing in the rest ocean. In the second experiment, the annual cycle of wind forcing in the eastern Pacific (east of 120°W) and the annual mean of wind forcing at west of 120°W are specified. In both experiments, observed annual mean surface heat fluxes are applied.

#### 3.4.1 The remote forcing

In the first experiment, the response of the equatorial eastern Pacific SST to anomalous wind forcing west of the date line is examined. There is no anomalous wind forcing east of 180°E. Figure 33 shows the simulated anomalous SST field along the equator. A maximum positive SST anomaly occur in January in the eastern Pacific around 110°W. The amplitude of the anomaly is 0.23°C. Another positive SST anomaly appears in December around 170°E with an amplitude of 0.16°C. The positive SST anomaly propagates eastward along the equator with an approximate phase speed of 75° longitude per month (about 3 m/s). This speed is the same as that of oceanic Kelvin waves. The eastward propagation of the anomalous SST signal coincides well with the thermocline depth anomaly field

(Figure 34). The time evolution of the SST anomaly in the eastern Pacific is highly asymmetric between transition periods from maximum warm to cold SST anomalies (3 months from January to April) and from maximum cold to warm SST anomalies (9 months from April to January). The thermocline depth anomaly shows a similar feature. Due to anomalous westerly (easterly) forcing in the western Pacific, downwelling (upwelling) oceanic Kelvin waves are excited which propagate eastward along the equator away from the forcing region. For example, a positive thermocline depth anomaly, which represents a downwelling Kelvin pulse, occurs at  $170^{\circ}\text{E}$  in November when the maximum westerly anomaly appears. The thermocline depth anomaly propagates eastward and approaches  $160^{\circ}\text{W}$  in December and  $110^{\circ}\text{W}$  in January. Such eastward propagation results from oceanic free Kelvin wave dynamics and is extremely different from the westward propagation of the SST anomalies due to the coupled air-sea interaction mechanism.

To further identify the horizontal structure of the eastward-propagating free Kelvin wave, Figure 35 illustrates the simulated anomalous thermocline depth field. It clearly shows the Kelvin wave structure with the maximum amplitude in the equator. Since there is no anomalous forcing east of  $180^{\circ}\text{E}$ , the thermocline depth anomaly east of the date line is due to remote forcing of anomalous winds in the western Pacific. After it approaches the eastern boundary, the Kelvin

wave propagates poleward along the coasts of North and South America.

Of particular interest in contrast to this experiment is the examination of the response of the SST to the annual cycle of wind forcing east of the date line with a specified annual mean wind field west of  $180^{\circ}\text{E}$ . Different from the eastward propagation of free oceanic Kelvin waves, the SST anomaly shows westward propagation in response to surface wind forcing in the central and eastern Pacific (Figure 36). When the annual cycle of surface wind forcing is applied in all Pacific region, the two waves, the eastward-propagating free Kelvin wave and the westward-propagating forced wave, will interfere. For example, an anomalous cooling ( $-0.23^{\circ}\text{C}$ ) occurs in April in the eastern Pacific due to the free Kelvin wave (Figure 33) while an anomalous warming of  $1.2^{\circ}\text{C}$  occurs at same time and place due to the forced wave (Figure 36). The net effect of the two waves is a SST anomaly of  $1.0^{\circ}\text{C}$  in April (Fig. 28). Although the amplitude of the SST anomaly in the eastern Pacific due to remote forcing of the anomalous wind in the western Pacific is quite small compared with that due to local wind forcing, the remote forcing may play a role in the initiation of the anomalous warming or cooling in the equatorial eastern Pacific.

#### 3.4.2 The local forcing

In this experiment, the response of the eastern Pacific SST to the local (120°W-80°W) anomalous wind forcing is examined.

In response to the anomalous local wind forcing, SST anomalies are confined in the eastern Pacific (east of 120°W) while thermocline depth anomalies are found farther to the west (Figure 37). A maximum SST anomaly occurs in the equatorial eastern Pacific around 100°-110°W. The anomalous warming starts from February, reaches its peak in March, and disappears in July-August. The maximum cold SST anomaly in the eastern Pacific appears in November. The amplitude of both the anomalous warming and cooling in the equatorial eastern Pacific due to local wind forcing is about 1°C.

The thermocline depth anomaly field shows more obvious westward propagation than the anomalous SST field. For example, a negative thermocline depth anomaly occurs in April at 130°W and propagates westward along the equator to 140°E in August. The phase speed of the negative anomaly is about 22.5° longitude per month (about 1 m/s). Since there is no anomalous wind forcing west of 120°W, the westward propagation is regarded as a free oceanic Rossby wave. This is confirmed from the horizontal structure of the anomalous thermocline depth field (figure omitted) in which there is dominant symmetric structure with a lowest meridional mode, resembling Rossby wave structure.

### 3.5 The effect of annual variation of cloudiness on the SST change

In previous sections, surface heat fluxes are specified from climatological monthly mean fields (Esbensen and Kushnir 1981). For a coupled ocean-atmosphere system, solar radiation at the top of the earth atmosphere is the sole external input. The coupling between ocean and atmosphere is strongly influenced by atmospheric parameters such as clouds, wind speed, air surface temperature and specific humidity.

In this section, annual mean and annual cycle of the tropical Pacific SST are simulated using empirical heat flux parameterization formulae. Only surface wind and cloud cover are specified as external parameters. Air surface temperature and specific humidity are determined from SST through empirical regression equations derived from climatological monthly mean fields (Esbensen and Kushnir 1981).

#### 3.5.1 Surface heat flux parameterization

The net downward heat flux at ocean surface can be expressed as

$$Q_{\text{net}} = \text{SR} - \text{LW} - \text{LH} - \text{SH} \quad (3.5.1)$$

where SR represents downward solar radiation at ocean surface, LW net upward longwave radiation flux, LH latent heat flux, and SH sensible heat flux.

Philander et al. (1987) in their study of seasonal cycle using an OGCM model assumed a constant solar radiation flux equatorward of 20° latitude and a constant longwave radiation flux and used standard bulk formulae to compute latent and sensible heat fluxes. They also assumed a constant relative humidity (80%) with a specified observed air surface temperature field. Seager et al. (1988) in a simple model of the tropical Pacific SST used Weare et al.'s (1980) formula to compute the solar radiation flux by giving climatological cloud cover fields. The longwave radiation and sensible heat flux were simply parameterized as a Newtonian cooling term by forcing the model SST towards a constant temperature with an upward heat flux in the range of 30-45 Wm<sup>2</sup>.

In the present study, following Esbensen and Kushnir (1981), the solar radiation flux at the ocean surface is computed according to Berliand's formula (Budyko 1974). It consists of two parts: an estimate of the monthly averaged maximum available direct plus diffuse solar flux at sea level, which is a function of latitude and month, and a factor which includes the effect of cloudiness, i.e.,

$$SR = Q_0(1-A)[1 - (a_1+a_2n)n] \quad (3.5.2)$$

where  $Q_0$  is the monthly averaged direct and diffuse maximum solar flux calculated from observation by Budyko (1974, Table 3),  $A$  is surface albedo which is taken to be 0.06, a typical

value for the tropical oceans (Payne 1972),  $n$  is the monthly averaged cloudiness, and coefficients  $a_1$  and  $a_2$  are given in Budyko's book (Table 4).

The net upward long-wave radiation flux is parameterized as

$$LW = \varepsilon\sigma T_a^4(0.39-0.05e^{0.5})(1-a_3n^2) + 4\varepsilon\sigma T_a^3(T_s-T_a) \quad (3.5.3)$$

where  $T_a$  and  $T_s$  are the monthly mean air and sea surface temperatures,  $e$  is the monthly averaged water vapor pressure (in mb),  $\varepsilon$  is the emissivity of water ( $=0.97$ ),  $\sigma$  is the Stefan-Boltzmann constant,  $a_3$  is a coefficient depending on latitude in order to account for the varying radiative properties of clouds at different latitudes (Budyko, 1974, Table 9).

The latent and sensible heat flux estimates are based on the bulk aerodynamic formulae, i.e.,

$$LH = \rho_a L C_D V_a (q_s - q_a) \quad (3.5.4)$$

and

$$SH = \rho_a C_p C_D V_a (T_s - T_a) \quad (3.5.5)$$

where  $\rho_a$  is the density of air,  $C_p$  the isobaric specific heat of air,  $L$  the latent heat of evaporation,  $C_D$  the drag

coefficient, and  $q_s$  and  $q_a$  the monthly averaged sea and air specific humidities.

To apply the aforementioned surface heat flux formulas, one has to specify atmospheric variables such as surface wind, cloudiness, air surface temperature and humidity. According to a statistical analysis, there are high (greater than 0.9) correlations between  $T_s$  and  $q_s$  (see empirical relationship, Eq. (2.3.6) in Chapter 2) and between  $T_s$  and  $T_a$  (the linear regression equation is  $T_a = 1.03T_s - 1.32$ ). The climatological monthly mean data of Esbensen and Kushnir (1981) in the domain of 120°E-80°W and 30°S-30°N for all 12 months are used for the above regression analysis (sample size: 33x16x12). Therefore, air surface temperature and specific humidity can be empirically determined from the model SST, and only surface winds and cloudiness are specified.

### 3.5.2 The results

In this section, annual mean and annual cycle of SST are simulated using the aforementioned parameterization formulas of solar radiation, longwave radiation, latent and sensible heat fluxes described in Section 3.5.1. In the annual mean SST simulation (Figure 38a), climatological annual mean surface wind (Sadler et al. 1987), cloudiness (Esbensen and Kushnir 1981), and direct plus diffuse solar flux (Budyko 1974) are specified. The western Pacific warm pool and eastern Pacific cold tongue are simulated. It is noted from Figure 38b that

the difference between the simulated and observed SST is less than 1°C in most region. The largest error (-3.8°C) appears in the artificial eastern boundary along 82°W due to strong coastal upwelling there while the realistic coast of the South America lies a few degrees to the east.

The effect of annual variations of cloudiness is examined by analyzing the following two experiments in annual cycle SST simulations. In one experiment, annual mean cloudiness is fixed. In the second experiment, annual cycle of cloudiness is specified. Figure 39 shows the simulated SST fields in the second experiment for two extreme months in terms of the SST cold tongue: March and September. In the western Pacific, the warm pool lies along the southern Pacific convergence zone in March and moves northwestward to the north western Pacific in September. In the eastern Pacific, the equatorial cold tongue is much stronger in September than in March. Along the south America coast, the SST is 4°C colder than that in March. Along the intertropical convergence zone, the SST shows strong phase in September characterized by a 27°C SST zone whereas it is only 26°C contour line in March.

The difference of the simulated SST fields between the two experiments (as shown in Fig. 40) indicates that due to the absence of description of annual cycles of cloudiness, the simulated SST is overestimated in summer/fall hemisphere and underestimated in winter/spring hemisphere. The largest difference (about 0.9°C) occurs in the northeastern Pacific

monsoon region. The difference in the other region is less than  $0.4^{\circ}\text{C}$ . Compared with the amplitude of annual variation of SST, the difference in the eastern Pacific subtropical high region is small. However, it is relatively large in the western Pacific. The result suggests that the annual variation of cloudiness is important for simulating a realistic annual cycle of SST in the western Pacific and the northeastern Pacific monsoon region and is not important in the rest of the ocean.

## CHAPTER FOUR

### SUMMARY

In this study, I investigate the physical mechanisms of the annual cycle in the tropical Pacific atmosphere and ocean.

A simple atmospheric model is proposed for studying the key parameters of the coupled ocean-atmosphere system, monthly mean surface winds and precipitation, for a given sea surface temperature forcing. The model atmosphere is assumed to be in a hydrostatic equilibrium with a linear lapse rate in the troposphere. A vertically integrated hydrostatic equation is derived to directly determine the sea-level pressure field from SST. Since the annual variation of the mean lapse rate is highly correlated with that of SST, it is empirically determined from the monthly mean SST field. The determination, however, contains a systematic bias. The bias is basically independent of season. It is important in accounting for the east-west phase difference between cold SST tongues and subtropical high pressure systems even though its magnitude is moderate. So far all simple models fail to reproduce accurately such a phase difference so that the simulated easterly trades in the eastern Pacific Ocean and along-shore meridional winds near Mexico and South America are weaker than those observed. The exact physical mechanisms causing such a phase difference remain unanswered in this stage. I speculate that the effects of the upper-troposphere circulations and

radiation transfer as well as transient processes may be possible causes.

The empirical relationship between the vertically averaged lapse rate and SST implies that from a statistical sense, there is a climatological advection/adiabatic/radiation thermodynamic equilibrium in the tropical troposphere. Thermodynamics in the Gill model involves the feedback of low-level convergence through adiabatic processes and a variety of atmospheric heating. Compared with it, the present model has a much simpler formulation. Only hydrostatic equation and the equation of state are applied in determining an important thermodynamic quantity, sea-level pressure. Success in modeling a realistic annual cycle of sea-level pressure implies that the tropical atmosphere is in a climatological advection/adiabatic/radiation equilibrium so that complicated thermodynamic processes can be parameterized in terms of underlying SST.

The diagnosis of linear three-force balance in the Gill model indicates that the use of direction- and latitude-dependent Rayleigh friction coefficients is crucial for surface momentum balance and can significantly reduce surface wind errors. The diagnosis of thermodynamic problems in a simple atmospheric model shows that the difficulty in producing a realistic SLP field lies in the proper description of spatial and temporal variations of vertically averaged lapse rates.

The response of the tropical atmosphere to the symmetric and antisymmetric SST forcing is examined using the proposed simple atmosphere model. It is found that the time evolution of the symmetric SST mode results in the westward phase propagation of the surface zonal wind, precipitation and sea-level pressure along the equator. It is also found that the annual variation of the antisymmetric SST mode causes the seasonal oscillations in the precipitation field with maximum rainfall along the climatological convergence zones such as the ITCZ and SPCZ, in the sea-level pressure field with large amplitudes in the subtropical region away from the equator, and in the monsoonal circulations with the anomalous westerly in the summer hemisphere and the cross-equatorial flows directed from the winter hemisphere.

The model is extremely cheap in computational costs. Despite its simplicity, it is capable of simulating realistic annual cycles of the surface wind, sea-level pressure, and precipitation over the tropical Pacific. It can also be used to study the interannual variability associated with El Nino/Southern Oscillation (Li and Wang 1992). The results suggest that the physics of the tropical atmospheric response to external SST forcing can be understood in terms of the proposed conceptual dynamic and thermodynamic framework.

A reduced-gravity ocean model is used to study the response of the tropical Pacific SST to the surface wind stress and heat flux thermal forcing. The model contains

linear dynamics in the upper ocean that predict mean currents and thermocline depth and a nonlinear thermodynamic equation to predict sea surface temperature. A constant buoyancy is assumed in the upper ocean so that the model dynamic quantities such as horizontal currents and thermocline depth are independent of SST and depend only on surface wind stresses. Following Cane (1979), Zebiak and Cane (1987), and Seager et al. (1988), a constant depth, frictional, linear surface layer is added to the upper ocean so that vertical entrainment rate is dynamically determined from wind-induced upwelling through Ekman divergence at the surface layer. The temperature of entrained water below the surface layer is assumed to be observed climatological annual mean temperature at base of the layer plus a perturbation which is parameterized by annual variation of simulated thermocline depth fields.

With specified surface wind and heat flux forcing, the ocean model is able to capture many fundamental features of climatological SST in the tropical Pacific. For instance, the western Pacific warm pool and the eastern Pacific cold tongue are simulated and there are clear annual variations in the SST field.

The mechanisms for annual cycles of the tropical Pacific SST are investigated using the ocean model. Physically, there are two important processes which affect the SST. One is wind-related dynamic processes that include horizontal advection

and vertical upwelling. Another is thermal forcing which consists of solar radiation, longwave radiation, latent heat and sensible heat fluxes. By examining the response of the SST to the annual mean or annual cycle of surface wind and thermal forcing, I find that the westward propagation of the equatorial SST results from the wind-induced dynamic processes and the northward propagation of the anomalous SST in the eastern Pacific is due to the annual variation of solar radiation forcing.

From a meteorological view, the westward propagation of atmospheric quantities such as surface zonal wind, SLP, and precipitation along the equator is due to westward propagating symmetric SST forcing. From an oceanographic view, the westward propagation of equatorial SST is due to wind-related dynamic processes. Therefore, the westward phase propagation of the atmospheric and oceanic components along the equator is a manifestation of air-sea interaction.

Although coupled air-sea interaction is an important mechanism to cause the westward propagation of the equatorial SST anomaly in the Pacific, the initiation of anomalous warming (or cooling) in the eastern Pacific is primarily due to the northward propagation of the SST anomaly in response to solar radiation forcing. The remote forcing of anomalous westerly (or easterly) winds in the equatorial western Pacific also has contribution on the eastern Pacific SST variation by exciting ocean Kelvin waves which propagate eastward.

The parameterization of solar radiation, longwave radiation, latent heat and sensible heat fluxes has been carried out to examine the effects of annual variations of cloudiness on the SST change. The solar and longwave radiation fluxes follows Berliand's formulas and the latent and sensible heat fluxes use empirical bulk formulations. Only winds and cloud cover are required as external inputs. Other parameters such as air surface temperature and specific humidity are determined from SST through empirical relationships derived from climatological monthly mean data. By avoiding the specification of the parameters, one obtains two advantages. First, the model can be coupled to a simple atmosphere model which does not predict these variables, and second, the model is not sensitive to the expected errors in the determination of these variables from a more complex atmosphere GCM.

Runs using specified annual mean and annual cycle of cloudiness indicate that the annual mean cloud cover has a primary effect on the SST field and the seasonal variation of cloud cover is obviously of secondary importance. The difference of SST in the two experiments is generally less than  $0.4^{\circ}\text{C}$ . However, the difference is important in the western Pacific since it has a comparable magnitude as that of annual or interannual SST variation there. The results suggest that the effect of annual variation of cloudiness on the SST is crucial in the western Pacific and in the northeastern Pacific and is not important elsewhere in the Pacific.

The major discrepancy in the ocean model is failure to produce the realistic strength of annual variations of the SST in the equatorial eastern Pacific. For example, the observed SST anomaly in the eastern Pacific around 100°W is 2.8°C while the simulated is 2.0°C. Furthermore, the observed maximum SST anomaly in the equatorial eastern Pacific occurs in March while the simulated appears in April. The assumptions of constant mixed layer depth and the empirical entrainment temperature formulation are possible causes. Within the model framework, a number of modifications can be made. For example, both mixed-layer and thermocline depths can change with time and space by formulating a simple two and one-half layer model similar to that of Schopf and Cane (1983), and the mixed layer physics such as turbulence mixing can be combined with model dynamics in order to better describe the vertical entrainment process.

In this dissertation study, I have analyzed and simulated the annual cycles of the tropical Pacific atmosphere and ocean using a simple atmosphere model and a reduced-gravity ocean model. Future work will focus on the study of the mechanisms of low-frequency variabilities in a coupled air-sea-interaction system and the simulation of the intraseasonal oscillation, annual cycle, and interannual oscillation in the tropical Pacific atmosphere and ocean.

APPENDIX

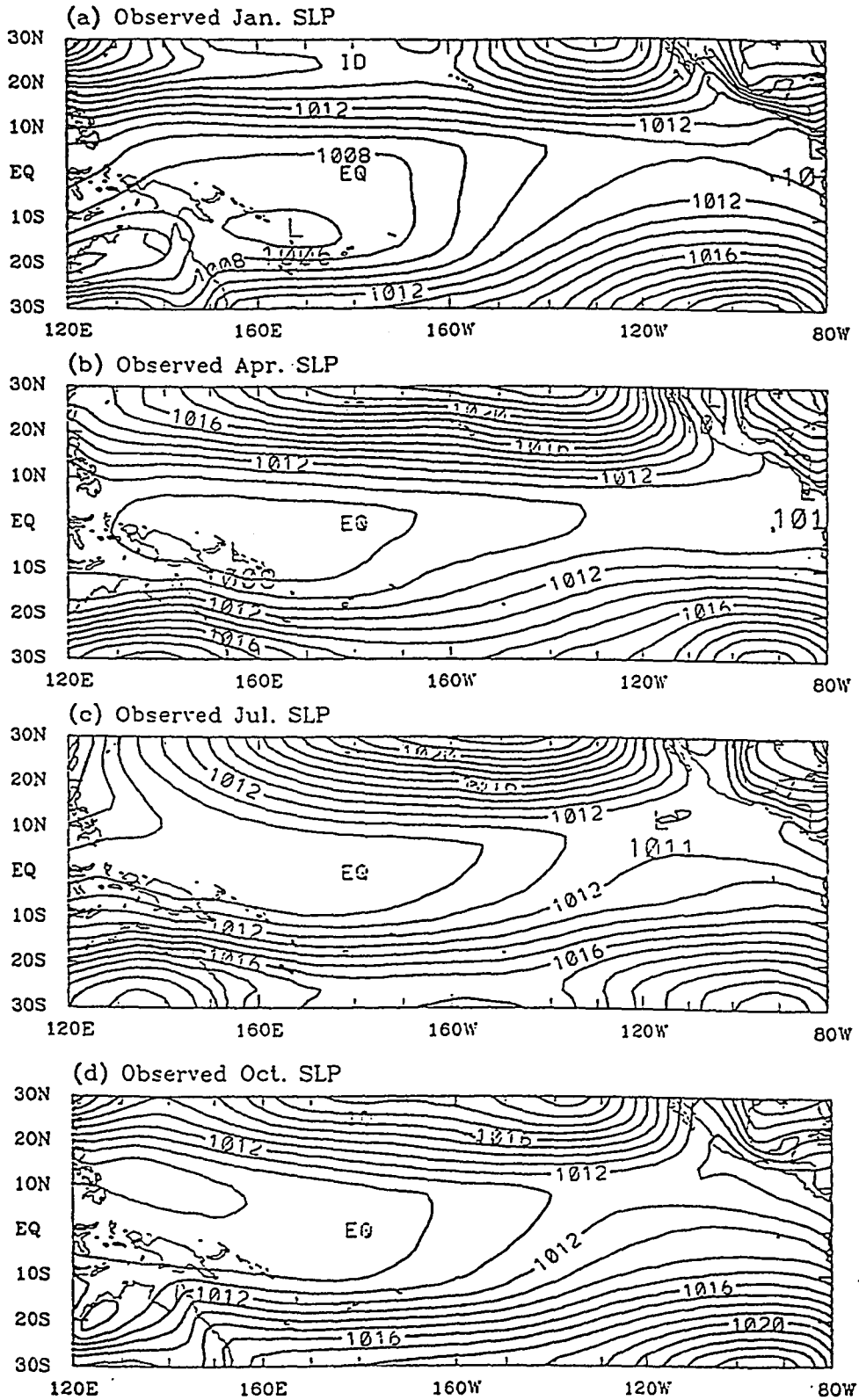


Fig. 1a Observed climatological monthly mean sea-level pressure (mb) field derived by Sadler et al. (1987) in January, April, July, and October, respectively. Contour interval is 1 mb.

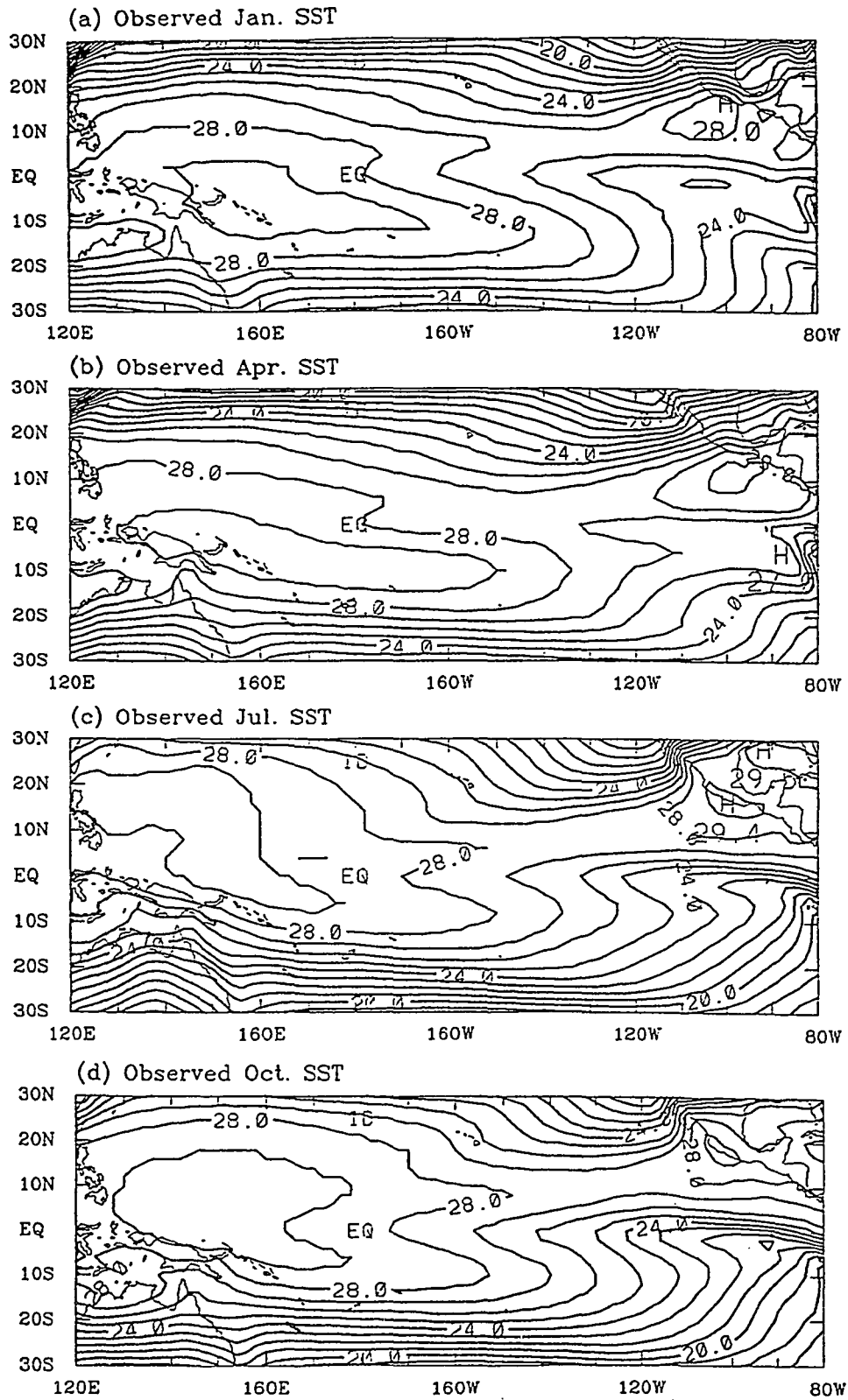


Fig. 1b

Observed climatological monthly mean sea surface temperature field derived by Sadler et al. (1987) in January, April, July, and October, respectively. Contour interval is 1°C.

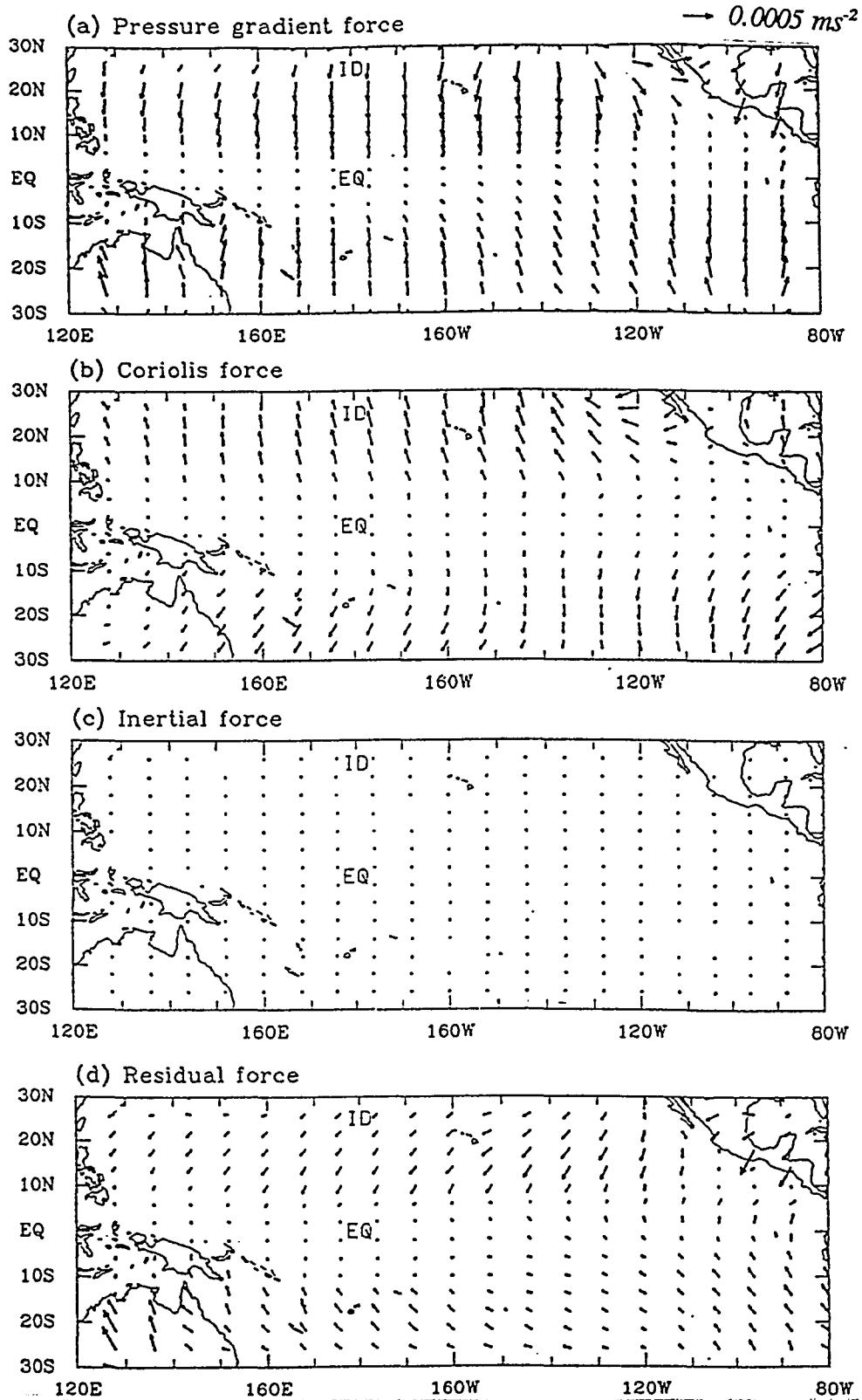


Fig. 2 The pressure gradient force (a), Coriolis force (b), inertial force (c), and residual force (d) computed from climatological annual mean sea-level pressure and surface winds derived from COADS by Sadler et al. (1987). The unit vector is  $5 \times 10^{-4} \text{ ms}^{-2}$ .

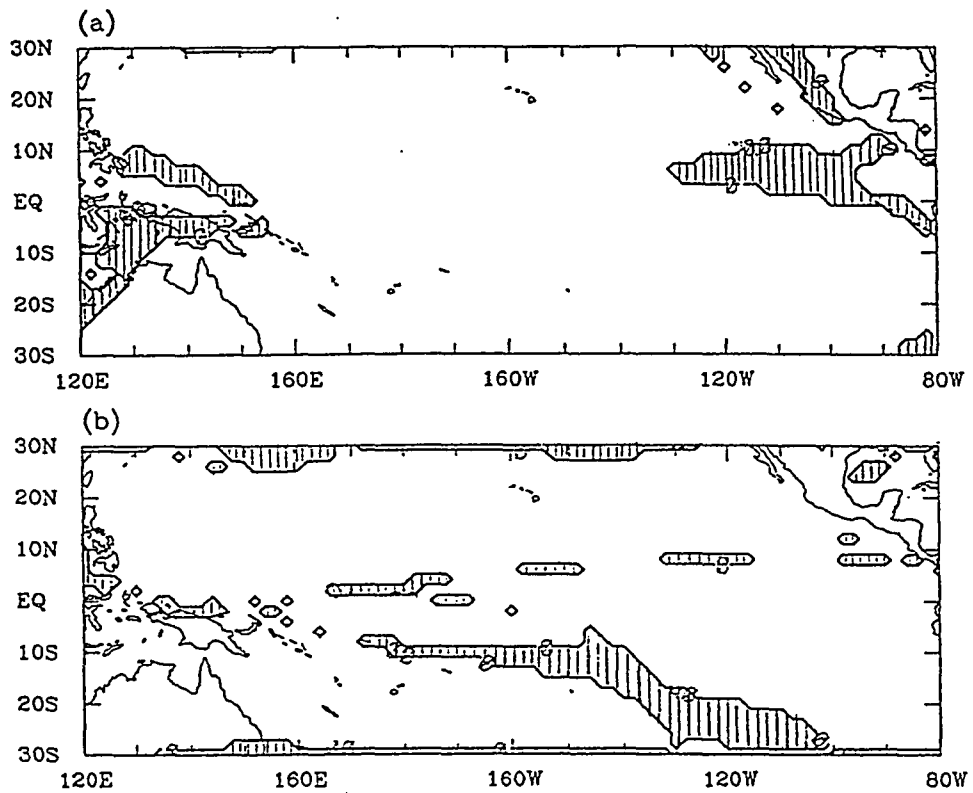


Fig. 3 Geographic distribution of the regions (represented by shaded areas) where opposite signs exist between the zonal residual force ( $R_1$ ) and zonal wind component (a) and between the meridional residual force ( $R_2$ ) and meridional wind component (b).

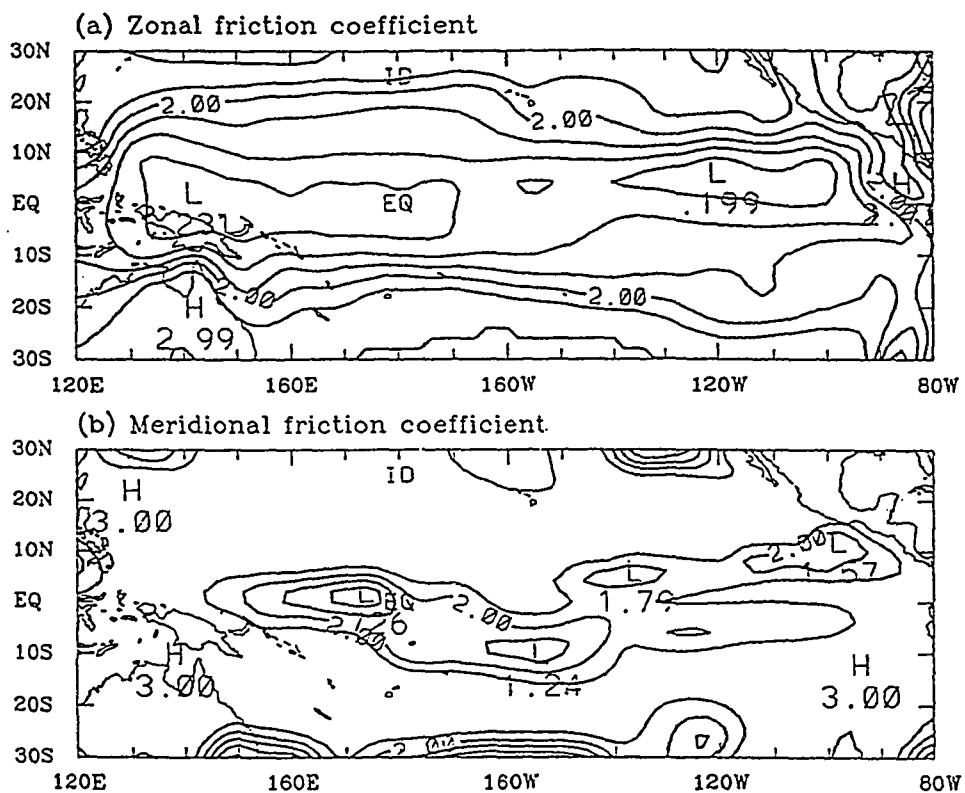


Fig. 4 Diagnosed annual mean zonal (a) and meridional (b) friction coefficients (in units  $10^{-5} \text{ s}^{-1}$ ) based on observation. Contour interval is  $0.5 \times 10^{-5} \text{ s}^{-1}$ .

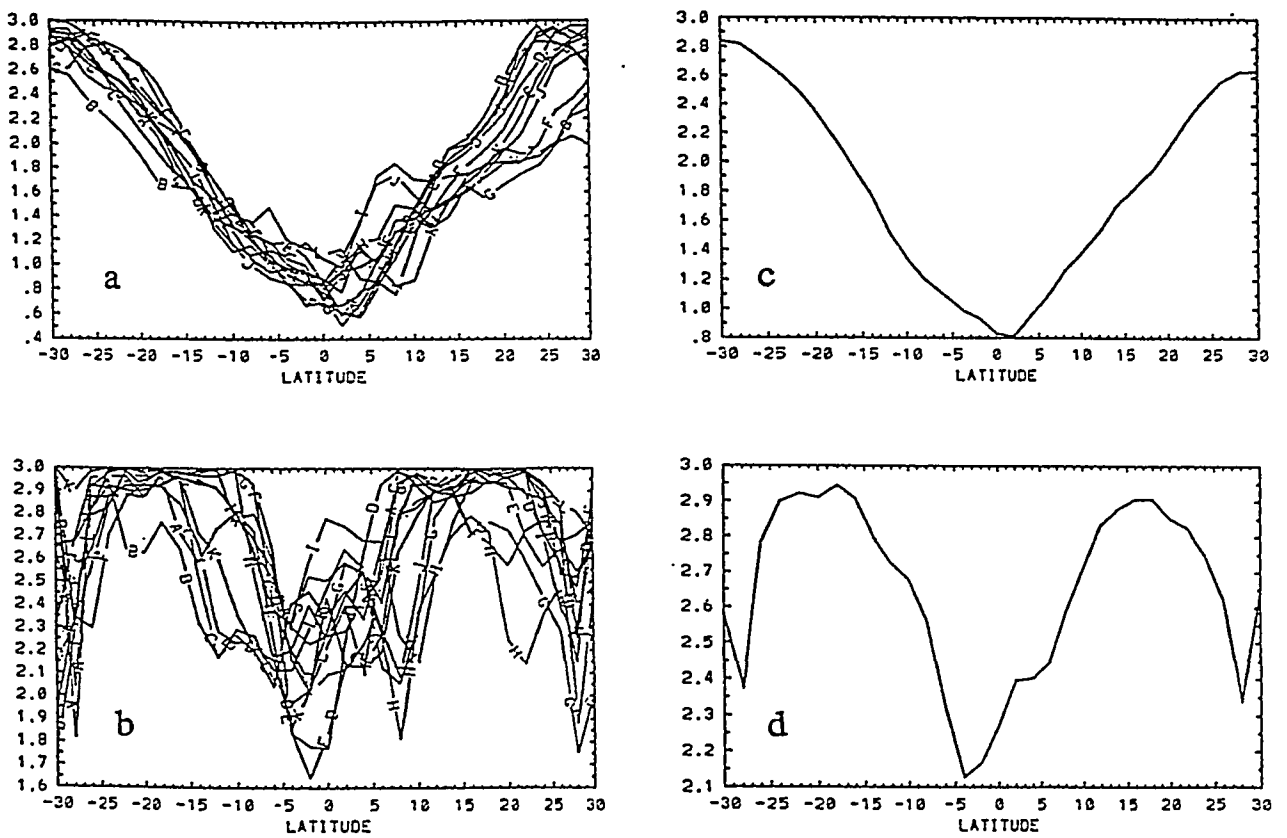


Fig. 5 The meridional distribution of zonal-averaged zonal (a) and meridional (b) friction coefficients from January (line A) through December (line L), and 12-month-mean zonal (c) and meridional (d) coefficients in units  $10^{-5} \text{ s}^{-1}$ .

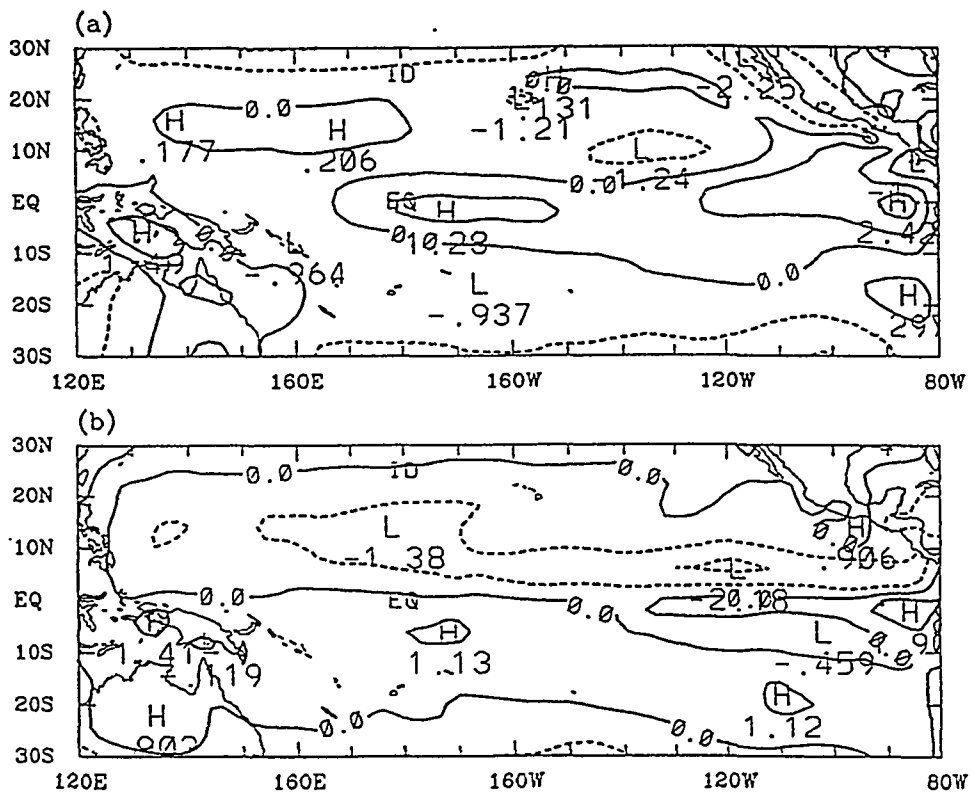


Fig. 6 The difference between simulated and observed annual mean surface zonal (a) and meridional (b) winds (in units m/s). The simulation uses a linear three-force balance model (2.2.2) with the direction- and latitude-dependent Rayleigh friction coefficients. Contour interval is 1 m/s.

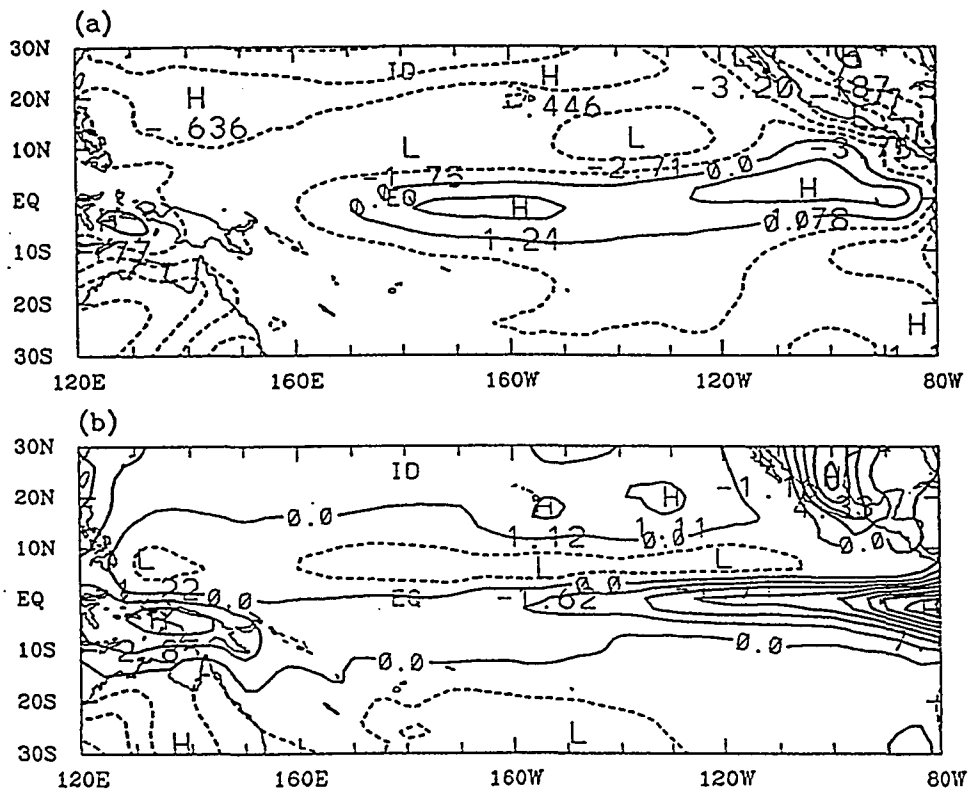


Fig. 7 As in Fig. 6 except with a constant Rayleigh friction coefficient of  $10^{-5} \text{ s}^{-1}$ . Contour interval is 1 m/s.

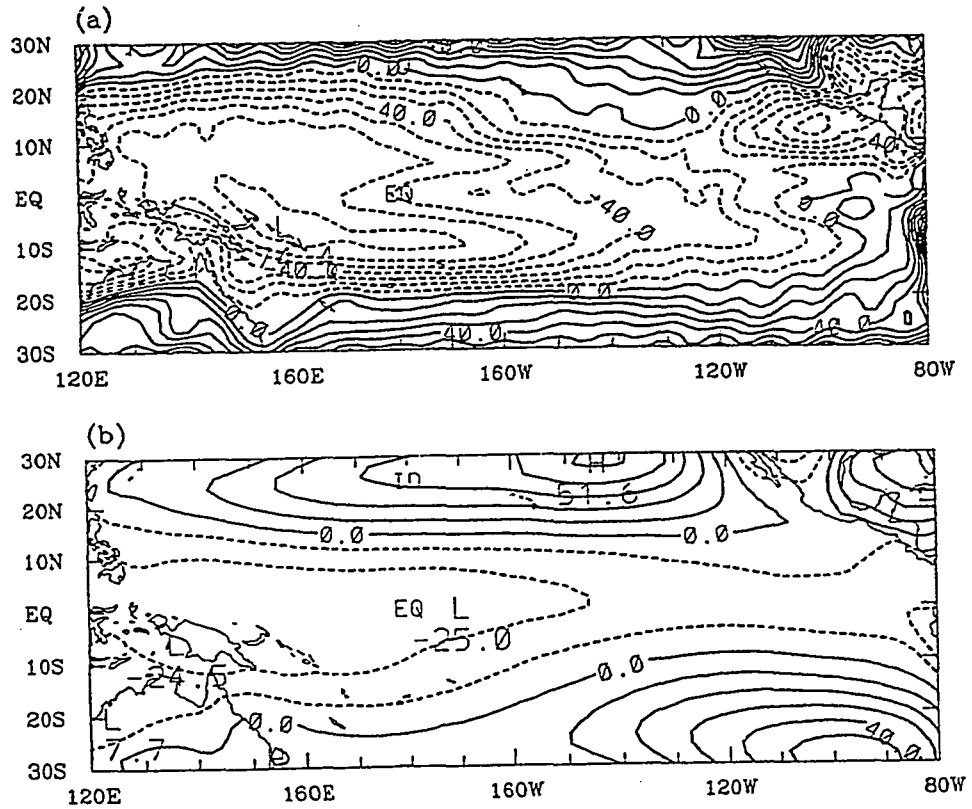


Fig. 8 (a) The diagnosed annual mean lower-troposphere geopotential height perturbation (in units m) based on the thermodynamic equation (2.2.3) in the WL model, using climatological annual mean SST and surface and 850mb winds. (b) The annual mean 850mb geopotential height perturbation (in units m) computed from climatological annual mean sea-level pressure with an approximate temperature profile proposed by Lindzen and Nigam (1987). Contour interval is 10 m.

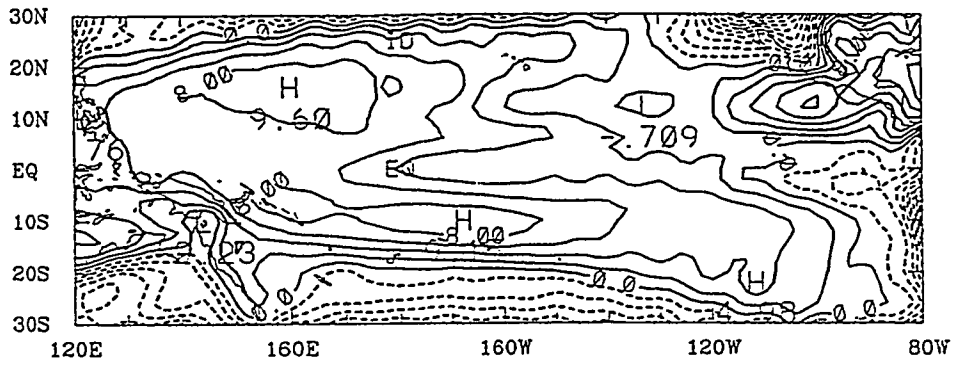


Fig. 9 The annual mean perturbation lapse rate (in units of  $10^{-5} \text{ }^{\circ}\text{C/Pa}$ ) diagnosed from the thermodynamic equation (2.2.3) using climatological annual mean SST, 850mb and surface winds, and 850mb geopotential height. Contour interval is  $2 \times 10^{-5} \text{ }^{\circ}\text{C/Pa}$ .

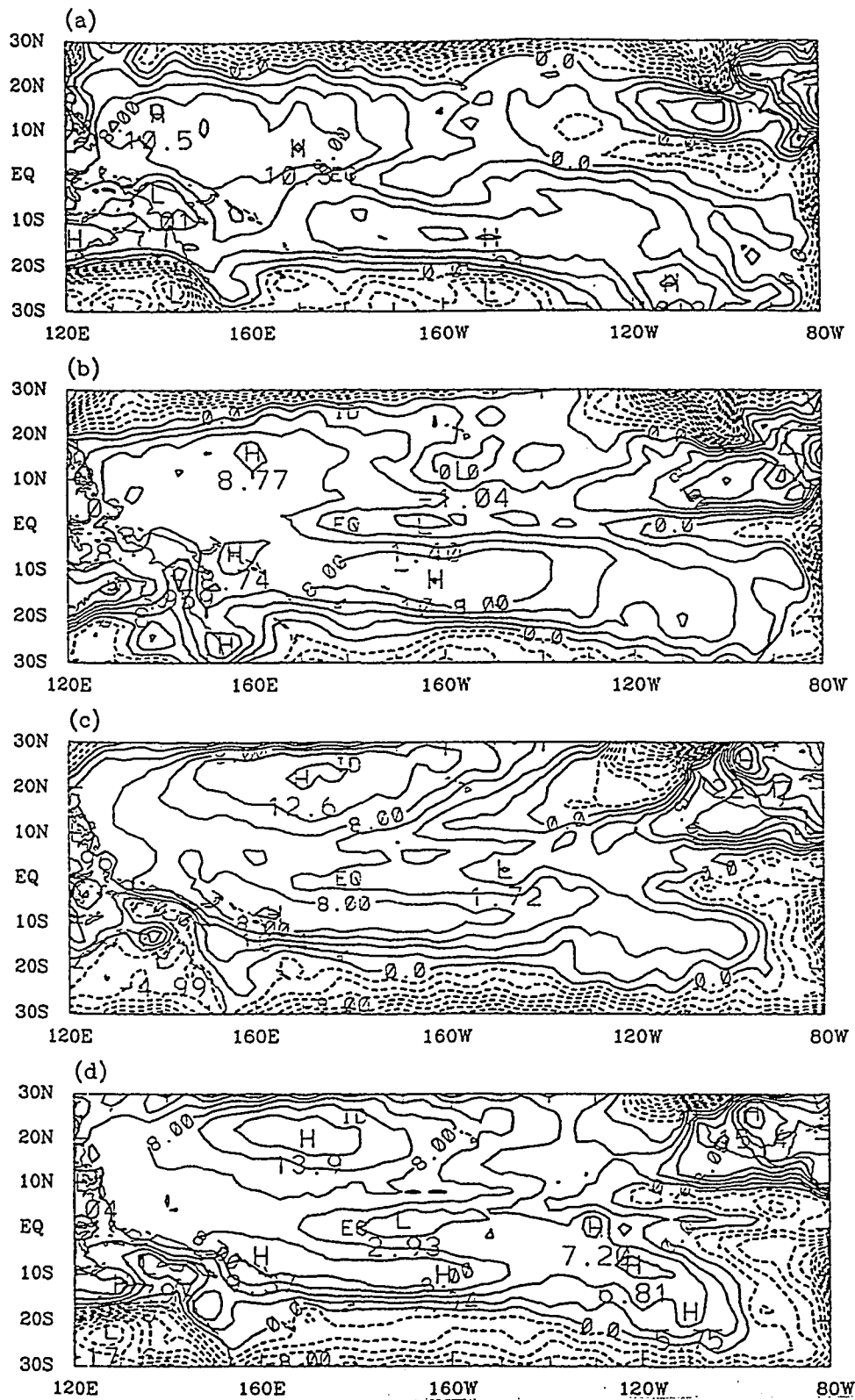


Fig. 10 The diagnosed January, April, July and October perturbation lapse rates (in units  $10^{-5} \text{ }^{\circ}\text{C}/\text{Pa}$ ) calculated from the corresponding climatological monthly mean SST, surface and 850mb winds, and 850mb geopotential height. Contour interval is  $2 \times 10^{-5} \text{ }^{\circ}\text{C}/\text{Pa}$ .

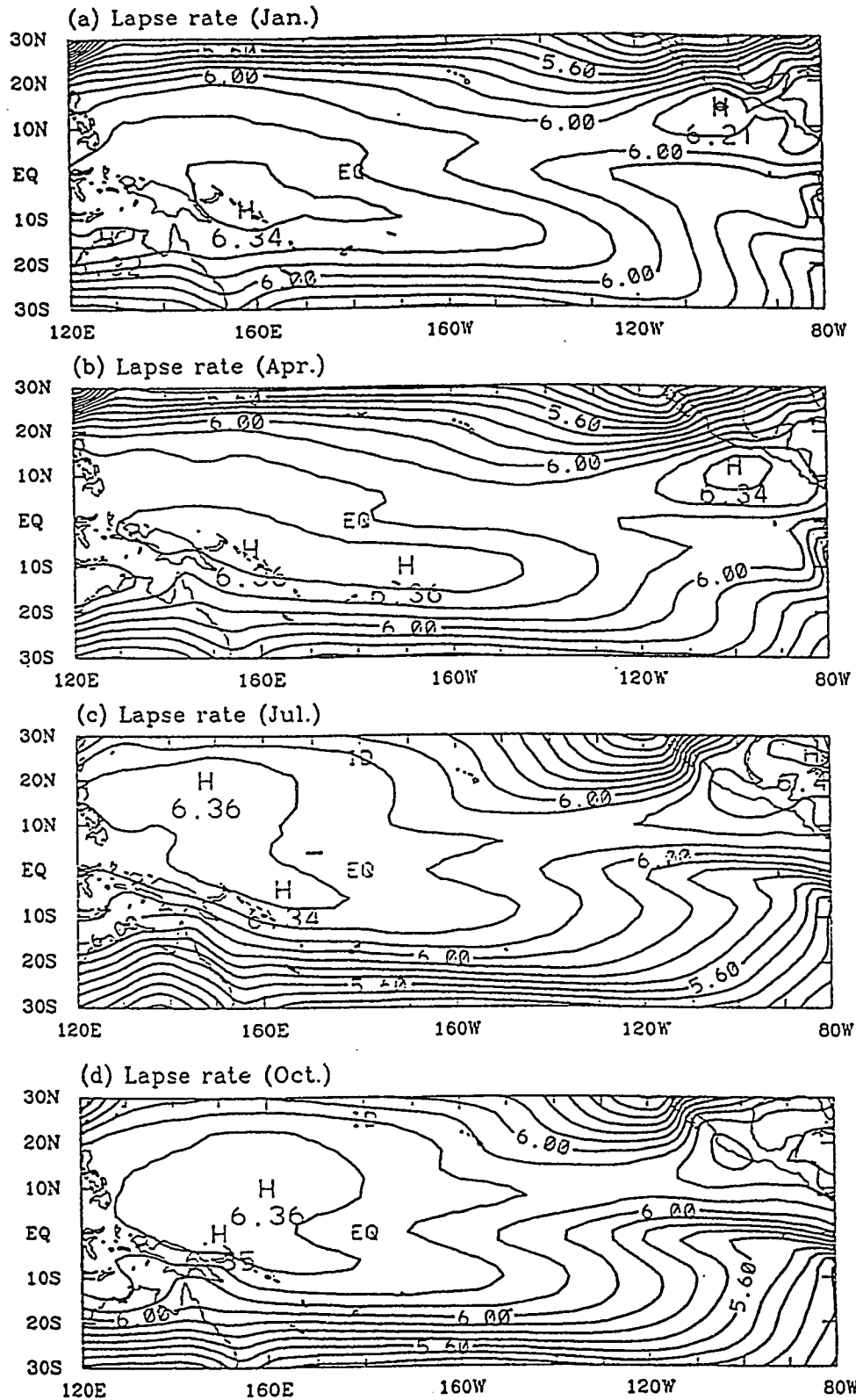


Fig. 11 The diagnosed January, April, July and October lapse rate (in units  $^{\circ}\text{C}/\text{km}$ ) distribution calculated from equation (2.3.2) by using observed climatological monthly mean SST and SLP (COADS) data. Contour interval is  $0.1\text{ }^{\circ}\text{C}/\text{km}$ .

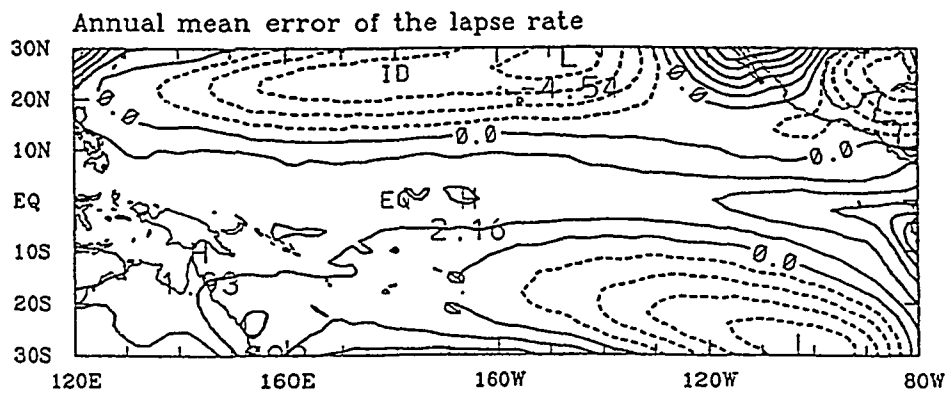


Fig. 12 The 12-month-mean difference between the empirical lapse rate calculated from Equation (2.3.3) and the diagnosed lapse rate calculated from Equation (2.3.2). Contour interval is 0.01 °C/km.

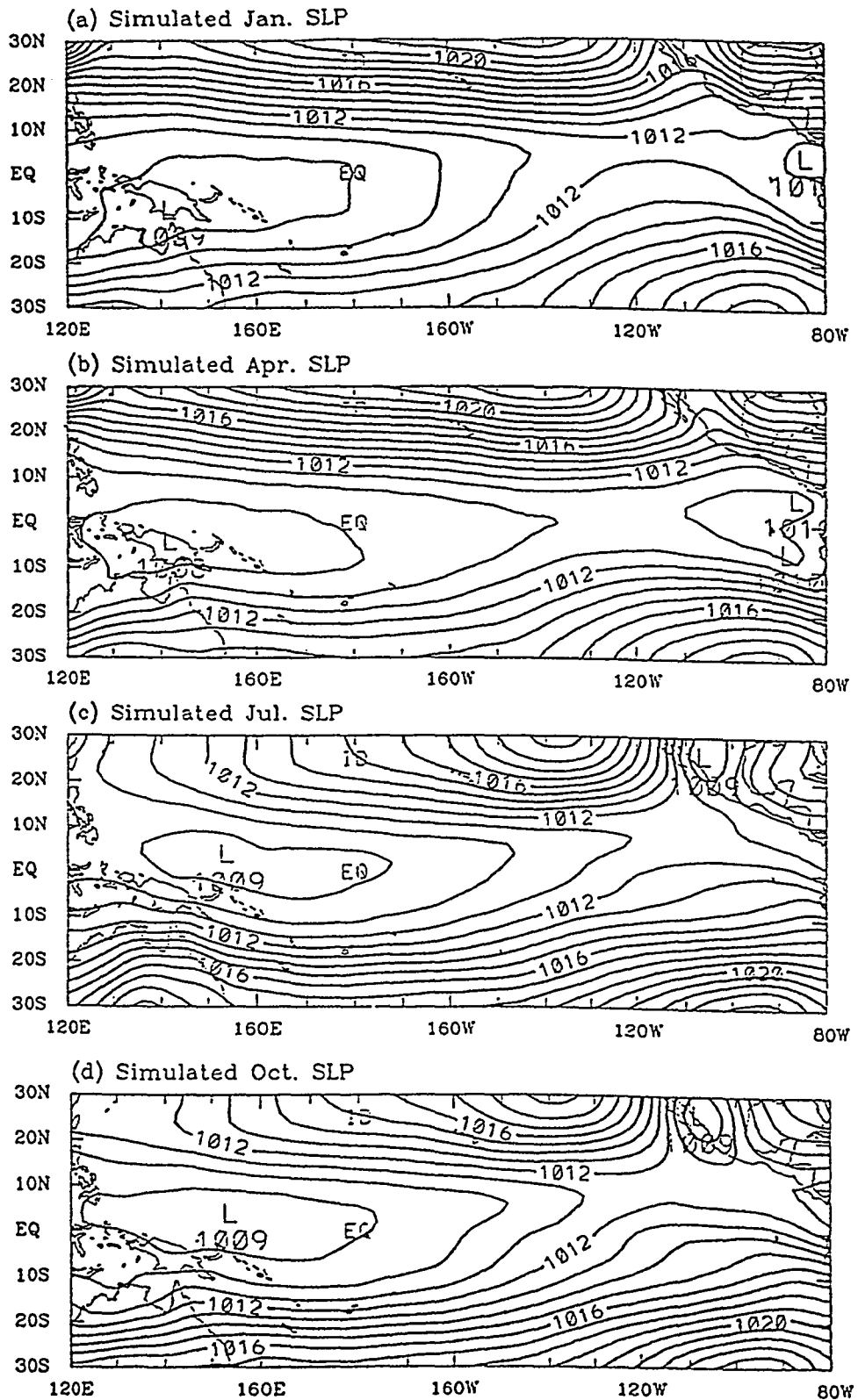


Fig. 13

The simulated (a) January, (b) April, (c) July, and (d) October sea-level pressure (in units mb) fields using the present model. Contour interval is 1 mb.

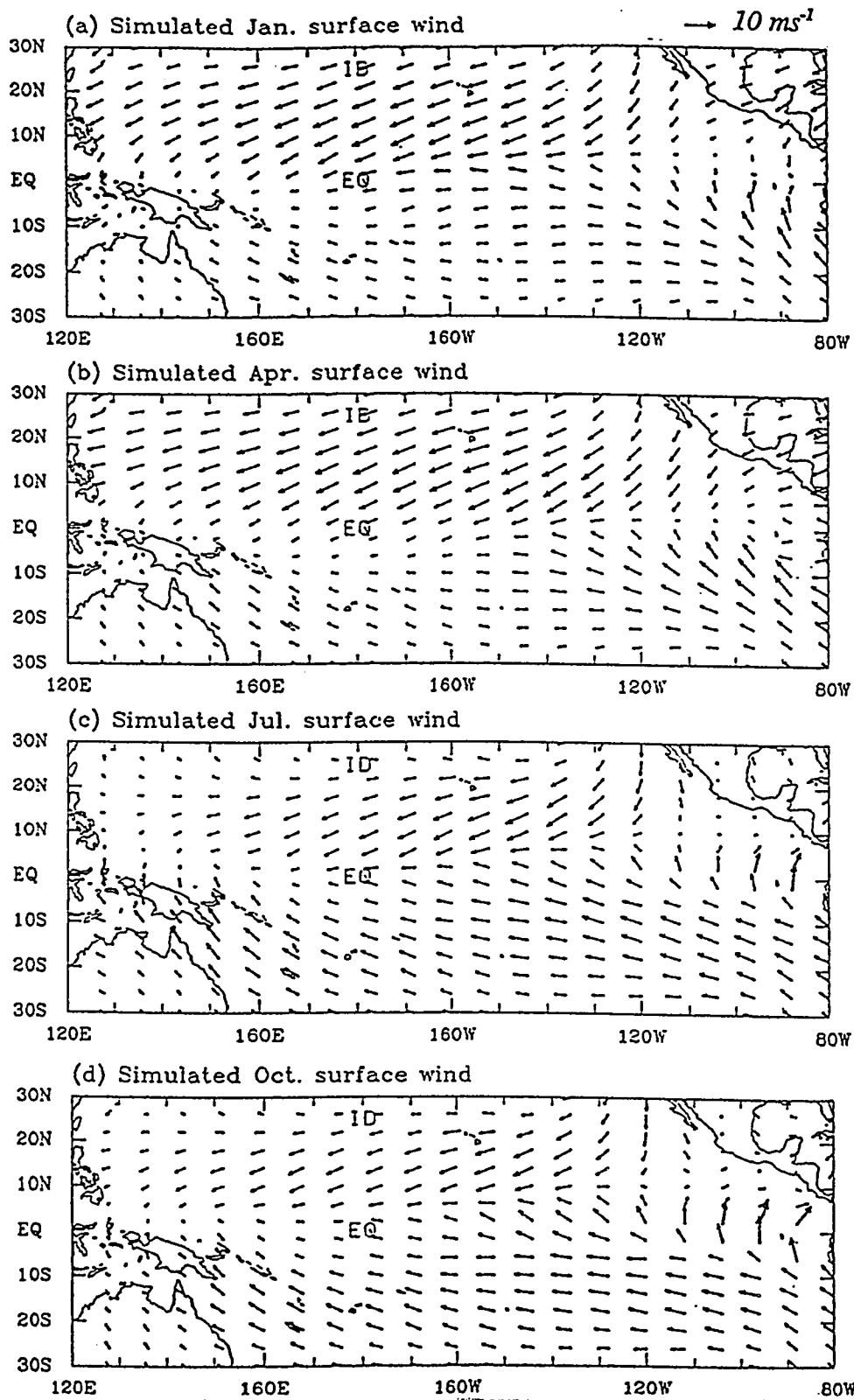


Fig. 14a The simulated (a) January, (b) April, (c) July, and (d) October surface wind (in units m/s) fields using the present model.

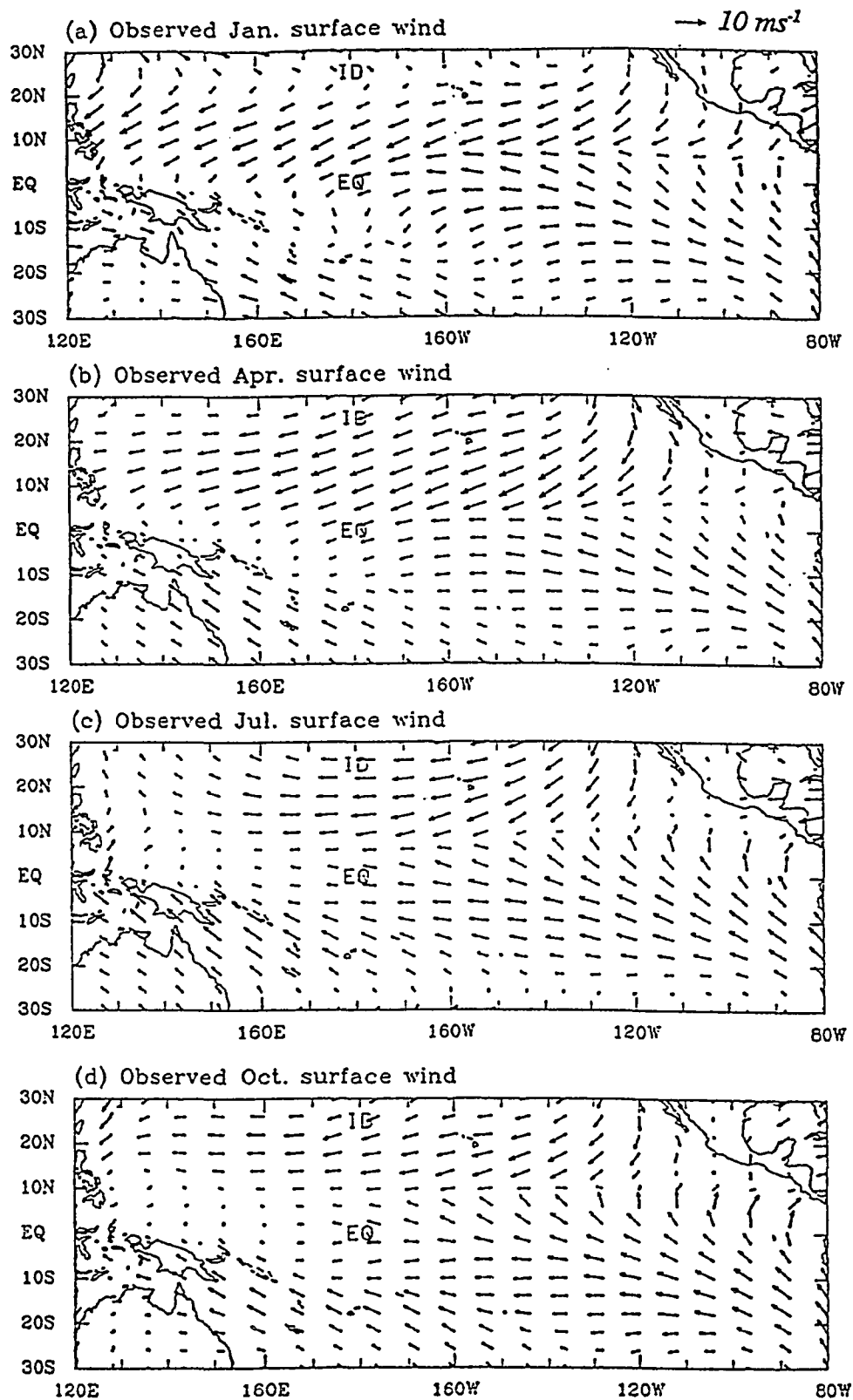


Fig. 14b The observed (a) January, (b) April, (c) July, and (d) October surface wind (in units m/s) fields (after Sadler et al. 1987).

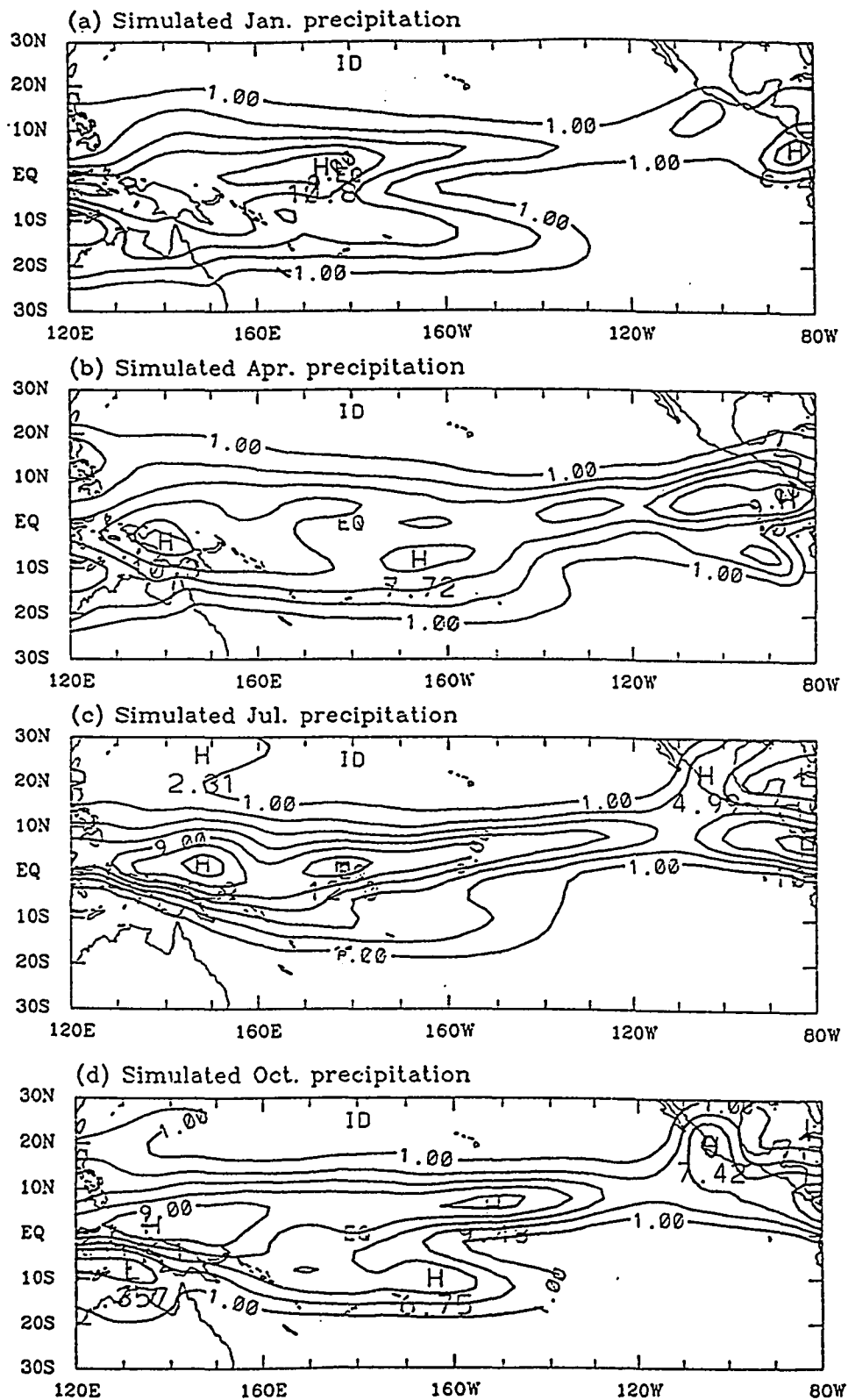


Fig. 15a The simulated precipitation rate (in units mm/day) fields for (a) January, (b) April, (c) July, and (d) October using the present model. Contour interval is 2 mm/day.

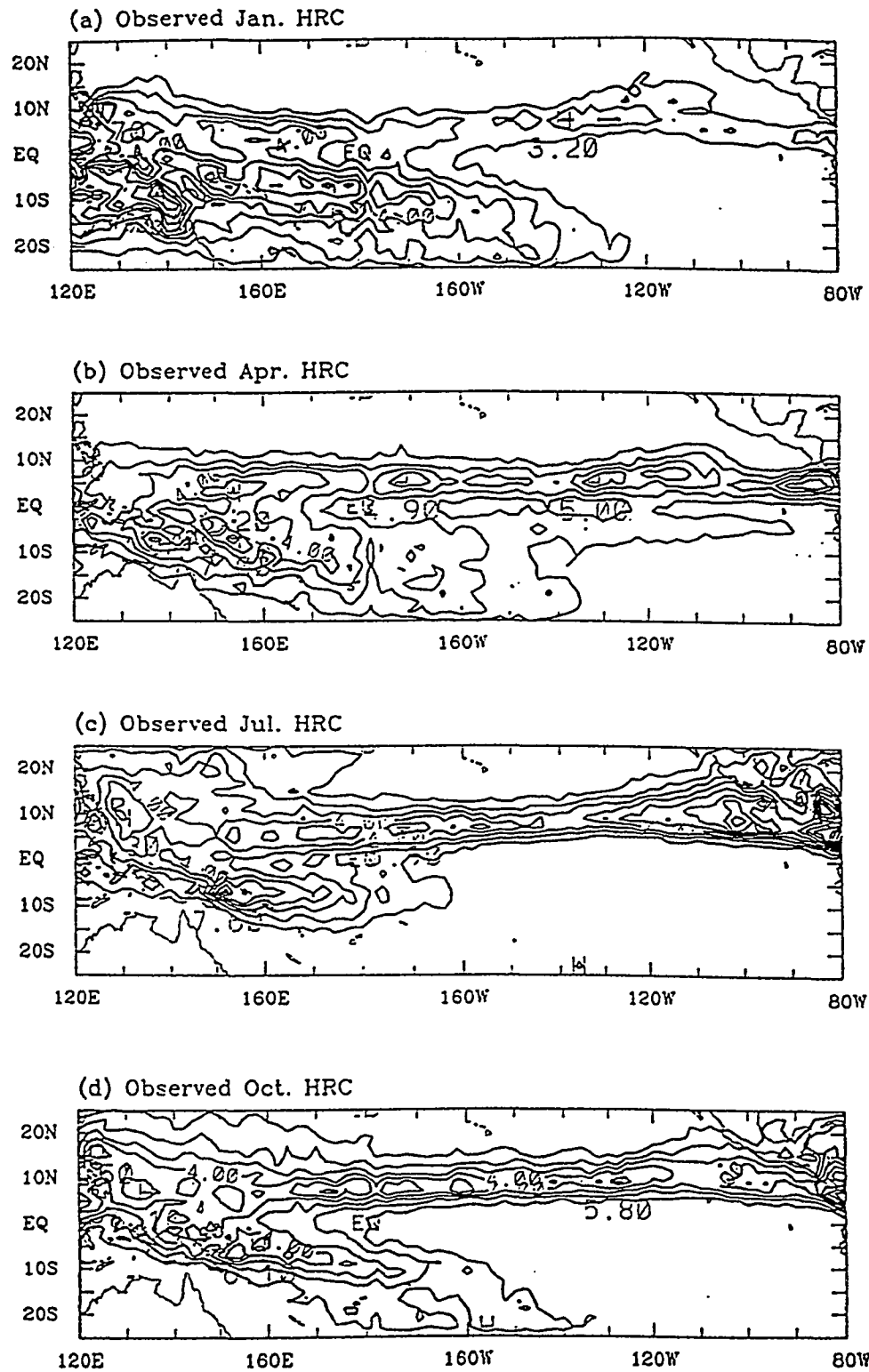


Fig. 15b The observed Highly Reflective Cloud (day/month) fields for (a) January, (b) April, (c) July, and (d) October (after Garcia 1985). Contour interval is 1 day/month.

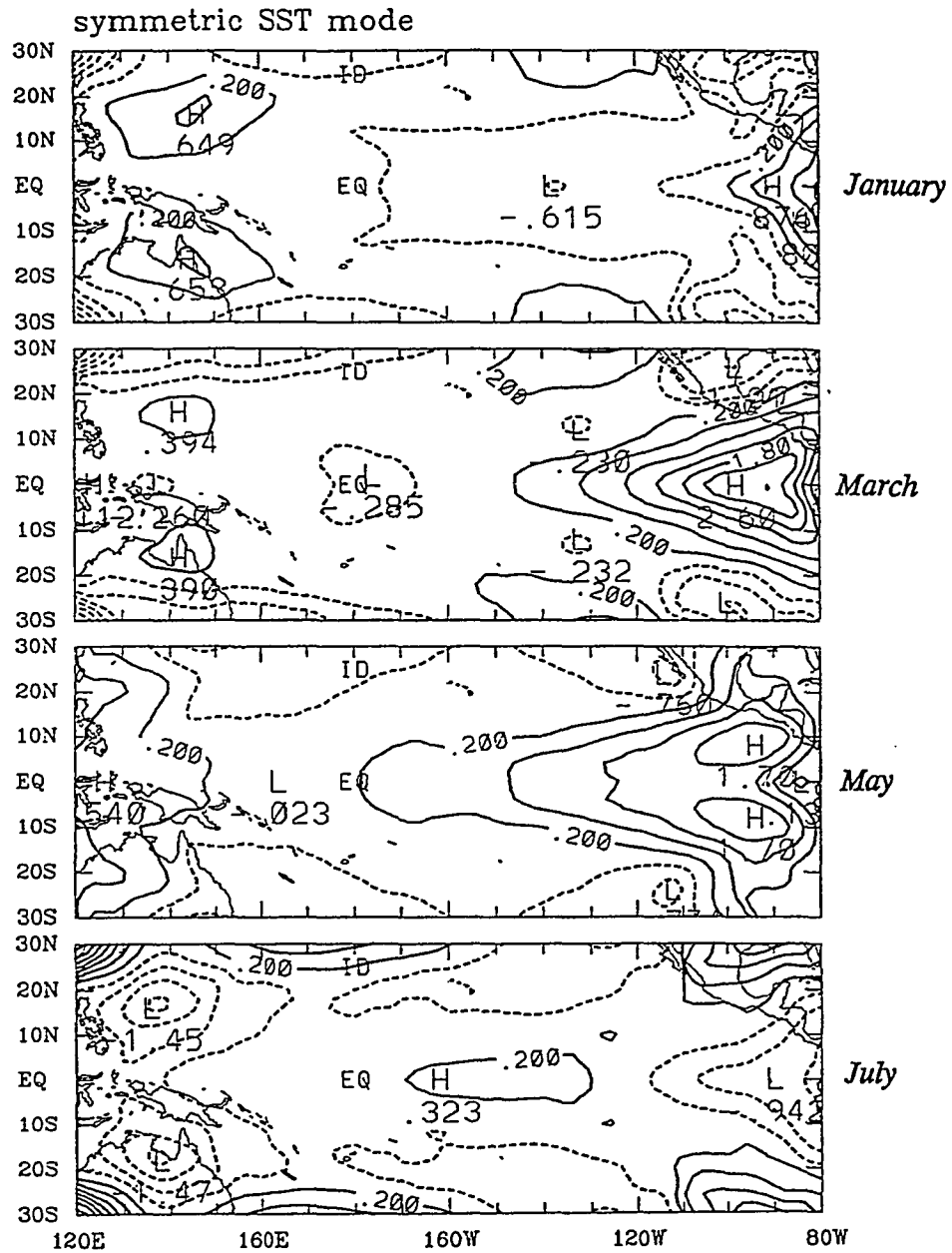


Fig. 16 The observed symmetric (to the equator) SST ( $^{\circ}$ C) modes in January, March, May, July, September, and November, respectively. Annual mean SST field has been removed. Contour interval is  $0.4^{\circ}$ C.

symmetric SST mode

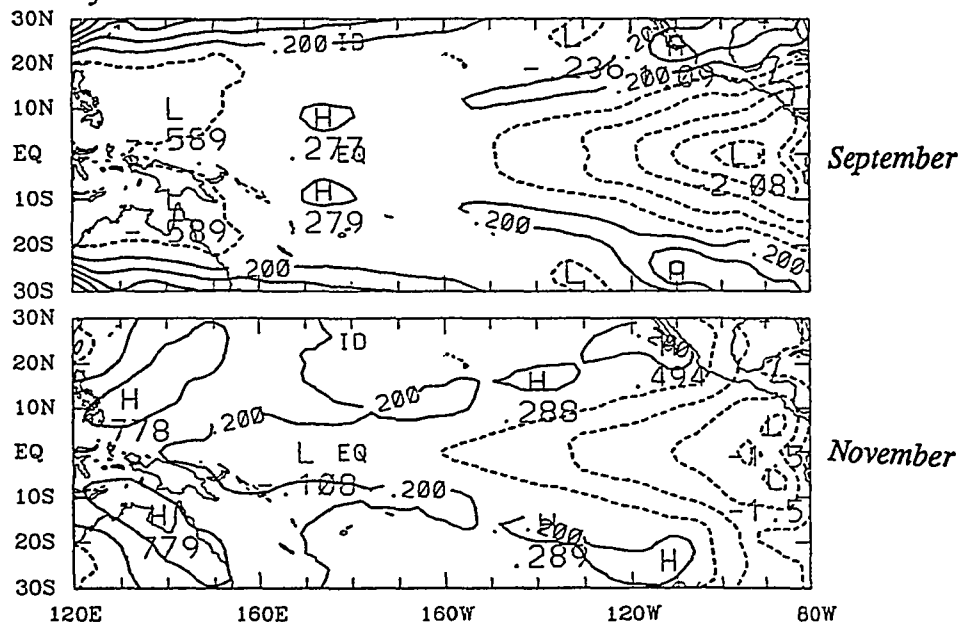


Fig. 16 (Continued)

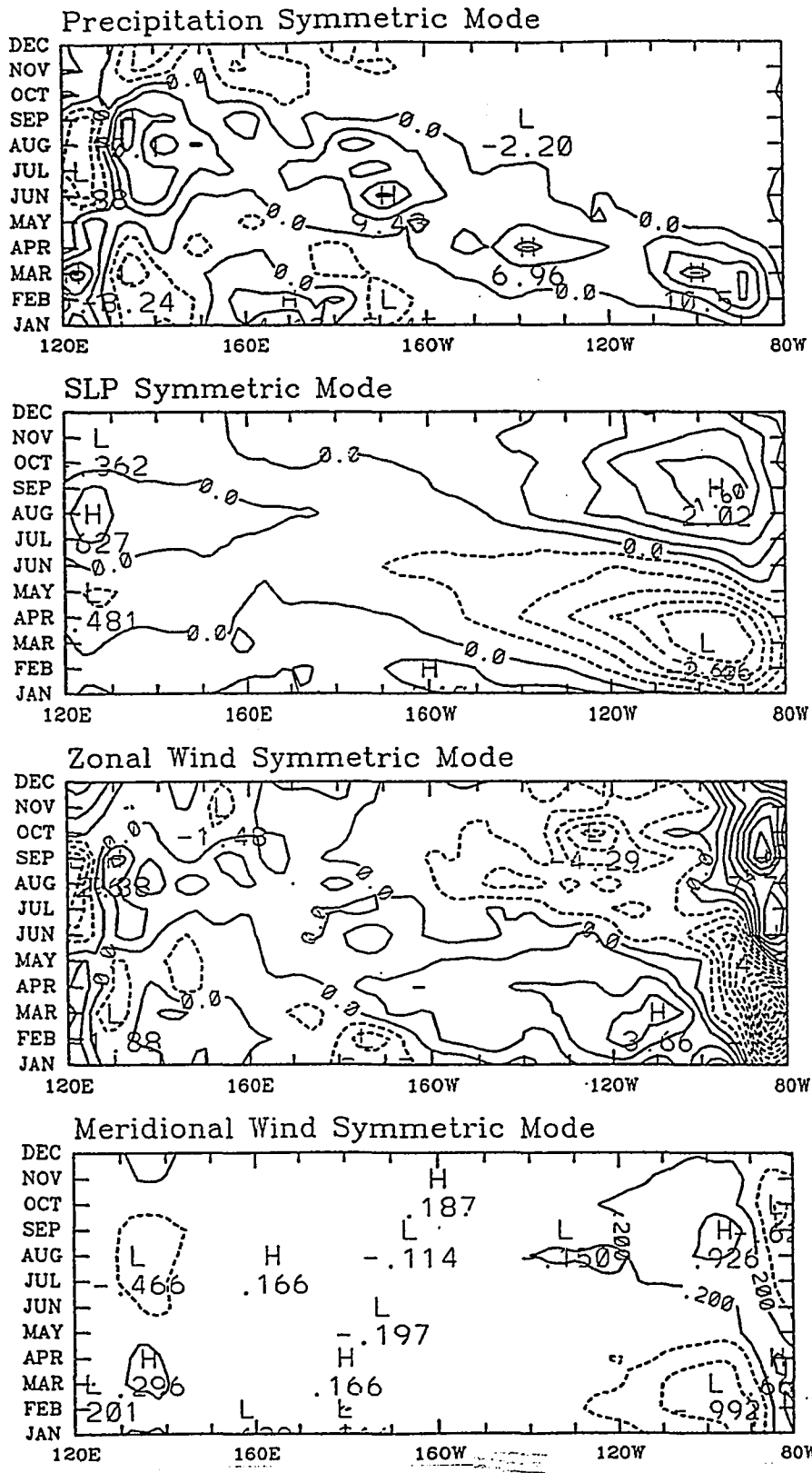


Fig. 17 The time-longitude section of precipitation rate (mm/day), sea-level pressure (mb) and zonal and meridional winds (m/s) along the equator in response to the symmetric SST forcing. Contour intervals are 3 mm/day, 0.4 mb, 1 m/s, and 0.4 m/s, respectively.

MONSOONAL MODE

ANNUAL MEAN

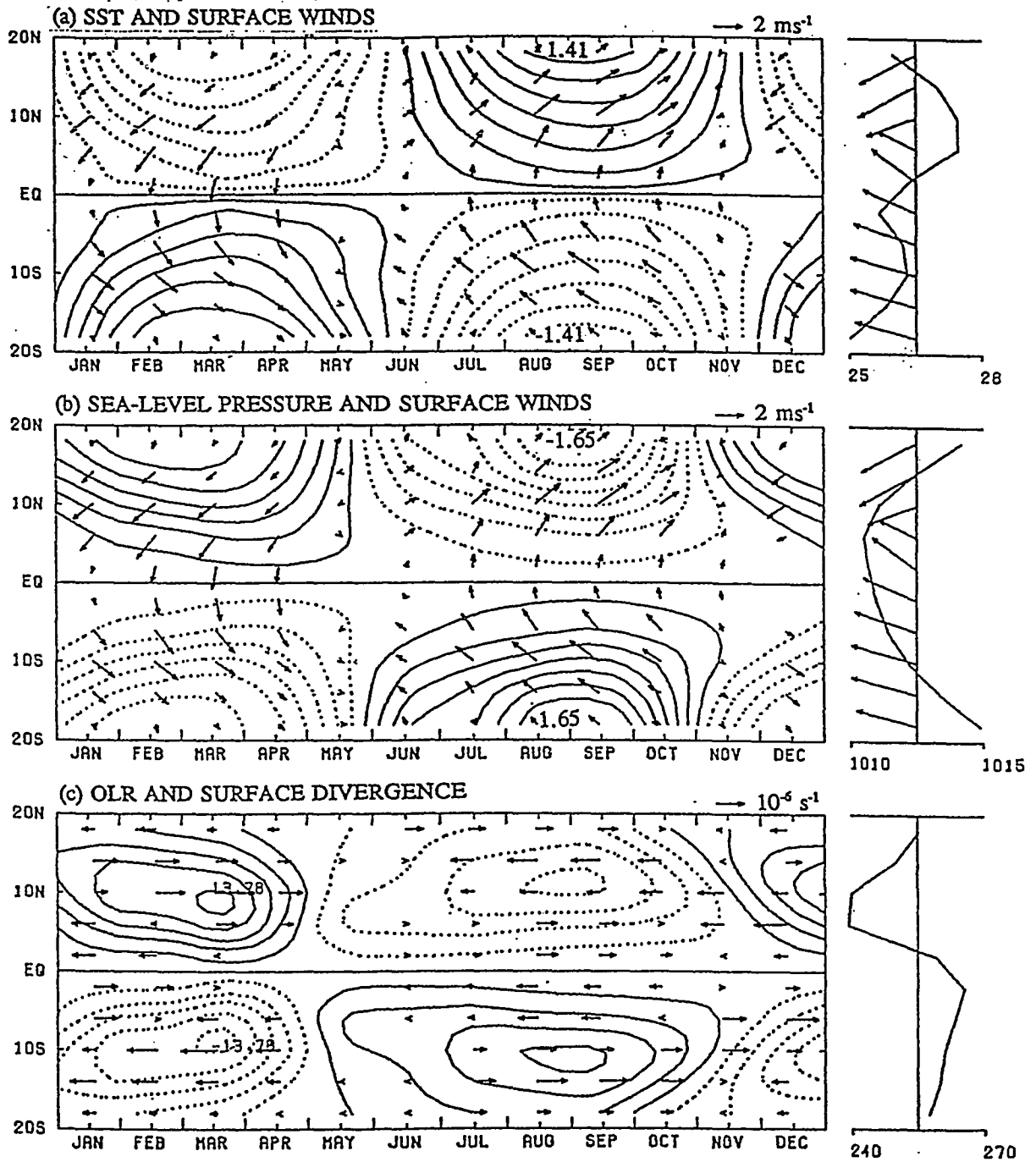


Fig. 18 The annual cycle of the zonal-averaged antisymmetric (to the equator) monsoonal mode of the monthly mean anomaly fields. The contour intervals for SST, SLP and OLR are 0.2°C, 0.2 mb, and 3 Wm<sup>-2</sup>, respectively (after Wang 1992b).

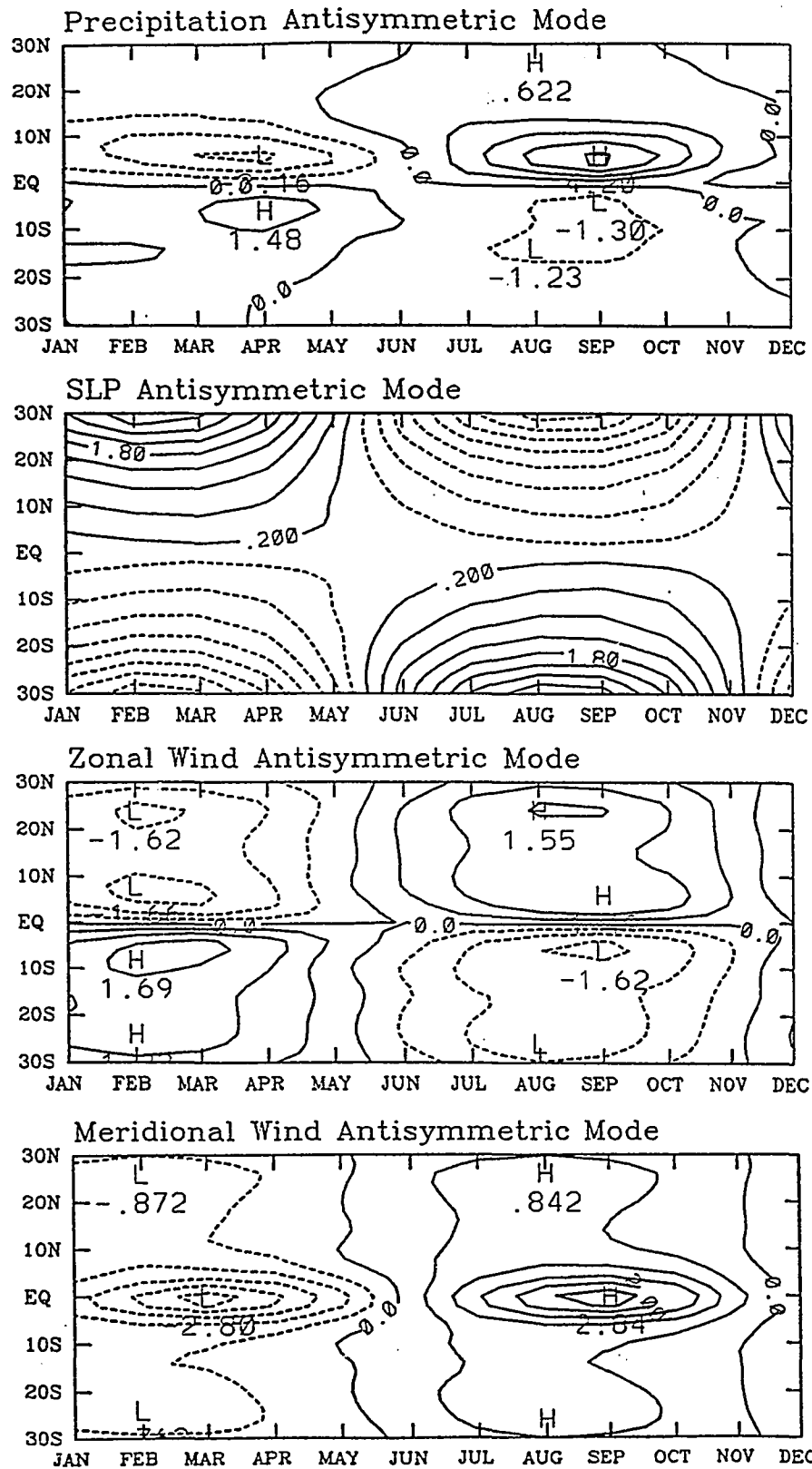


Fig. 19

The time-latitude section of zonal-mean precipitation rate (mm/day), sea-level pressure (mb) and zonal and meridional winds (m/s) in response to the antisymmetric SST forcing. Contour intervals are 1 mm/day, 0.4 mb, 0.5 m/s, and 0.5 m/s, respectively.

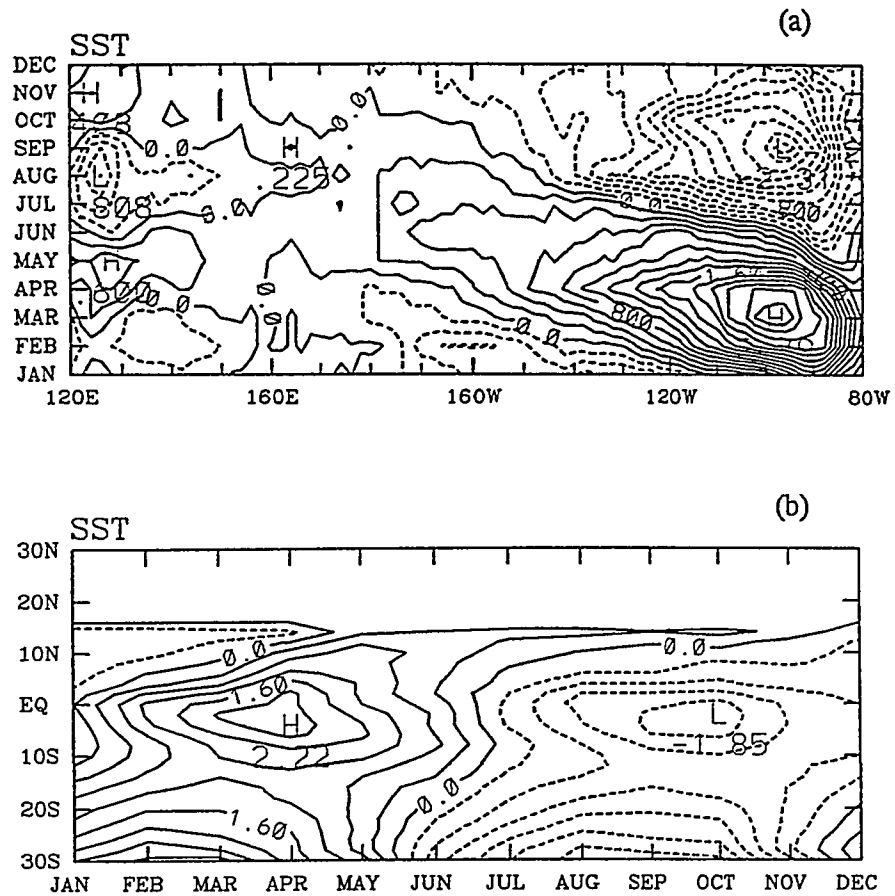


Fig. 20 (a) The time-longitude section of SST anomaly along the equator and (b) the time-latitude section of SST anomaly along 100-110°W. The SST is derived from COADS by Sadler et al. (1987). Contour intervals are 0.2°C and 0.4°C respectively.

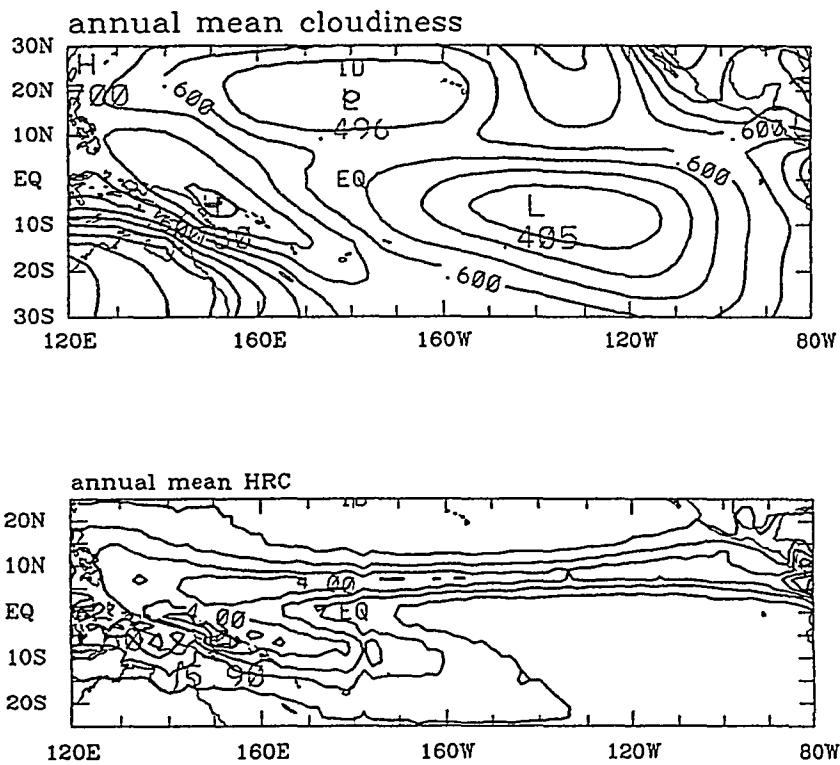


Fig. 21 Observed climatological annual mean cloudiness derived from Esbensen and Kushnir (1981) and annual mean HRC derived from Garcia (1985). Contour intervals are 0.05 and 1 day/month.



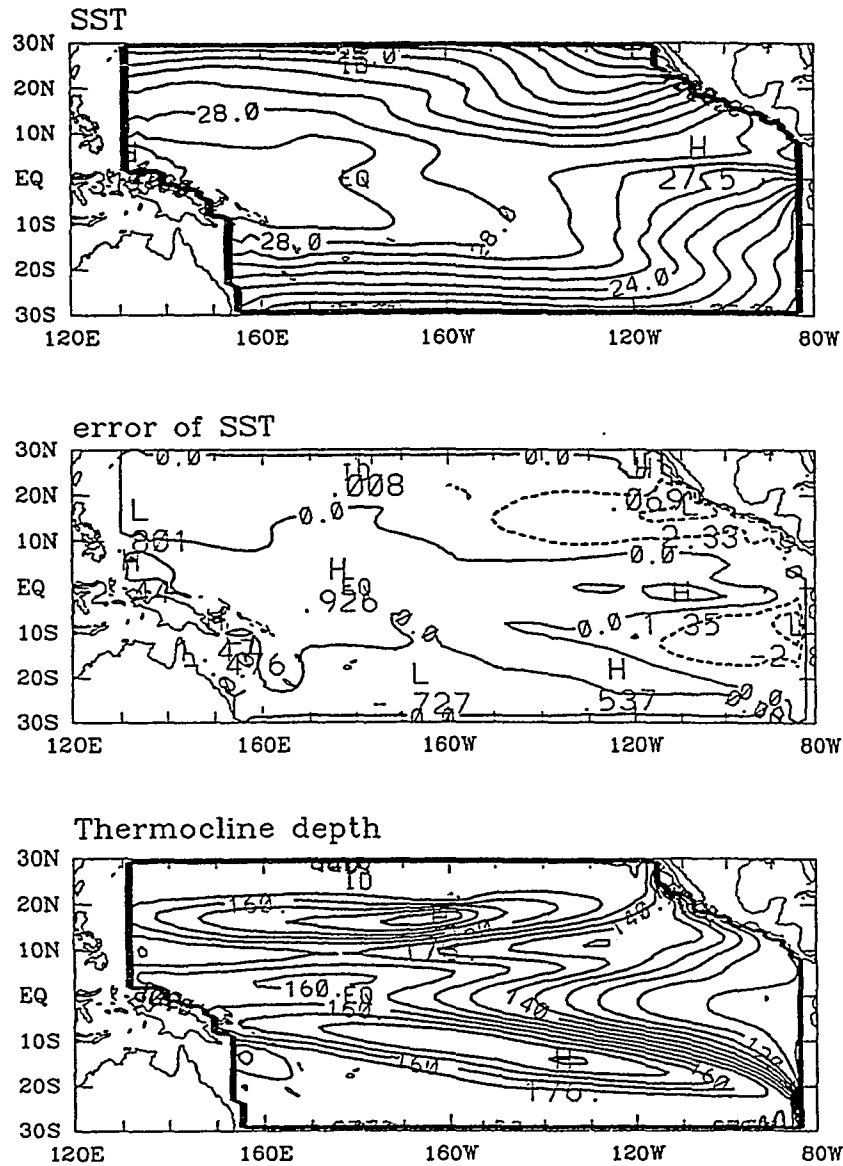


Fig. 23 The simulated annual mean SST ( $^{\circ}\text{C}$ ), the SST error, and thermocline depth (m) over the tropical Pacific in response to observed annual mean wind and thermal forcing. The surface winds are derived from COADS by Sadler et al. (1987) and the heat flux data are from Esbensen and Kushnir (1981). Contour intervals are  $1^{\circ}\text{C}$ ,  $1^{\circ}\text{C}$ , and 5 m, respectively.

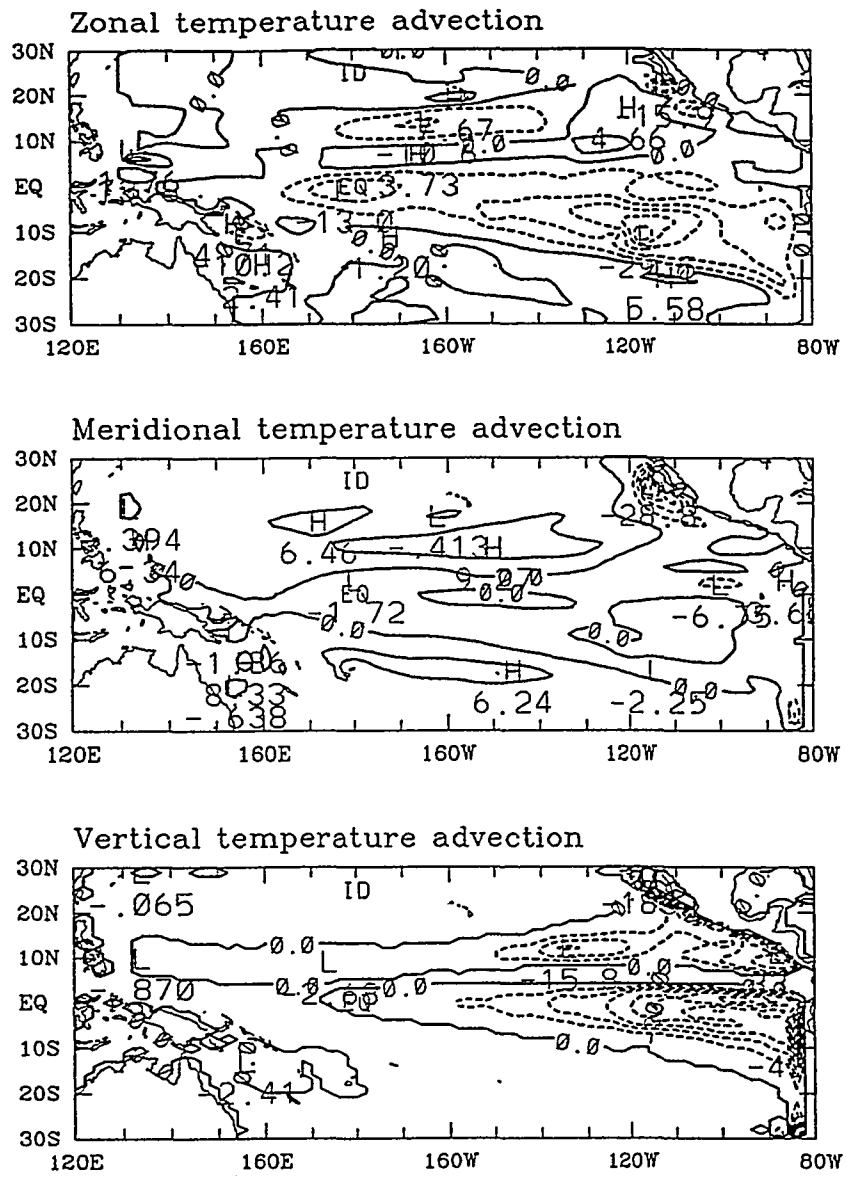


Fig. 24 The zonal temperature advection (a), meridional temperature advection (b), vertical temperature advection (c), and thermal forcing term (d) (in units of  $10^{-3} \text{ }^\circ\text{C/s}$ ) in the thermodynamic equation (3.2.5) for the first ocean experiment. Contour interval is  $5 \times 10^{-8} \text{ }^\circ\text{C/s}$ .

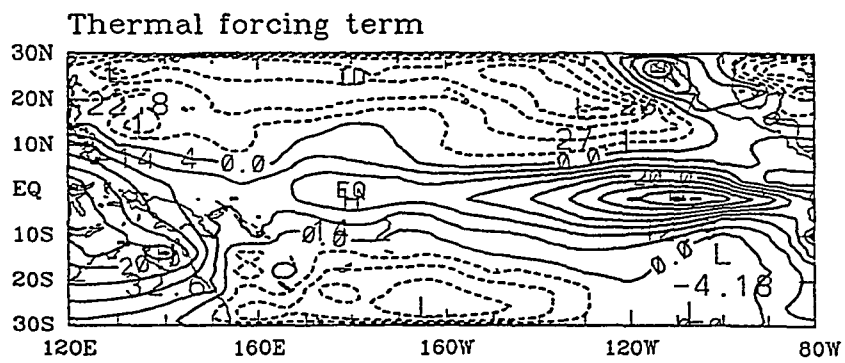


Fig. 24 (Continued)

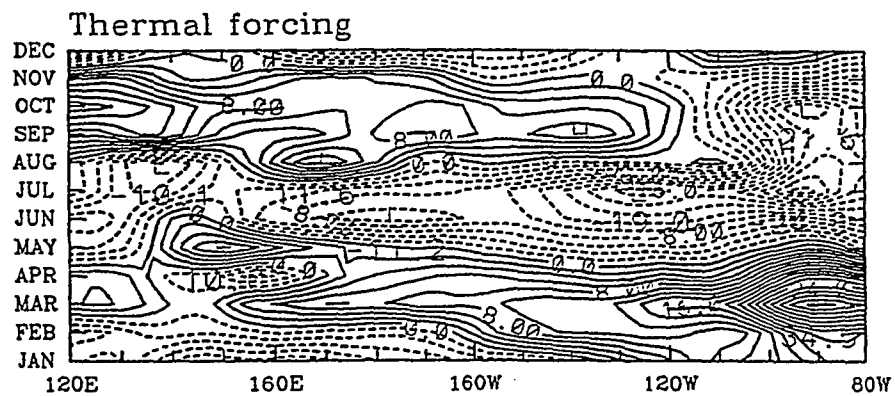
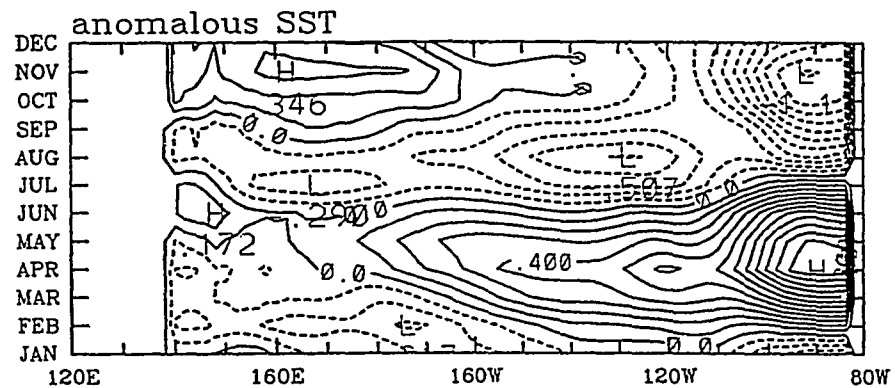


Fig. 25 The time-longitude section of the simulated SST anomaly and the observed thermal forcing anomaly along the equator for the second ocean experiment. Contour intervals are  $0.1^{\circ}\text{C}$  and  $2 \times 10^{-3} \text{ }^{\circ}\text{C/s}$  respectively.

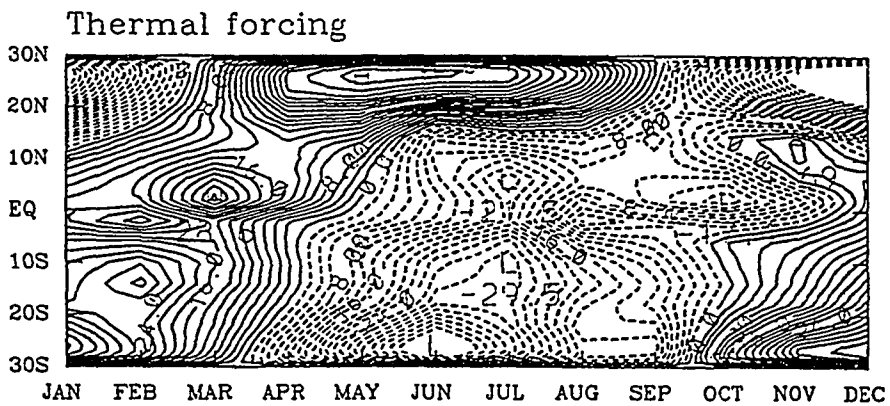
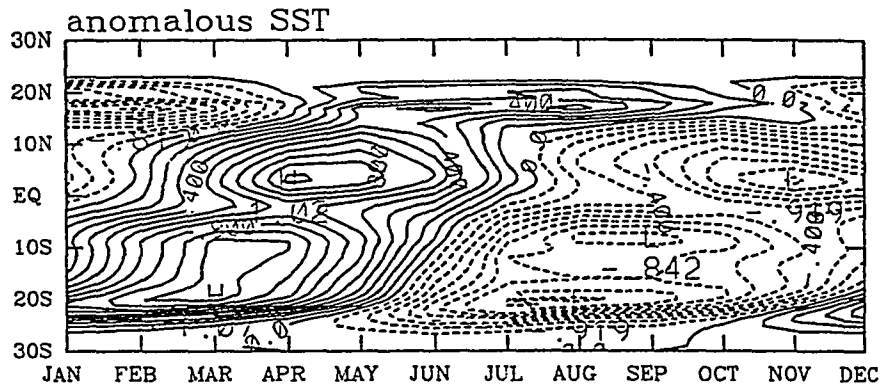


Fig. 26 The time-latitude section of the simulated SST anomaly and the observed thermal forcing anomaly along 100-110°W for the second ocean experiment. Contour intervals are 0.1°C and  $2 \times 10^{-3}$  °C/s respectively.

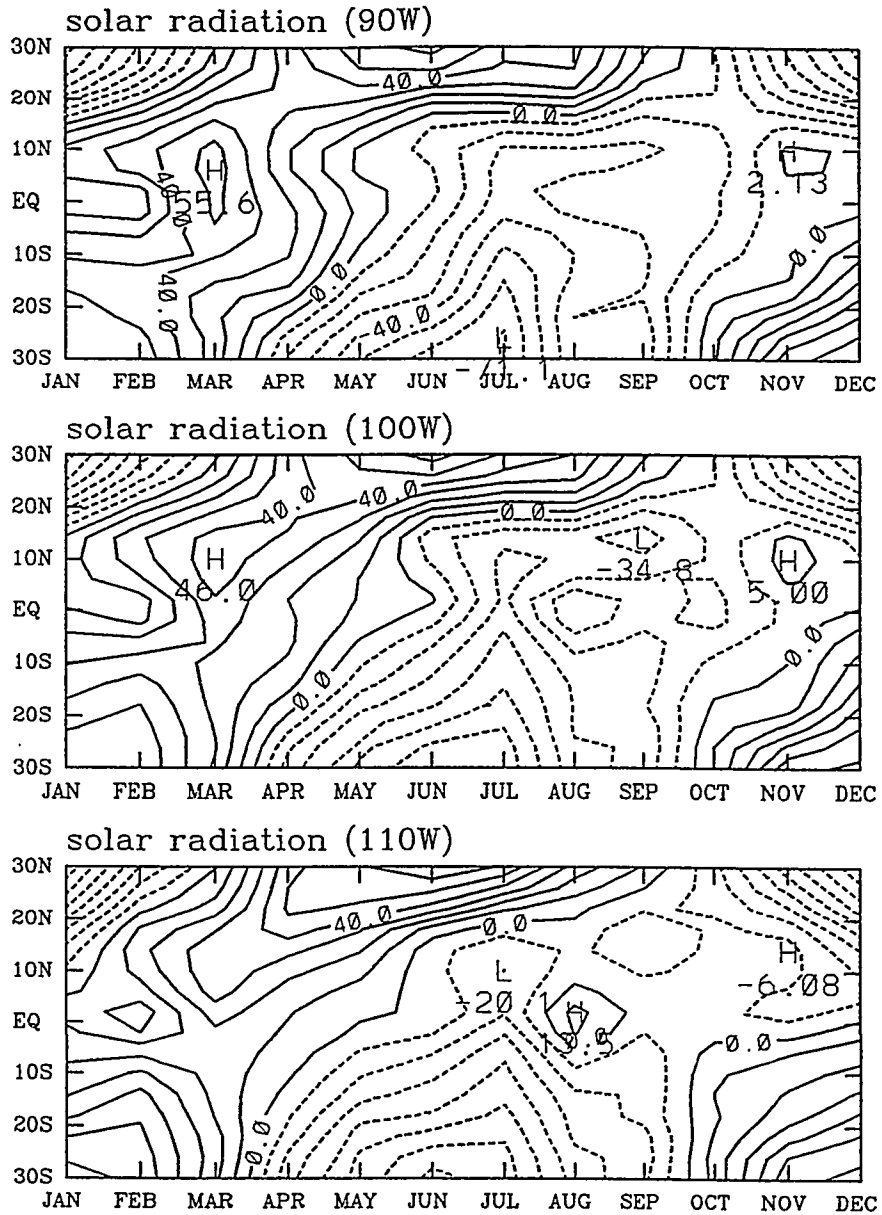


Fig. 27 The time-latitude section of downward solar flux at ocean surface derived from Esbensen and Kushnir (1981) along 90°W, 100°W, and 110°W, respectively. The effect of cloudiness has been considered. Contour interval is 10 Wm<sup>2</sup>.

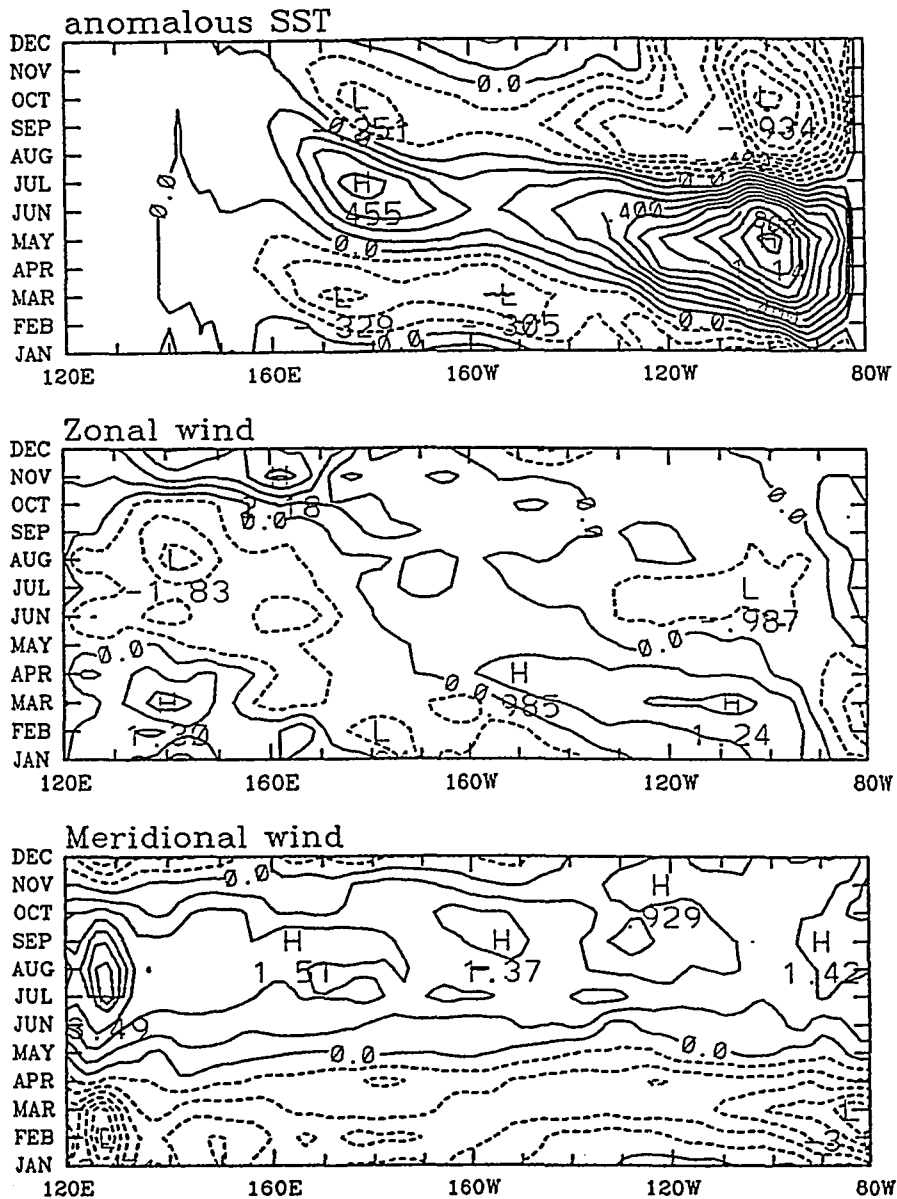


Fig. 28 The time-longitude section of the simulated SST anomaly and the observed surface zonal and meridional wind anomalies along the equator for the third ocean experiment. Contour intervals are 0.1°C, 0.5 m/s, and 0.5 m/s.

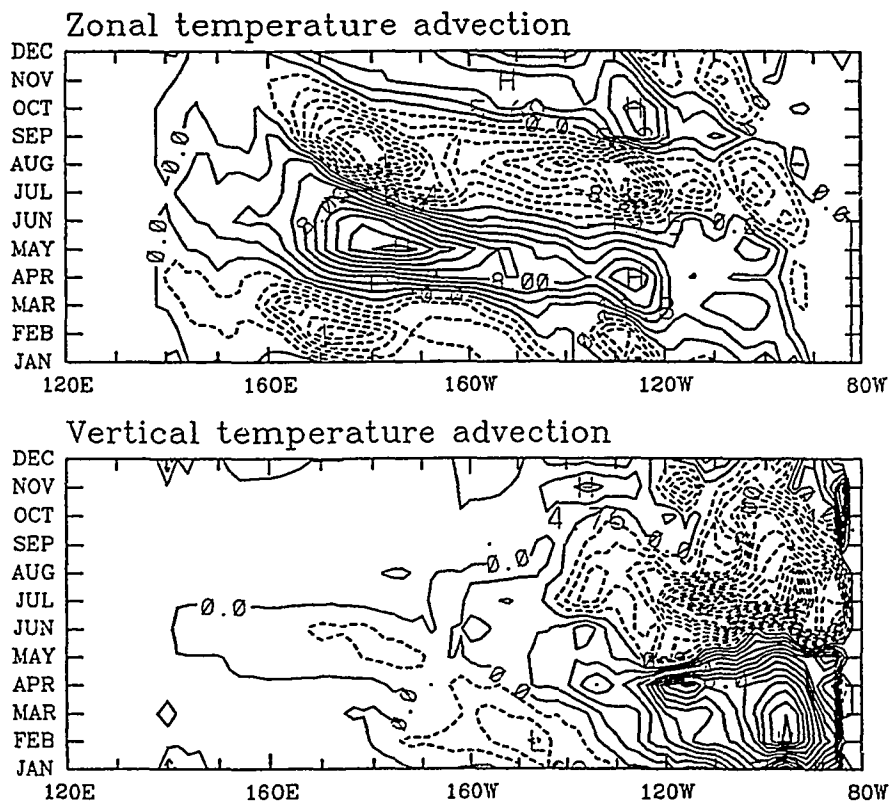


Fig. 29 The time-longitude section of the simulated zonal and vertical temperature advection anomalies along the equator in the third ocean experiment. Contour interval is  $2 \times 10^{-8} \text{ }^\circ\text{C/s}$ .

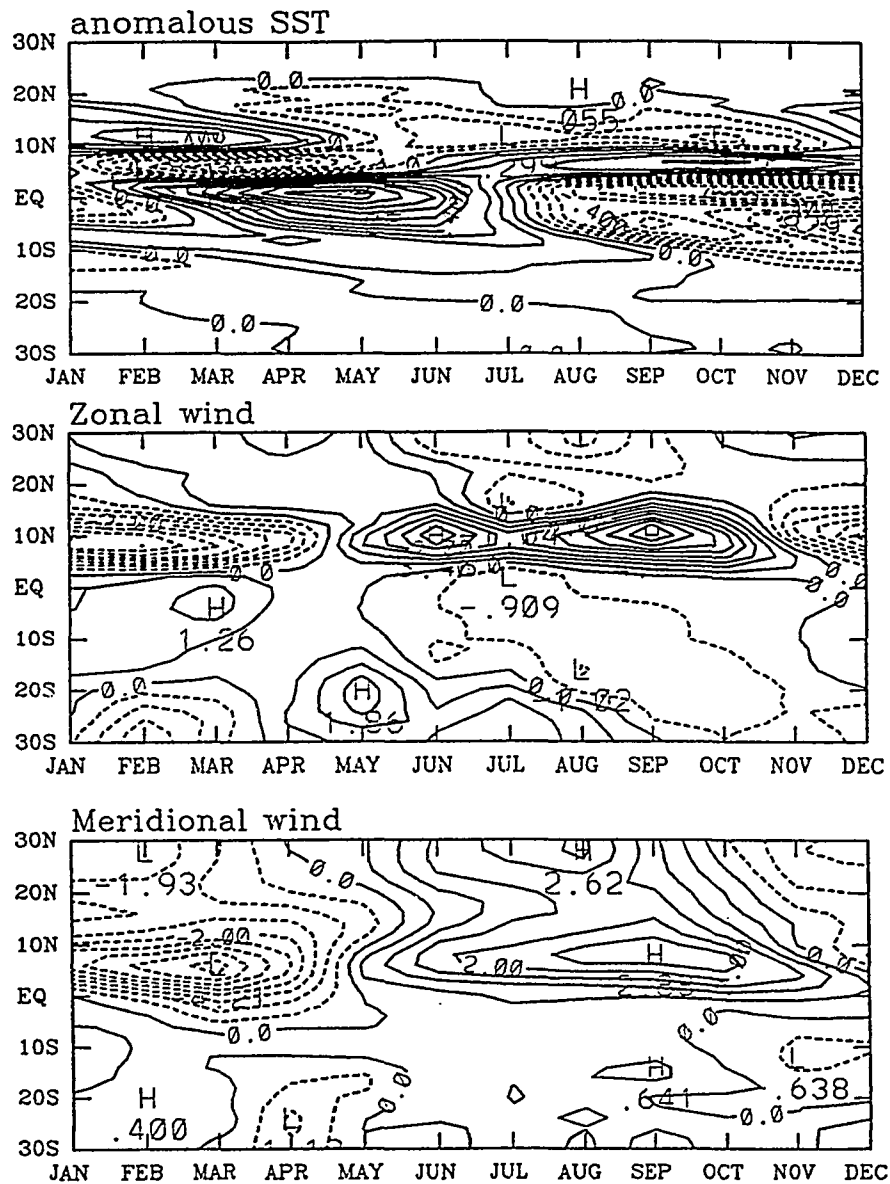


Fig. 30 The time-latitude section of the simulated SST anomaly and the observed surface zonal and meridional wind anomalies along 100-110°W in the third ocean experiment. Contour intervals are 0.1°C, 0.5 m/s, and 0.5 m/s, respectively.



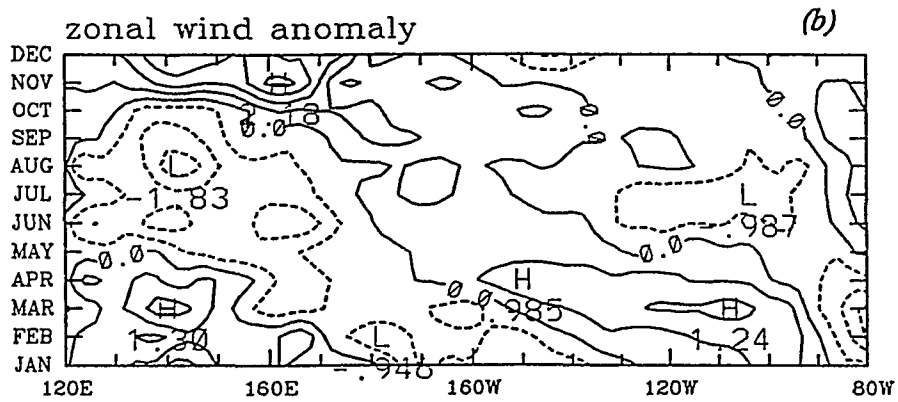
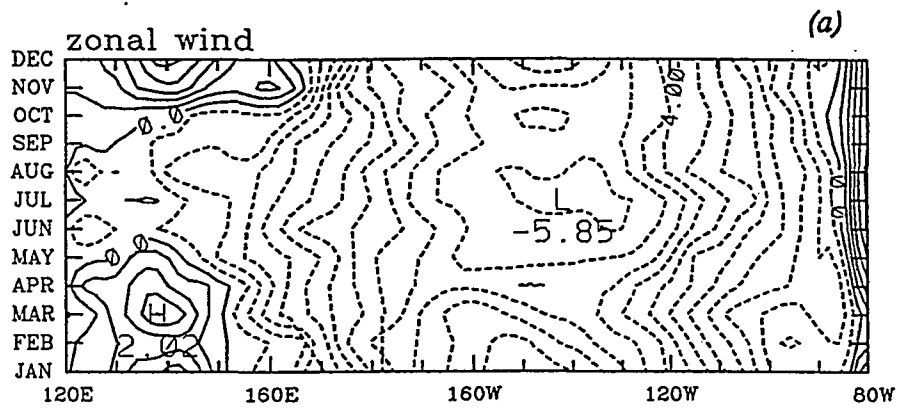


Fig. 32 Climatological monthly mean surface zonal wind (a) and the corresponding monthly mean anomaly (b) along the equator. Contour interval is 0.5 m/s.

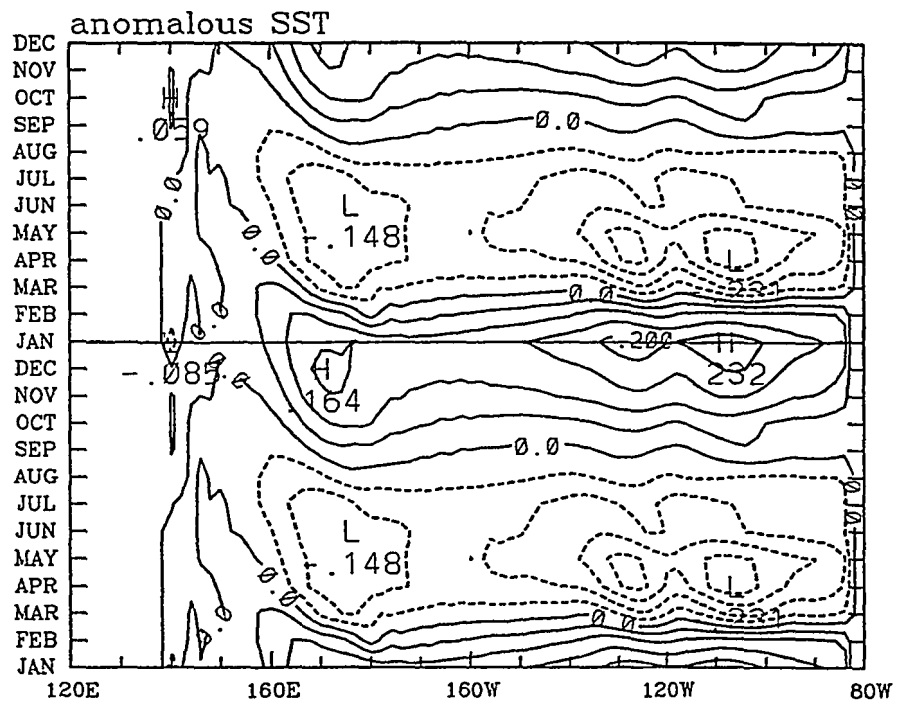


Fig. 33 Time-longitude section of simulated SST ( $^{\circ}\text{C}$ ) anomaly along the equator in response to anomalous surface wind forcing west of the date line. Contour interval is  $0.05^{\circ}\text{C}$ .

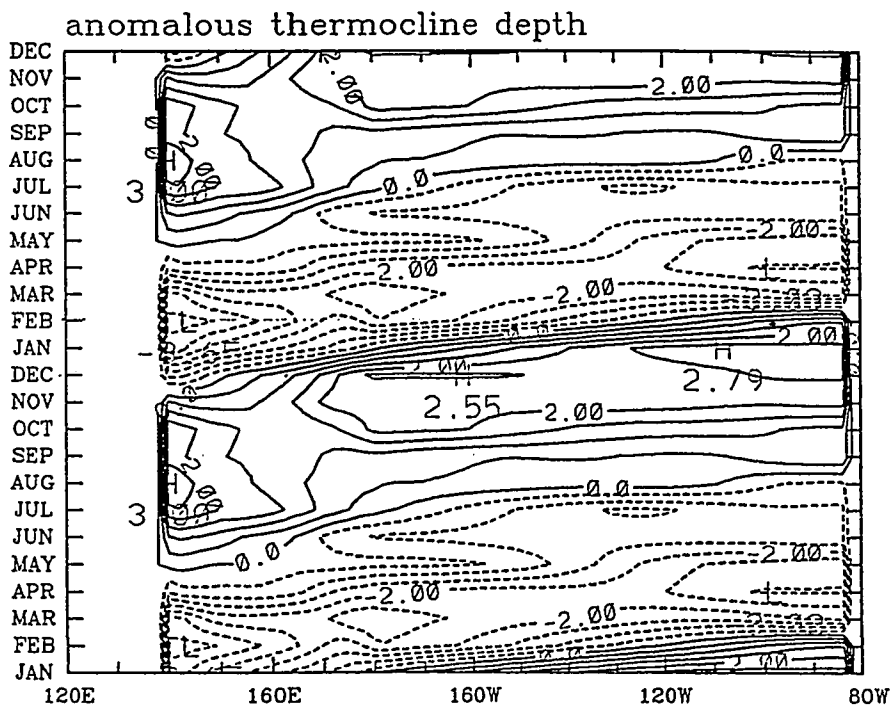


Fig. 34 As in Fig. 33 except for the simulated thermocline depth anomaly field (in units m). Contour interval is 0.5 m.



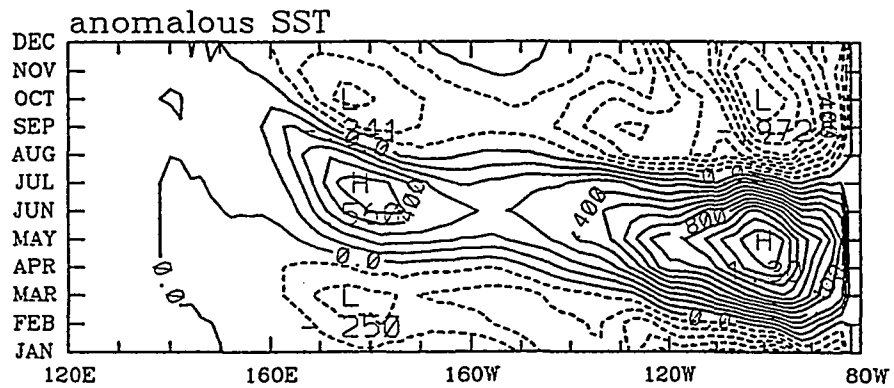


Fig. 36 Time-longitude section of the simulated SST anomaly ( $^{\circ}\text{C}$ ) along the equator in response to anomalous surface wind forcing east of the date line. Contour interval is  $0.1^{\circ}\text{C}$ .

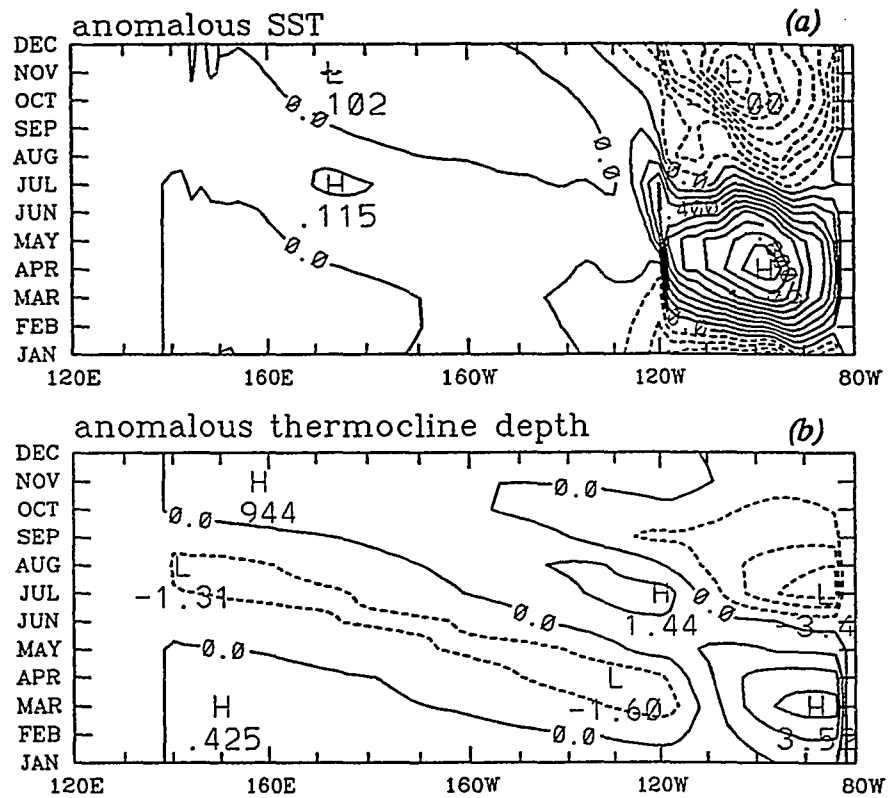


Fig. 37 Time-longitude section of the simulated SST ( $^{\circ}\text{C}$ ) and thermocline depth (m) anomalies along the equator in response to anomalous surface wind forcing east of  $120^{\circ}\text{W}$ . Contour intervals are  $0.1^{\circ}\text{C}$  and 1 m.

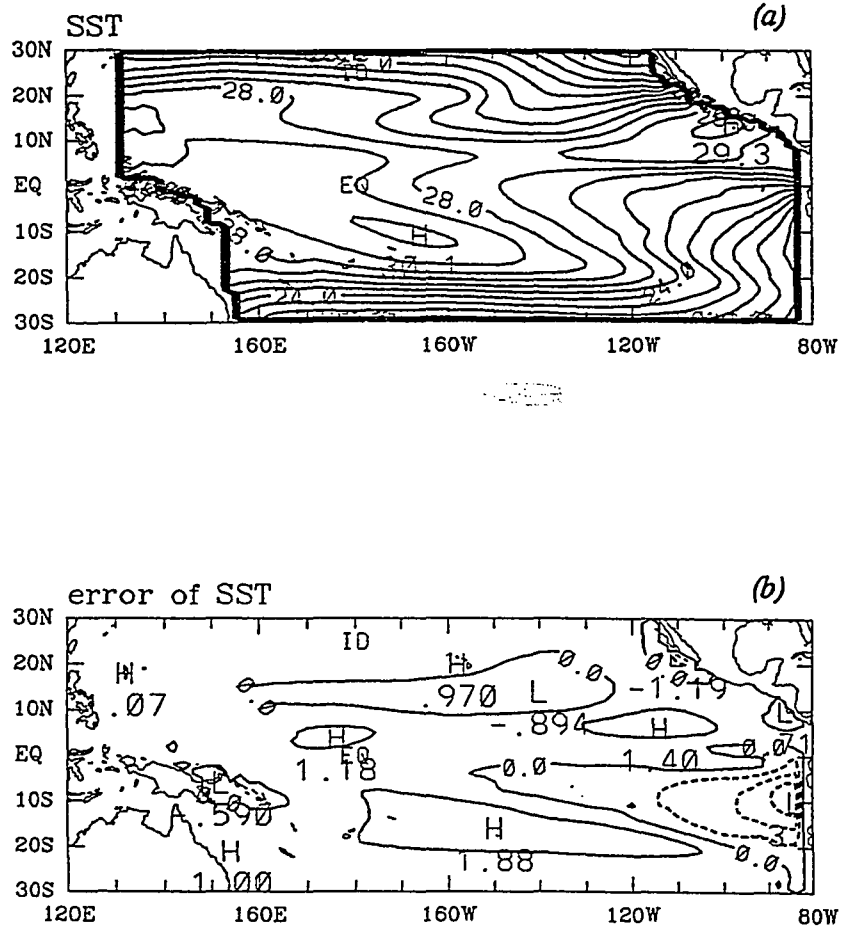


Fig. 38 Simulated annual mean SST field (a) and its error (b) for given climatological annual mean wind and cloudiness fields with the heat flux formulas of Equations (3.5.2)-(3.5.5). Contour interval is 1°C.

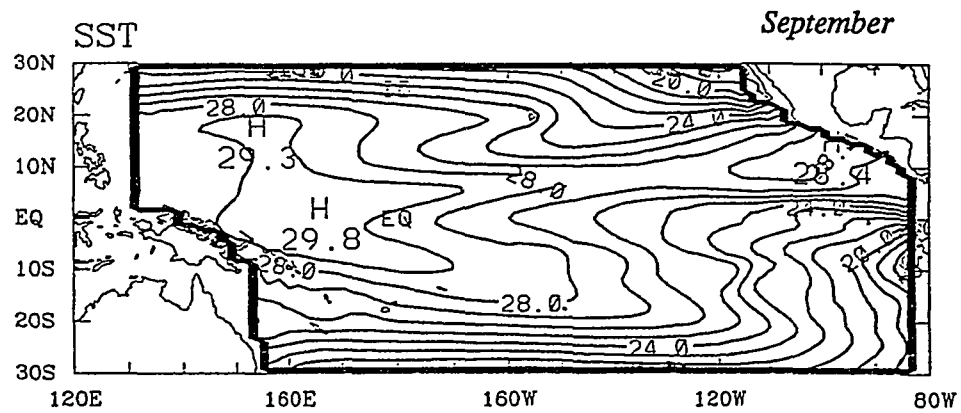
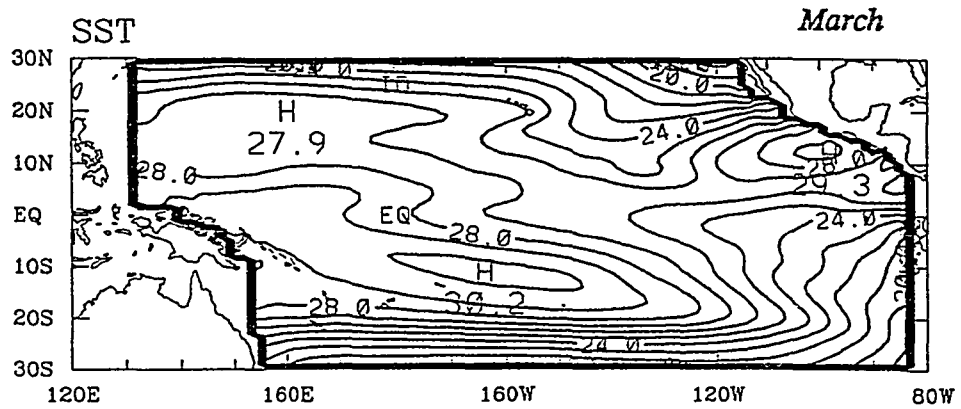


Fig. 39 Simulated March and September SST fields for given climatological monthly mean wind and cloudiness fields with the heat flux formulas of Equations (3.5.2)-(3.5.5). Contour interval is 1°C.

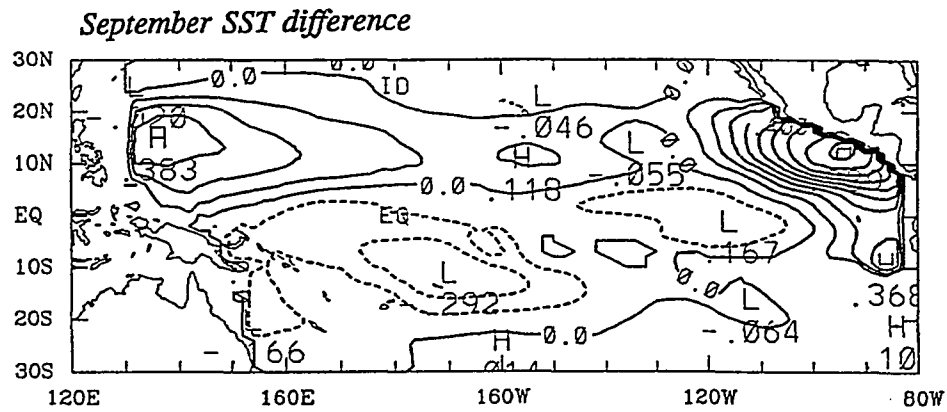
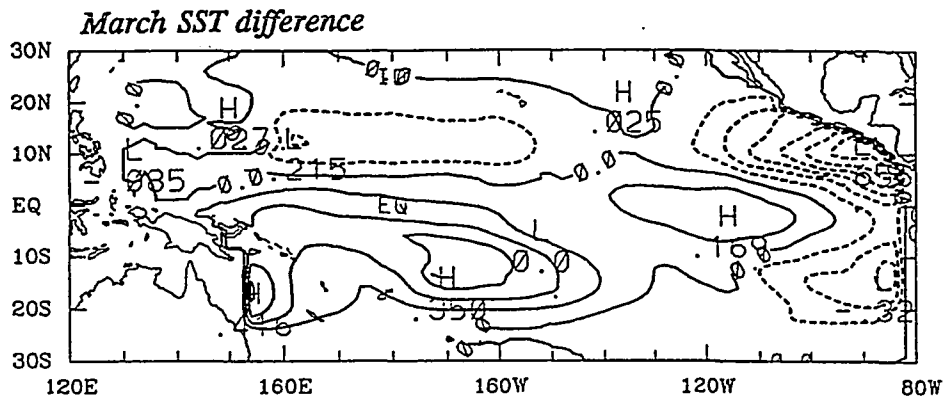


Fig. 40 The simulated SST difference in March and September between the experiments with fixed annual mean cloudiness and with varying monthly mean cloudiness. Contour interval is 0.1°C.

## REFERENCES

- Anderson, D.L.T., and J.P. McCreary, 1985: Slowly propagating disturbances in a coupled ocean-atmosphere model. J. Atmos. Sci., 42, 615-629.
- Betts, A.K., 1982: Saturation point analysis of moist convective overturning. J. Atmos. Sci., 39, 1484-1505.
- Bjerknes, J., 1966: A possible response of the atmospheric Hadley circulation to equatorial anomalies of ocean temperature. Tellus, 18, 820-829.
- Budyko, M. I., 1974: Climate and life. Academic. Pres., 508 pp.
- Cane, M.A., 1979: The response of an equatorial ocean to simple wind stress patterns. I. Model formulation and analytical results. J. Mar. Res., 37, 233-252.
- Chang, P., 1993: A study of seasonal cycle of sea surface temperature in the tropical Pacific Ocean using reduced gravity models. Submitted to J. Geophys. Res..
- Davey, M.K., and A.E. Gill, 1987: Experiments on tropical circulation with a simple moist model. Quart. J. Roy. Meteor. Soc., 113, 1237-1269.
- Deser, C., 1993: Diagnosis of the surface momentum balance over the tropical Pacific Ocean. J. Climate, 6, 64-74.
- Emmanuel, K.A., 1986: An air-sea interaction theory for tropical cyclones. Part I. J. Atmos. Sci., 43, 585-604.

- Esbensen, S.K., and V. Kushnir, 1981: The heat budget of the global ocean: an atlas based on estimates from marine surface observations. Rep. 29, Clim. Res. Inst., Oreg. State Univ., Corvallis.
- Garcia, O., 1985: Atlas of Highly Reflective clouds for the global tropics: 1971-1973. U.S. Department of Commerce, NOAA, Environmental Research Lab., Boulder, Co.
- Gent, P.R., 1991: The heat budget of the TOGA-COARE domain in an ocean model. J. Geophys. Res., 96, 3323-3330.
- Gill, A.E., 1980: Some simple solutions for heat-induced tropical circulation. Quart. J. Roy. Meteor. Soc., 106, 447-462.
- \_\_\_\_\_, 1982: Studies of moist effects in simple atmospheric models: the stable case. J. Geophys. Astrophys. Fluid Dynamics, 19, 119-152.
- Gordon, C. and R.A. Corry, 1991: A model simulation of the seasonal cycle in the tropical Pacific ocean using climatological and modeled surface forcing. J. Geophys. Res., Vol. 96, No. C1, 847-864.
- Horel, J.D., 1982: On the annual cycle of the tropical Pacific atmosphere and ocean. Mon. Wea. Rev., 110, 1863-1878.
- Knox, R., and D. Halpern, 1982: Long range Kelvin wave propagation of transport variations in Pacific Ocean equatorial currents. J. Mar. Res., 40, 329-339.

- Kuo, H.-L., 1974: Further studies of the parameterization of the influence of cumulus convection on large-scale flow. J. Atmos. Sci., 31, 1231-1240.
- Lander, M.A., 1986: Theory and observation of the relationship among the wind and relevant forces in the tropical marine atmospheric boundary layer. Ph.D. dissertation, Department of Meteorology, University of Hawaii.
- Li, T., and B. Wang, 1992: A conceptual climate model for simulating the surface winds and precipitation over the tropical Pacific. Submitted to J. Atmos. Sci..
- Liao, D., and L. Wang, 1986: Theory and application of numerical weather prediction. 527 pp (in Chinese).
- Lindzen, R.S., and S. Nigam, 1987: On the role of sea surface temperature gradients in forcing low-level winds and convergence in the tropics. J. Atmos. Sci., 45, 2440-2458.
- Lukas, R., 1981: The termination of the equatorial undercurrent in the eastern Pacific. Ph.D. dissertation, Department of Oceanography, University of Hawaii, 127pp.
- \_\_\_\_\_, S. P. Hayes, and K. Wyrтки, 1984: Equatorial sea level response during the 1982-83 El Nino. J. Geophys. Res., 89, 10425-10430.
- \_\_\_\_\_, and E. Firing, 1985: The annual Rossby wave in the central equatorial Pacific ocean. J. Phys. Oceanogr., 15, 55-67.

- Matsuno, T., 1966: Quasi-geostrophic motions in the equatorial area. J. Meteor. Jap., Ser. II, 44, 25-43.
- Mitchell T. P., and J. M. Wallace, 1992: On the annual cycle in equatorial convection and sea-surface temperature. J. Climate, 5, 1140-1156.
- Murakami, T., B. Wang, and S.W. Lyons, 1992: Summer monsoons over the Bay of Bengal and the eastern North Pacific. J. Meteorol. Soc. Japan, 70, 191-210.
- Murphree, T., and H. van den Douk, 1988: Calculating winds from time mean sea level pressure fields. J. Atmos. Sci., 45, 3269-3281.
- Neelin, J.D., 1989: On the interpretation of the Gill model. J. Atmos. Sci., 46, 2466-2468.
- Payne, R. E., 1972: Albedo of the sea surface. J. Atmos. Sci., 29, 959-970.
- Philander, S. G. H., 1990: El Nino, La Nina, Southern Oscillation.
- \_\_\_\_\_, W. J. Hurlin, and A. D. Seigel, 1987: Simulation of the seasonal cycle of the tropical Pacific Ocean. J. Phys. Oceanogr., 17, 1986-2002.
- \_\_\_\_\_, T. Yamagata and R.C. Pacanowski, 1984: Unstable air-sea interaction in the tropics. J. Atmos. Sci., 41, 603-613.
- Sadler, J.C., M.A. Lander, A.M. Hori, and L.K. Oda, 1987: Tropical marine climatic atlas. Vol. 2, Pacific Ocean.

- Report UHMET 87-02, Department of Meteorology, University of Hawaii, Honolulu, Hawaii, p27.
- Seager, R., S. E. Zebiak, and M. A. Cane, 1988: A model of the tropical Pacific sea surface temperature climatology. J. Geophys. Res., 93, 1265-1280.
- Schopf, P.S., and M.J. Suarez, 1988: Vacillations in a coupled ocean-atmosphere model. J.Atmos.Sci., 45, 549-566.
- Seager, R., 1991: A simple model of the climatology and variability of the low-level wind field in the tropics. J. Climate, 4, 164-179.
- Taylor, R.C., 1973: An atlas of Pacific island rainfall. Hawaii Inst. Geophys. Data Rep., HIG-73-9, 175 pp. (NTIS No. AD 767073).
- Wang, B., 1988: Dynamics of tropical low frequency waves: an analysis of the moist Kelvin waves. J.Atmos.Sci., 45, 2051-2065.
- \_\_\_\_\_, 1992a: Climatic regimes of tropical convection and rainfall. Submitted to J. Climate.
- \_\_\_\_\_, 1992b: On the annual cycle in the equatorial Pacific cold tongue. Submitted to J. Atmos. Sci.
- \_\_\_\_\_, and T. Li, 1993: A simple tropical atmospheric model of relevance to short-term climate variations. J. Atmos. Sci., 50, 260-284.
- Weare, B.C., P. T. Strub, and M. D. Samuel, 1981: Marine climate atlas of the tropical Pacific Ocean, 147 pp, Dep. of Land, Air, and Water Resour., Univ. of Calif., Davis.

- Webster, P. J., and R. Lukas, 1992: TOGA COARE: The coupled ocean-atmosphere Response Experiment. Bull. Amer. Meteor. Soc., 73, 1377-1416.
- Wyrтки, K., 1965: The average annual heat balance of the North Pacific Ocean and its relation to ocean circulation. J. Geophys. Res., 70, 4547-4559.
- Zebiak, S.E., 1982: A simple atmosphere model of relevance to El Nino. J. Atmos. Sci., 39, 2017-2027.
- \_\_\_\_\_, 1986: Atmospheric convergence feedback in a simple model for El Nino. Mon. Wea. Rev., 114, 1263-1271.
- \_\_\_\_\_, 1990: Diagnostic studies of Pacific surface winds. J. Climate, 3, 1016-1031.
- \_\_\_\_\_, and M.A. Cane, 1987: A model El Nino-Southern Oscillation. Mon. Wea. Rev., 115, 2262-2278.